APPLIED COMPUTATIONAL ELECTROMAGNETICS SOCIETY JOURNAL

August 2022
Vol. 37 No. 8
ISSN 1054-4887

The ACES Journal is abstracted in INSPEC, in Engineering Index, DTIC, Science Citation Index Expanded, the Research Alert, and to Current Contents/Engineering, Computing & Technology.

The illustrations on the front cover have been obtained from the ARC research group at the Department of Electrical Engineering, Colorado School of Mines

Published, sold and distributed by: River Publishers, Alsbjergvej 10, 9260 Gistrup, Denmark

AUGUST 2022 REVIEWERS

Layla H. Abood
Djelloul Aissaoui
Rezaul Azim
Behrokh Beiranvand
Syed Sabir Hussain Bukhari
Mahendran C.
Xiaoming Chen
Merit Cisneros-Gonzalez
Yogesh Kumar Coukiker
Arkaprovo Das
Tanmaya Kymar Das
Zaheer Ahmed Dayo
Mona Elhelbawy
Piotr Gas
Bernhard J. Hoenders
Muyu Hou
I. Kathir
Ashutosh Kedar
Wang-Sang Lee
Yingsong Li
Liu
Matteo Bruno Lodi
Biswa Binayak Mangaraj
Valentin Mateev
Ali Madani Mohammadi
Weidong Mu
Antonino Musolino
Amjad Omar
Balendu Kumar Pandey
Andrew Peterson
Jagadheswaran Rajendran
Natarajamani S.
Suganthi Santhanam
Sayidmarie
Fusun Oyman Serteller
Vladimir Stanković
Qusai Hadi Sultan
Marsellas Waller
Lu Wang
Steven Weiss
Gaobiao Xiao
Wentao Yuan
Xiaoyan Zhang
Yun-Qi Zhang

THE APPLIED COMPUTATIONAL ELECTROMAGNETICS SOCIETY JOURNAL

Vol. 37 No. 8 August 2022

TABLE OF CONTENTS

On Controlling the Passband and Stopband of UWB Band-Pass Filter

Tamer G. Abouelnaga[1,2] and Esmat A. Abdallah[1]

[1]Microstrip Circuits Department
Electronics Research Institute ERI, Cairo, Egypt

[2]Electrical Engineering Department
Higher Institute of Engineering and Technology HIET, Kafr Elsheikh, Egypt
Tamer@eri.sci.eg

Abstract – In this article, the passband, and stopband of quarter wavelength stubs-based Band Pass Filter (BPF) are controlled by a straightforward and new method. This method depends on inserting an attenuation pole and tuning the passband by a Circular Slot Ring Resonator (CSRR) and rectangular slot beneath the BPF's stubs. Hence, controlling the passband width without any further area usage is achieved. The stop-band rejection level and bandwidth are controlled by inserting Band Stop Filter (BSF) after the BPF such that the used rectangular slots beneath the stubs control the stop-band bandwidth. For verification, third-order Chebyshev BPF and Butterworth BSF filters are used. The proposed filter passband is chosen to cover the sub-6 GHz different 5G bands. The proposed BPF has an ultra-wide 3 dB passband of 2.97 GHz (2.35 GHz - 5.32 GHz) and a 20 dB stopband of 4.59 GHz (6.18-10.77 GHz). The proposed BPF filter is fabricated, measured, and the results are in good agreement with their simulated counterparts.

Index Terms – 5G, attenuation poles, Butterworth BSF, Chebyshev BPF, UWB.

I. INTRODUCTION

In many wireless communication systems, conventional microstrip Band Pass Filters (BPFs) are used due to their planar structure and ease of fabrication. For ultra-wideband applications, a Short-circuited stub Band Pass Filter (SBPF) may be a good candidate filter. Control of attenuation pole frequency of a BPF near the cutoff frequency results in a sharp rate of cutoff. The closer the attenuation poles to the cut-off frequency, the sharper the filter skirt, and the higher the selectivity. A lot of research had been done to control the passband width and achieve a sharp cutoff rate. In [1], two open stubs were proposed to control the attenuation pole frequency of a dual-mode circular microstrip ring resonator bandpass filter, keeping the bandwidth almost constant. In [2], a modified Chebyshev BPF with attenuation poles in the stopband was proposed. The insertion of attenuation poles was accomplished by connecting a lumped inductor or capacitor in series with a shunt-type coaxial transmission-line resonator. In [3], a fifth-order combline filter with two attenuation poles (transmission zeros) was proposed. The attenuation poles were controlled by dedicated resonators, which were coupled to non-resonating nodes.

In [4], UWB bandpass using ring filter was introduced. The ring filter was made to control the attenuation pole frequency by adjusting both the ring and the stub impedance.

In [5], a wideband BPF was constructed of two sections of three coupled lines separated by a nonuniform line resonator. One transmission zero was introduced at each edge of the desired passband, and one of the outer coupled lines of each section was shorted to the ground. The nonuniform resonator was constructed by attaching pair of capacitive open-ended stubs at its central location. Insertion of attenuation poles in all aforementioned BPFs needs more area and their development is somewhat difficult.

Also, an unwanted harmonic passband is observed at approximately three times the passband mid-band frequency, which is unsuitable for wireless receiver circuitry, and hence, suppression of spurious signals of the upper stopband is essential to be wide as possible [6].

To meet this requirement, various methods have been proposed [7–14]. In [7], stepped-impedance open stubs were added to the resonator ports to add another transmission zero to suppress the second harmonic frequency. Although, it had the advantages of size reduction, simplicity, and low cost. But it suffers from extra insertion loss and a 5.2 dB rejection level. In [8], an ultra-wideband microstrip BPF was obtained using two parallel coupled lines resonators centered by a T-inverted shape. This filter suffers from critical dimensions of

Submitted On: January 24, 2022
Accepted On: September 11, 2022

https://doi.org/10.13052/2022.ACES.J.370801

0.2 mm which will limit the power handling capability of the proposed filter. In [9], a metamaterial-based resonator was used to obtain a BPF. This filter had the advantages of size reduction and low cost, but it suffers from extra insertion loss and a 13 dB rejection level. In [10], suppression of spurious signals was done by a crown Band Stop Filter (BSF). This filter had good harmonic suppression, but its fractional bandwidth should be further increased. In [11], an ultra-wideband (UWB) microstrip band-pass filter was proposed by using the multi-mode resonator technique. The proposed structure was realized by three and two open and short stubs, respectively. This filter had good harmonic suppression, but its insertion loss should be decreased and suffers from critical dimensions of 0.1 mm which will lower its power capability. A dual Behaviour Resonator (DBR) filter was reported in [12]. BSF basic topology is used by interrupting the uniform transmission line with multiple unequal lengths of shunt stubs to enforce the emergence of dual passbands relying on multiple transmission zeros. This solution increases component count, circuit size, and power consumption. Also, it suffers from narrow fractional bandwidth.

In [13], to insert transmission zeros in the broadband filter, the coupling line was connected to a certain position on the resonator. Then the coupling strength was adjusted by the connecting position. This filter had good fractional bandwidth, but it suffered from extra insertion loss and a reduced rejection level of 5 dB. In [14], a cross-coupled line structure was used to obtain a broadband band-pass filter. Cross-coupled line structure was composed of parallel-coupled lines and an open stub. This filter had good insertion loss, but its fractional bandwidth should be further enhanced. In [15], an H-type sandwich slotline structure was employed to obtain the UWB passband filter. This filter had good fractional bandwidth, but its insertion loss and stopband rejection level should be further enhanced.

In this paper, any quarter-wavelength shorted stubs-based BPFs with any odd order could be used. The proposed method doesn't need any lumped elements or parasitic elements to control the performance. Also, it is simple and promising since no additional area usage is required. It is mainly depending on Defected Ground Structure (DGS) structure. The insertion of an attenuation pole at the lower passband edge is achieved by adding CSRR at the middle short stub of the BPF. The attenuation pole frequency is controlled by the ring radius. The whole passband width is controlled by adding a rectangular slot beneath the shorted stubs. For verification, a third-order Chebyshev BPF is used. The upper stopband rejection level is achieved by cascading the proposed third-order BPF with third-order Butterworth open stubs BSF. The stopband width of the BSF is controlled by adding two rectangular slots beneath the connecting lines of the BSF. Finally, the proposed BPF filter is fabricated, measured, and the results are compared with their simulated counterparts.

II. DESIGN PROCEDURE OF THE PROPOSED HARMONIC SUPPRESSED BPF

In this section, the proposed BPF is obtained firstly, by designing, analyzing, and optimizing a third-order Chebyshev bandpass filter BPF. Then the middle stub is loaded by Circular Slot Ring Resonator CSRR for realizing the attenuation pole at the lower stopband and close to the lower cutoff frequency. Then, a rectangular slot is added to control the passband width of the proposed BPF. Secondly, a third-order Butterworth BSF is designed, analyzed, and optimized at the upper stopband of the proposed BPF. Hence, an upper stopband with at least a 20 dB rejection level is achieved. Finally, both BPF and BSF are cascaded, BSF stopband width is controlled by adding two stubs below its connecting lines, and the resultant filter performance is investigated. For the proposed BPF, different frequency bands of sub-6 GHz 5G are chosen to be covered by the passband of the proposed BPF. From the latest published version of the 3GPP technical standard (TS 38.101), the sub-6 GHz bands for the 5G communications are classified into new radio bands such as n53 (2.483 – 2.495), n77 (3.3 GHz–4.2 GHz), n78 (3.3 GHz–3.8 GHz), and n79 (4.4 GHz–5 GHz) [16–17].

$$\begin{aligned}
\theta &= \frac{\pi}{2}\left(1-\frac{FBW}{2}\right),\\
d &= 2,\\
\frac{J_{1,2}}{Y_0} &= g_0\sqrt{\frac{d g_1}{g_2}}, \quad \frac{J_{n-1,n}}{Y_0} = g_0\sqrt{\frac{d g_1 g_{n+1}}{g_0 g_{n-1}}},\\
\frac{J_{i,i+1}}{Y_0} &= \frac{d\, g_0 g_1}{\sqrt{g_i\, g_{i+1}}} \; for\; i = 2\; to\; n-2,\\
N_{i,i+1} &= \sqrt{\left(\frac{J_{i,i+1}}{Y_0}\right)^2 + \left(\frac{d\, g_0 g_1 tan\,\theta}{2}\right)^2},\\
for\; i &= 1\; to\; n-1.
\end{aligned} \tag{1}$$

A. Proposed BPF

Third-order Chebyshev BPF is designed based on three shunt short-circuited stubs that are $\lambda_g/4$ long with connecting lines that are also $\lambda_g/4$ long, where λ_g is the guided wavelength at the mid-band frequency. CST Microwave Studio software is used for the simulation of different stages of the proposed filter. In this paper, the sub 6 GHz 5G frequency bands should be covered (2.4 GHz to 5 GHz). As a start, a three-pole Chebyshev short-circuited BPF centered at f_{mid} = 4.25 GHz with

Table 1: The prototype parameters of the BPF

g_0	g_1	g_2	g_3	g_4
1	0.85154	1.10315	0.85154	1

Table 2: The prototype layout dimensions

i	Z_i (Ω)	W_i (mm)	$\lambda_{gi}/4$ (mm)
1	25.3228	8.077	9.322
2	38.2373	4.544	8.914
3	25.3228	8.077	9.322
	$Z_{i,i+1}$ (Ω)	$W_{i,i+1}$ (mm)	$\lambda_{gi,i+1}/4$ (mm)
1	60.5	2.106	5.016
2	60.5	2.106	5.016

58.8% fractional bandwidth (FBW), (3 GHz - 5.5GHz), has been designed. This passband is chosen 600 MHz shifted forward and it will be shifted back through the fine-tuning process. For all the simulations FR-4 dielectric substrate is used, having a dielectric constant of 4.4, a thickness of 1.6 mm, and a loss tangent of 0.019. The design equations of short-circuited BPF, Fig. 1, can be found in equation 1 [18] as:

The characteristic admittance of the shunt stub:

$$Y_1 = g_0 Y_0 \left(1 - \frac{d}{2}\right) g_1 \, tan\, \theta + Y_0 \left(N_{1,2} - \frac{J_{1,2}}{Y_0}\right)$$

$$for\ i = 1,$$

$$Y_i = Y_0 \left(N_{i-1,i} + N_{i,i+1} - \frac{J_{i-1,i}}{Y_0} - \frac{J_{i,i+1}}{Y_0}\right)$$

$$for\ i = 2\ to\ n-1,$$

$$Y_n = Y_0 \left(g_n\, g_{n+1} - g_0\, g_1 \frac{d}{2}\right) tan\, \theta + Y_0 \left(N_{n-1,n} - \frac{J_{n-1,n}}{Y_0}\right)\ for\ i = n.$$

The characteristic admittance of the connecting lines is calculated as:

$$Y_{i,i+1} = Y_0 \left(\frac{J_{i,i+1}}{Y_0}\right)\ for\ i = 1\ to\ n-1,$$

where g_i is the element value of a ladder-type Chebyshev lowpass prototype filter given for a normalized cut-off and d is a dimensionless constant, which is assigned to a value that gives a convenient admittance level. For third-order BPF, Fig. 2 (a) shows the layout of the short-circuited BPF. For a passband ripple of 0.04321, the prototype parameters of the filter and the computed design widths and lengths are listed in Tables 1 and 2, respectively.

The width of the 50 ohms microstrip line is 2.752 mm. The conventional BPF layout, 3D geometry, and S-parameters are shown in Fig. 2 (b). The dimensions of the BPF that are given in Table 2 are simulated by CST and the obtained matching level and insertion loss are -4.2 dB and -2.6 dB, respectively at 3.6 GHz which indeed needs a geometry optimization process. Table 3 shows the optimized dimensions and Fig. 3 (b) shows the S-parameters of the optimized BPF. From Fig. 3 (b), the -10 dB passband extends from 2.65 GHz to 5.5 GHz with an insertion loss of 0.5 dB at the mid of the passband. The upper stopband rejection level degrades much at 7.7 GHz and further frequencies. Also, the n53 frequency band isn't covered and the lower stopband rejection level is at 5 dB at 2 GHz. To solve these problems, firstly, an attenuation pole at 2.4 GHz should be inserted.

Table 3: Optimized dimensions of the BPF prototype

i	Z_i (Ω)	W_i (mm)	$\lambda_{gi}/4$ (mm)
1	55.4889	2.472	9.322
2	39.5408	4.32	8.914
3	55.4889	2.472	9.322
	$Z_{i,i+1}$ (Ω)	$W_{i,i+1}$ (mm)	$\lambda_{gi,i+1}/4$ (mm)
1	49.4884	3.018	5.016
2	49.4884	3.018	5.016

B. Insertion of an attenuation pole at 2.4 GHz

The Circular Slot Ring Resonator CSRR when placed and centered at the edge of the middle-shorted stub of the BPF will act as a stopband filter at the desirable frequency that is related to its dimensions. The CSRR BSF performance is investigated in Fig. 3 (a) where the same BPF dimensions are used. The effect of changing CSRR inner radius R is investigated, keeping the slot width at 0.6 mm. Figure 3 (a) shows that increasing the inner CSRR radius from 3 mm to 6 mm will decrease the stopband frequency from 3.36 GHz to 1.85 GHz. This wide range of frequencies will add a new freedom degree to the designing process. Empirical equation 2 describes the relationship between the inner radius R in mm and the stopband frequency f_s in GHz as $3 \leq R \leq 6$ as:

$$f_s \approx 4.65 - 0.73R + 0.04R^2. \quad (2)$$

Based on Fig. 3 (a), inner and outer radii of 4 mm and 4.6 mm, respectively are chosen for 2.4 GHz CSRR BSF. Hence, an attenuation pole frequency of 2.4 GHz and rejection level of 50 dB is presented. Figure 3 (b) shows the S-parameters of the proposed BPF which is loaded with the CSRR. The passband extends from 3.23 GHz to 5.57 GHz with a lower rejection level of 50 dB at 2.4 GHz and a lower cutoff frequency of 2.89 GHz which gives a sharp filter skirt, and good selectivity at the lower passband edge. The loaded BPF still suffers from a low rejection level at the upper stopband starting from 8 GHz and further frequencies. Also, the n53 band is not covered yet by

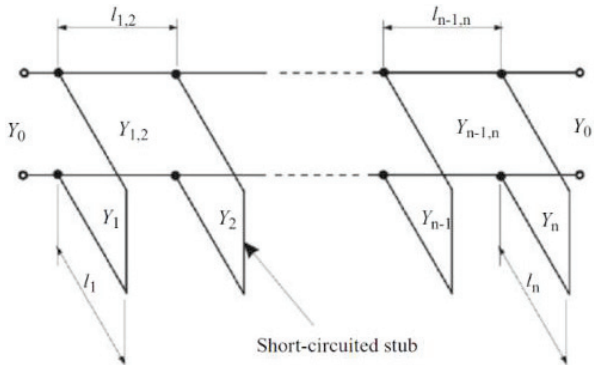

Fig. 1. Transmission line BPF with quarter-wavelength short-circuited stubs.

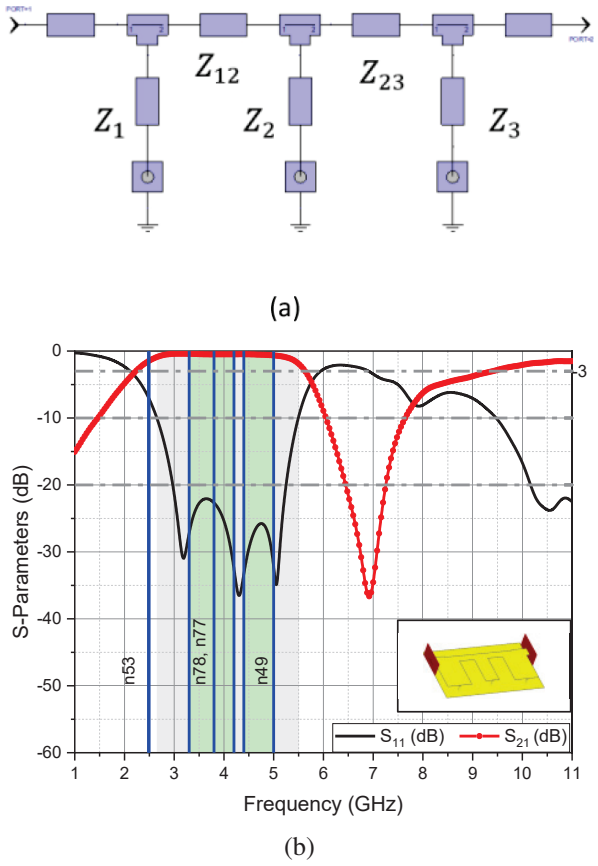

Fig. 2. Conventional short-circuited BPF (a) layout and (b) simulated S-parameters.

the −10 dB passband. Adding a rectangular slot just below the three shorted stubs of the proposed BPF will control the passband width since it will directly affect the electrical length of the three shorted stubs [19–20].

C. Controlling the passband width of the BPF

The rectangular slot's length effect on the −3 dB passband is investigated in Fig. 4 (a) where the slot

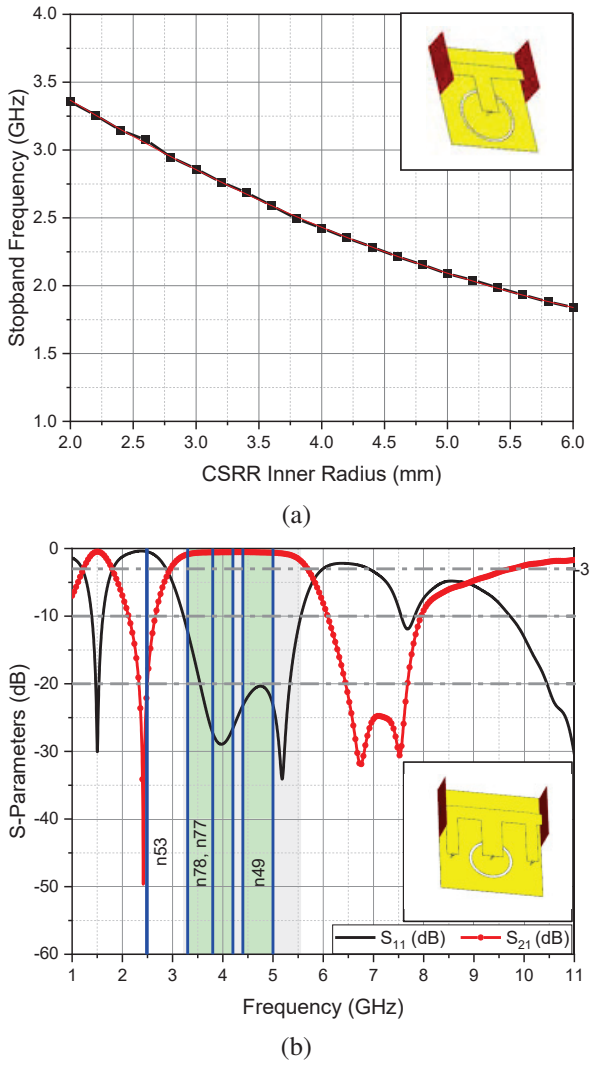

Fig. 3. (a) CSRR BSF frequency versus inner radius. (b) Proposed BPF loaded with CSRR S-parameters.

width is kept at 1 mm and centered at 6.43 mm from the shorted middle stub edge of the proposed BPF. As predicted by Fig. 4 (a), the lower cutoff frequency is decreased as the slot length is increased. The empirical equations 3 and 4 describe the upper 3 dB frequency f_u in GHz and the lower 3 dB frequency in GHz f_l as slot length l ranges from 8 mm to 20 mm as:

$$f_l \approx 3.1 - 0.03l - 0.001l^2, \tag{3}$$

$$f_u \approx 5.7 - 0.24e^{-2\left(\frac{l-15.5}{1.7}\right)^2}. \tag{4}$$

A slot length of 20 mm is the best choice to obtain a −3 dB passband range which extends from 2.22 GHz to 5.71 GHz as shown in Fig. 4 (a). It can be noticed that the n53 band is covered by the proposed BPF by the −10 dB passband, Fig. 4 (b). From Fig. 4 (b), the spurious −3 dB

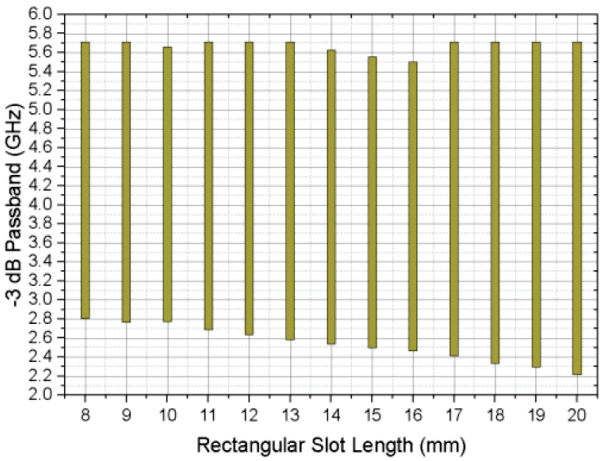

(a)

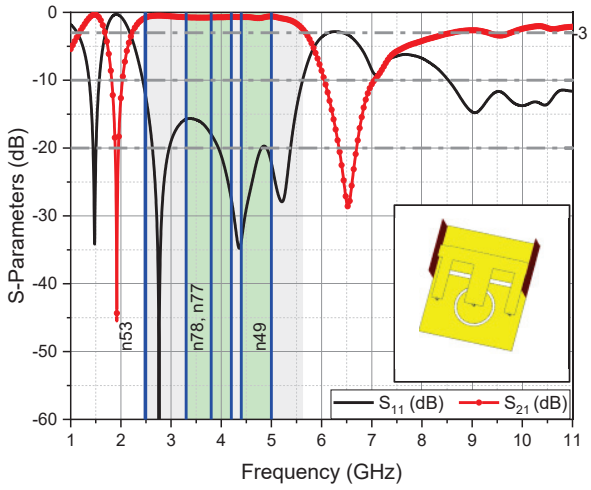

(b)

Fig. 4. Proposed BPF loaded with CSRR (a) rectangular slot length effect and (b) S-parameters.

passband is observed at 8.5 GHz to 11GHz and further. The spurious response should be eliminated to avoid passband interference. Hence, in the next section, a third-order bandstop Butterworth filter will be designed and then the proposed BPF is cascaded with it. This combination achieves a wide stopband, high rejection level, and low insertion loss.

D. BSF design and analysis

Butterworth BSF was chosen to reject the harmonics in the frequency band that extends from 6 GHz to 12 GHz with a mid-stopband frequency of 9 GHz. The BSF was developed using three shunt quarter-wavelength open stubs with two pairs of symmetrical connecting microstrip lines that are quarter-wavelength long at the mid-stopband frequency. The design procedure started with a chosen ladder-type Butterworth lowpass prototype of order three, Table 4.

Table 4: Third-order Butterworth lowpass filter parameters with 3dB attenuation

g_0	g_1	g_2	g_3	g_4
1	1	2	1	1

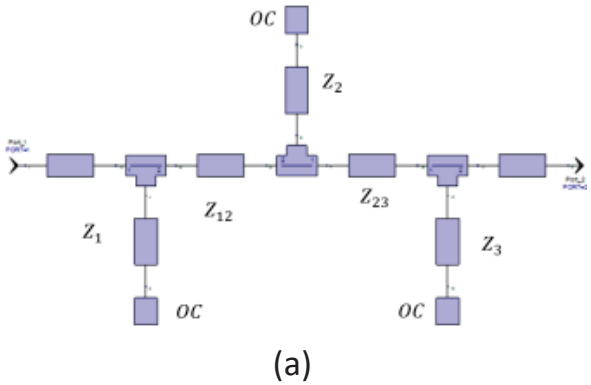

(a)

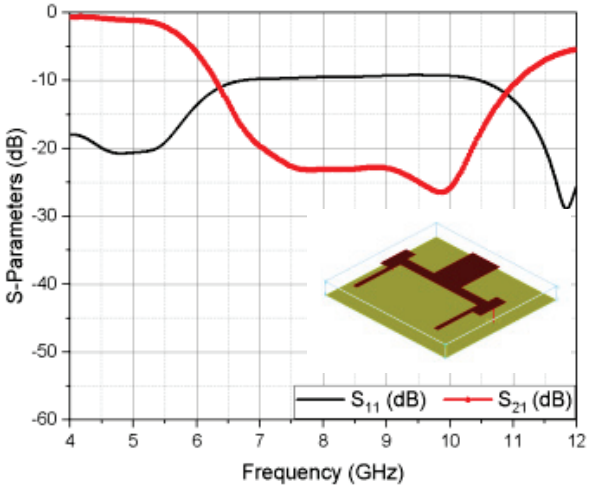

(b)

Fig. 5. Third-order optimized Butterworth Open-circuited BSF (a) layout and (b) S-parameters.

The design equations for the third-order filter can be found in [13]. The BSF layout is shown in Fig. 5 (a). Table 5 shows the layout dimensions of the BSF. A rejection of −4.5 dB is obtained at the lower edge of the stopband (6 GHz). An optimization process was needed to enhance the lower stopband edge rejection. Table 6 shows the optimized dimensions of the BSF. Figure 5 (b) shows the optimized S-parameters results where the lower bandstop edge (6 GHz) reaches −6 dB instead of −4.5 dB which was obtained by the BSF prototype.

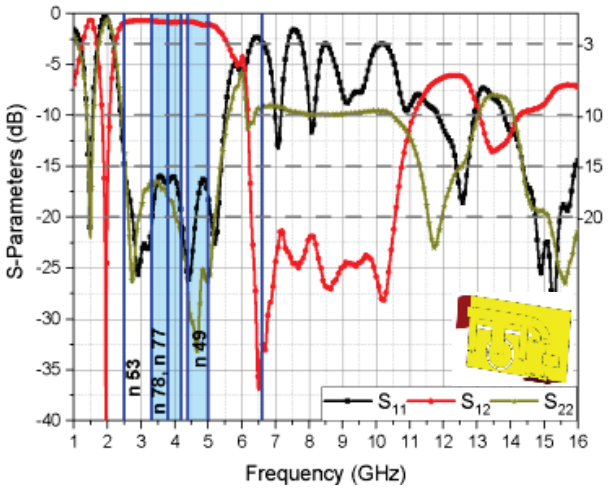

Fig. 6. Proposed BPF simulated S-parameters.

Table 5: Third-order Butterworth BSF dimensions

i	Z_i (Ω)	W_i (mm)	$\lambda_{gi}/4$ (mm)
1	135.709	0.214	3.981
2	43.4559	3.732	4.446
3	135.709	0.214	3.981
	$Z_{i,i+1}$ (Ω)	$W_{i,i+1}$ (mm)	$\lambda_{gi,i+1}/4$ (mm)
1	78.304	1.224	2.852
2	78.304	1.224	2.852

E. Cascading the proposed BPF with BSF

To eliminate the spurious response, the modified short-circuited BPF is cascaded with the open-circuited BSF. Hence, the spurious response can be significantly suppressed. Figure 6 shows that a 20 dB rejection level is obtained at the upper stopband which extends from 6.26 GHz to 10.56 GHz. For further extension of the stopband of 20 dB rejection level, two rectangular slots are added and centered beneath the connecting lines of the BSF as shown in Fig. 7 (a), (same as sub-section c). The slot dimensions are 5 mm in length and 2 mm in width. From Fig. 7 (b), the upper stopband has extended from 6.18 GHz to 10.76 GHz with a 20 dB rejection level.

Table 6: Optimized dimensions of Butterworth BSF

i	Z_i (Ω)	W_i (mm)	$\lambda_{gi}/4$ (mm)
1	113.346	0.43	3.981
2	48.7056	3.1	4.446
3	113.346	0.43	3.981
	$Z_{i,i+1}$ (Ω)	$W_{i,i+1}$ (mm)	$\lambda_{(gi,i+1)}/4$ (mm)
1	86.1602	0.969	2.852
2	86.1602	0.969	2.852

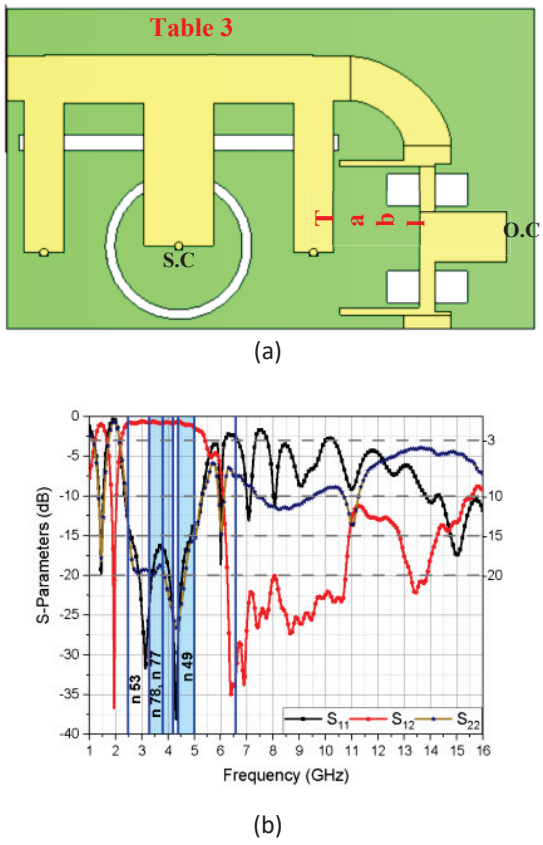

Fig. 7. Proposed extended upper stopband BPF (a) geometry and (b) simulated S-parameters.

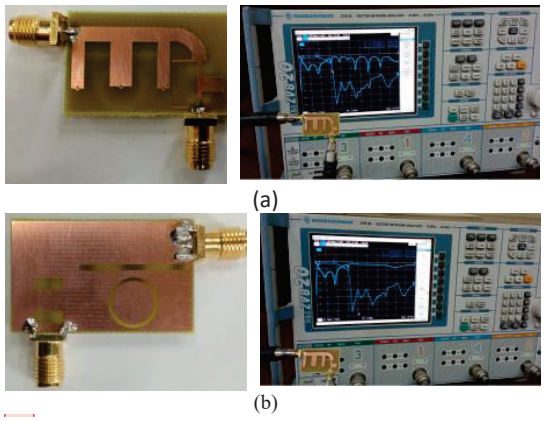

Fig. 8. Fabricated prototype of the proposed BPF (a) top view and (b) bottom view.

III. FABRICATION AND MEASUREMENT

For verification purposes, the proposed BPF filter is fabricated on an FR-4 substrate. The total electrical size of the filter is $0.74\lambda_g \times 0.46\lambda_g$. Figure 8 (a) and (b) show the fabricated BPF prototype, top, and bottom views. S- parameters of the proposed filter is measured

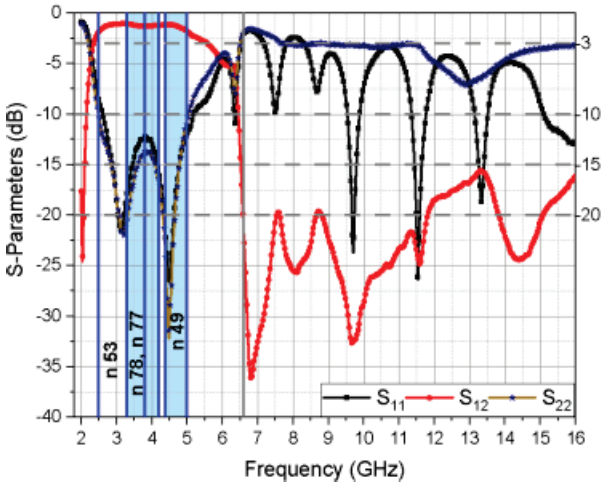

Fig. 9. Proposed BPF measured S-parameters.

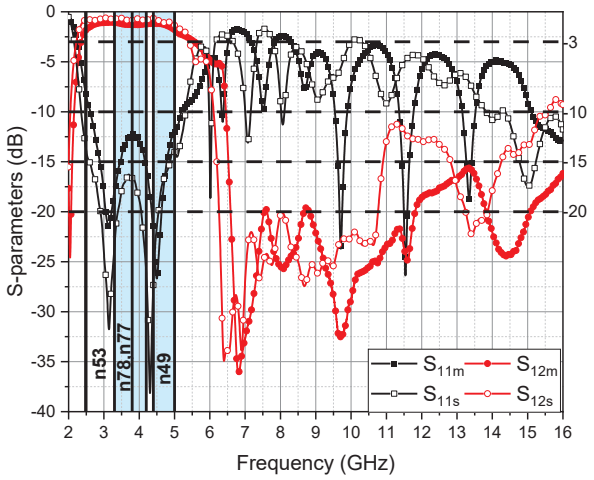

Fig. 10. Proposed BPF measured and simulated S-parameters.

by using the Rohde & Schwarz ZVB20 vector network analyzer (VNA). Figures 7 (b), 9, and 10 show the simulated and measured S-parameters of the proposed BPF.

It can be noticed that the simulated and measured upper stopband are better than 20 dB up to $2.9f_{mid}$ and better than 20 dB up to $3f_{mid}$, respectively. The simulated and measured 3-dB fractional bandwidth are 86.8 % and 81.3 %, respectively. The simulated and measured values of insertion loss at the center frequency of the passband are 0.77 dB and 1.3 dB, respectively. The proposed BPF is compared in Table 7 with previous designs' performance considering; the substrate dielectric constant ε_r, substrate thickness h, passband center frequency f_{mid}, insertion loss (IL), 3-dB fractional bandwidth (FBW), and upper stopband response at Minimum Rejection Level (MRL). One can

Table 7: Comparisons' results for previous BPFs

Filter Shape	ε_r	h (mm)	f_{mid} (GHz)	IL (dB)	$3dB\ FBW$ $(\%)$	Upper Stopband @ MRL (dB)
Ref. [7]	4.3	1.5	1.42	1.5	18.6	$2.8f_{mid}$ @ 5.2
Ref. [8]	4.4	1.58	3.5	0.3	58	$2.7f_{mid}$ @ 22
Ref. [9]	4.4	1.6	4.19	1.31	68	$3.1f_{mid}$ @ 13
Ref. [10]	4.4	1.6	2	0.4	49.7	$3.5f_{mid}$ @ 20
Ref. [11]	3.55	0.508	7.35	1.1	88.4	$2.5f_{mid}$ @ 20
Ref. [13]	6.15	0.635	1.18	2	68	$3.4f_{mid}$ @ 5
Ref. [14]	2.2	0.508	4.5	0.7	42	$1.5f_{mid}$ @ 18
Ref. [15]	-	-	5.12	2.5	132	$1.9f_{mid}$ @ 17
This work [S]	4.4	1.6	3.8	0.77	86.8	$2.9f_{mid}$ @ 20
This work [M]	4.4	1.6	3.9	1.3	81.3	$3f_{mid}$ @ 20

notice that the proposed BPF has simultaneously, simulated a wide upper stopband, high suppression level, and low insertion loss. Also, the low-cost advantage is kept by using the FR4 substrate.

IV. CONCLUSION

A simple and new method of controlling the passband and stopband of any quarter wavelength short-stub-based BPF had been introduced. For verification, a third-order Chebyshev BPF and 5G different bands are chosen. The conventional short-circuited BPF was modified by inserting an attenuation pole near its lower cutoff frequency and then controlling the passband by adding a rectangular slot. The modified BPF is cascaded with open-circuited BSF. Third-order for both bandpass and BSFs was chosen for miniaturization purposes. In the proposed BPF, the combination of the short-circuited BPF, open-circuited BSF, CSRR, and rectangular slots had been used to suppress spurious responses. The wide upper stopband with 20 dB harmonic suppression, low insertion loss, compactness along with its low cost makes it suitable for 5G sub 6 GHz applications as well as other wireless communication systems such as navigation and radar applications.

REFERENCES

[1] A. C. Kundu and I. Awai, "Control of attenuation pole frequency of a dual-mode microstrip ring resonator bandpass filter," *IEEE Transactions on Microwave Theory and Techniques*, vol. 49, no. 6, pp. 1113-1117, 2001.

[2] J. S. Lim and D. C. Park, "A modified Chebyshev bandpass filter with attenuation poles in the stopband," *IEEE Transactions on Microwave Theory and Techniques*, vol. 45, no. 6, pp. 898-904, 1997.

[3] S. Amari and G. Macchiarella, "Synthesis of inline filters with arbitrarily placed attenuation poles by using non resonating nodes," *IEEE Transactions on Microwave Theory and Techniques*, vol. 53, no. 10, pp. 3075-3081, 2005.

[4] H. Ishida and K. Araki, "Design and analysis of UWB bandpass filter with ring filter," *IEEE MTT-S International Microwave Symposium Digest (IEEE Cat. No. 04CH37535)*, vol. 3, pp. 1307-1310, 2004.

[5] H. N. Shaman, "New S-band bandpass filter (BPF) with wideband passband for wireless communication systems," *IEEE Microwave and Wireless Components Letters*, vol. 22, no. 5, pp. 242-244, 2012.

[6] J. S. Hong and M. J. Lancaster, *Microstrip Filters for RF/Microwave Applications,* John Wiley & Sons, 2004.

[7] T. G. Abouelnaga and A. S. Mohra, "Novel compact harmonic-rejected ring resonator-based bandpass filter," *Progress in Electromagnetics Research C*, vol. 74, pp. 191-201, 2017.

[8] L. Yechou, A. Tribak, M. Kacim, J. Zbitou, and A. Mediavilla, "A novel wideband bandpass filter using coupled lines and T-shaped transmission lines with wide stopband on low-cost substrate," *Progress in Electromagnetics Research C*, vol. 67, pp. 143-152, 2016.

[9] S. Chaimool and P. Akkaraekthalin, "Miniaturized wideband bandpass filter with wide stopband using metamaterial-based resonator and defected ground structure," *Radioengineering*, vol. 21, no. 2, pp. 611-616, 2012.

[10] T. Beiki and M. Hosseinipanah, "Harmonic suppression in short-circuited stub bandpass filter by means of a new miniaturized bandstop filter," *Analog Integrated Circuits and Signal Processing*, vol. 96, no. 3, pp. 589-596, 2018.

[11] M. Danaeian, E. Zarezadeh, M. Gholizadeh, A. Moznebi, and J. Khalilpour, "A compact and sharp rejection ultra-wideband bandpass filter based on short and open stub-loaded multiple mode resonators," *Journal of Electrical Engineering & Technology*, vol. 15, no. 1, pp. 469-476, 2020.

[12] C. Quendo, E. Rius, and C. Person, "An original topology of dual-band filter with transmission zeros," *IEEE MTT-S International Microwave Symposium Digest*, vol. 2, pp. 1093-1096, 2003.

[13] X. Liu, Z. Zhang, and G. Su, "A broadband filter with two transmission zeros adopting a new design method," *International Journal of RF and Microwave Computer-Aided Engineering,* vol. 30, no. 2, 2020.

[14] D. S. La, X. Guan, H. Li, Y. Li, and J. Guo, "Design of broadband band-pass filter with cross-coupled line structure," *International Journal of Antennas and Propagation*, vol. 2020, pp. 1-5, 2020.

[15] J. Sun and G. R. Li, "A balanced ultra-wideband bandpass filter based on H-type sandwich slotline," *International Journal of RF and Microwave Computer-Aided Engineering*, vol. 31, no. 5, 2021.

[16] T. G. Abouelnaga and M. Shokair, "Design of 10 $\times$10 massive MIMO array in sub-6GHz smartphone for 5G applications," *Progress in Electromagnetics Research B*, vol. 91 pp. 97-114, 2021.

[17] *5G NR Specifications, Document TS* 38.101-1 V15.4.0 3GPP Release 15, 2018.

[18] J. S. Hong and M. J. Lancaster, *Microstrip Filters for RF/Microwave Applications,* John Wiley & Sons, 2004.

[19] D. Ahn, J. S. Park, C. S. Kim, J. Kim, Y. Qian, and T. Itoh, "A design of the low-pass filter using the novel microstrip defected ground structure," *IEEE Transactions on Microwave Theory and Techniques*, vol. 49, no. 1, pp. 86-93, 2001.

[20] M. Challal, A. Boutejdar, M. Dehmas, A. Azrar, and A. Omar, "Compact microstrip low-pass filter design with ultra-wide reject band using a novel quarter-circle DGS shape," *Applied Computational Electromagnetics Society (ACES) Journal,* vol. 27, no. 10, pp. 808-815, 2012.

Tamer Gaber Abouelnaga was born in Nov. 1976. He received his B.Sc. degree (1994–1999, honors degree) in Electronics Engineering from Menofiya University, Egypt, M.Sc. degree (2002–2007), and Ph.D. degree (2007–2012) in Electronics and Communications from Ain Shams University. He works as a Researcher (2012–2017) and an Associate Professor (2018 to present) in Microstrip Circuits Department, Electronics Research Institute, Egypt. He works as Students Affairs Vice Dean (2018–2019) and Community Service and Environmental Development Vice Dean (2019 till now) – Higher Institute of Engineering and Technology – Kafr Elsheikh City. He had published 38 papers, 26 papers in peer-refereed journals, and 12 papers in international

conferences regarding antennas, couplers, filters, and dividers for different microwave applications.

Esmat A. Abdallah (Senior Member, IEEE) graduated from the Faculty of Engineering, Cairo University, Giza, Egypt in 1968. She received her M.Sc. and Ph.D. degrees from Cairo University in 1972, and 1975, respectively. She was nominated as Assistant Professor, Associate Professor, and Professor in 1975, 1980, and 1985, respectively. In 1989, she was appointed President of the Electronics Research Institute ERI, Cairo, Egypt, a position she held for about ten years. She became the Head of the Microstrip Department, ERI, from 1999 to 2006. Currently, she is at the Microstrip Department, Electronics Research Institute, Cairo, Egypt.

She has focused her research on microwave circuit designs, planar antenna systems, and nonreciprocal ferrite devices, and recently on EBG structures, UWB components, and antenna and RFID systems. She acts as a single author and as a co-author on more than 285 research papers in highly cited international journals and proceedings of international conferences. She has conducted many contracted projects (32 research and development projects) as PI funded by many funding agencies, such as the Academy of Scientific Research and Technology (ASRT), National Telecommunication Regulatory Authority (NATRA), National Science Foundation (NSF), Science and Technology Development Fund (STDF), and National Authority for Remote Sensing and Space Sciences and Information Technology Academia Collaboration (ITAC). She has six books and seven patents. She supervised more than 85 Ph.D. and M.Sc. theses. She is a member of the National Council of Communication and Information Technology.

Analytical Approximations for the Maximum-to-mean Ratio of the E-field in a Reverberation Chamber: A Review

Qian Xu[1], Rui Jia[2], Lifei Geng[2], Hao Guo[2], and Yongjiu Zhao[1]

[1]College of Electronic and Information Engineering
Nanjing University of Aeronautics and Astronautics, Nanjing, 211106, China
emxu@foxmail.com, yjzhao@nuaa.edu.cn

[2]State Key Laboratory of Complex Electromagnetic Environment Effects on Electronic and Information System
Luo Yang, China
jiarui315@163.com

***Abstract* –** The expected value of the maximum value of the rectangular E-field is important in radiated susceptibility testing in a reverberation chamber. In this paper, different forms of equations for the maximum-to-mean ratio of the rectangular E-field are reviewed. Important derivations are summarized and detailed. It is interesting to note that some series which could be difficult to deal with from mathematics could be solved efficiently from physical point of view. The relationship between the independent sample number N and the parameters in generalized extreme value distribution is also given.

***Index Terms* –** maximum-to-mean ratio, reverberation chamber, statistical electromagnetics.

I. INTRODUCTION

Reverberation Chambers (RCs) have been widely used in electromagnetic compatibility (EMC) testing [1]. Compared with an anechoic chamber, no radio absorber is used on the walls, thus a rich multipath environment can be created in an RC. By rotating the mechanical stirrers in an RC, statistically uniform and isotropic electromagnetic fields can be created. A typical measurement setup is illustrated in Fig. 1. For the radiated susceptibility testing in an RC, the maximum E-field is of interest [1], [2] as the device under test (DUT) could be malfunctioned by the maximum E-field.

In an RC, statistical electromagnetics are used to characterize the field properties. The probability density function (PDF) and the cumulative distribution function (CDF) of the maximum rectangular E-field have been given in [2]–[5]. Approximate analytical equations have also been given in [4], [5] for large independent sample number N. Different forms of equations exist, and the similarities and equivalencies among them have not been summarized.

In this paper, we review the analytical equations for the expected value and the standard deviation of the maximum E-fields in literatures. Numerical results are calculated and compared with different forms of analytical equations.

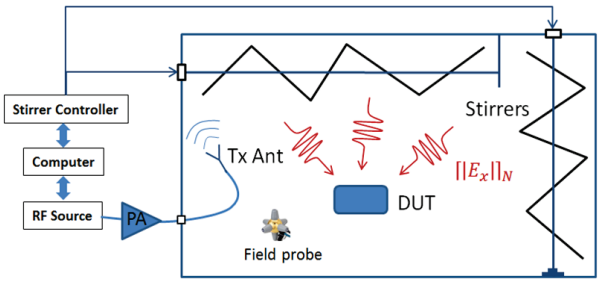

Fig. 1. A schematic plot of radiated susceptibility in an RC.

II. THEORY

The mean rectangular E-field strength in an RC is easy to estimate. However, the maximum rectangular E-field strength is of interest in many scenarios for EMC testing. The maximum-to-mean ratio of the rectangular E-field in an RC has been well studied in [2]–[5]. The PDF and the CDF of the maximum rectangular E-field in an RC are [2]–[5]:

$$p(x) = \frac{Nx}{\sigma^2}\left[1-\exp\left(\frac{-x^2}{2\sigma^2}\right)\right]^{N-1}\exp\left(\frac{-x^2}{2\sigma^2}\right), \quad (1)$$

and:

$$F(x) = \left[1-\exp\left(\frac{-x^2}{2\sigma^2}\right)\right]^{N}, \quad (2)$$

where N is the independent sample number, x represents the maximum value of the rectangular E-field $x = \lceil |E_x| \rceil_N$, and $\lceil \cdot \rceil_N$ represents the maximum value from N samples. The PDF of the normalized $\lceil |E_x| \rceil_N$ can be obtained by setting $\sigma = \sqrt{2/\pi}$, as the mean value of $|E_x|$ is $\sigma\sqrt{\pi/2}$. For different N, the PDF plots are illustrated in Fig. 2. It can be observed that when N

Submitted On: December 17, 2021
Accepted On: August 18, 2022

https://doi.org/10.13052/2022.ACES.J.370802

increases, the expected value of the maximum E-field increases. The confidence interval of maximum E-field can be calculated from CDF in (2) [1], [5].

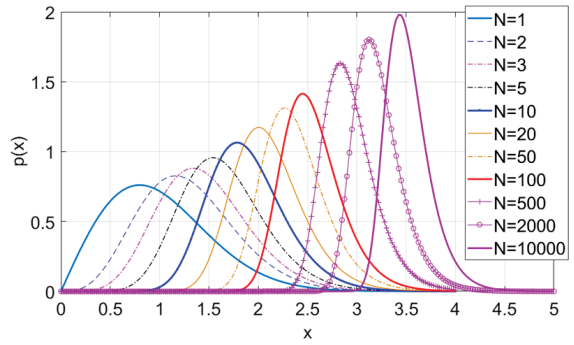

Fig. 2. PDF plots of the normalized maximum E-field (normalized to the mean value $\langle |E_x| \rangle$) for different independent sample number N.

The expected value of the maximum-to-mean ratio of the rectangular E-field be expressed as [2], [5]:

$$\alpha(N) = \frac{\langle \lceil |E_x| \rceil_N \rangle}{\langle |E_x| \rangle} = \frac{\int_0^\infty N x^2 \left[1 - \exp\left(\frac{-x^2}{2}\right)\right]^{N-1} \exp\left(\frac{-x^2}{2}\right) dx}{\sqrt{\pi/2}}. \tag{3}$$

However, numerical integration is required to evaluate (3) using a computer, an approximate equation could be necessary to have a quick estimation for a given N. By applying the binomial theorem:

$$\begin{aligned}\alpha(N) &= \frac{\int_0^\infty N x^2 \sum_{k=0}^{N-1} \binom{N-1}{k} \left[-\exp\left(\frac{-x^2}{2}\right)\right]^k \exp\left(\frac{-x^2}{2}\right) dx}{\sqrt{\pi/2}} \\ &= \frac{\sum_{k=0}^{N-1} N \binom{N-1}{k} (-1)^k \int_0^\infty x^2 \left[\exp\left(\frac{-x^2}{2}\right)\right]^{k+1} dx}{\sqrt{\pi/2}} \\ &= \frac{\sum_{k=0}^{N-1} N \binom{N-1}{k} \frac{(-1)^k \sqrt{\pi}}{(k+1)\sqrt{2k+2}}}{\sqrt{\pi/2}} \\ &= \sum_{k=0}^{N-1} \frac{N!(-1)^k}{(N-k-1)!\,(k+1)!\sqrt{k+1}} \\ &= \sum_{k=0}^{N-1} s(k). \end{aligned} \tag{4}$$

Although (3) is converted to the summation of a finite series, (4) is still not easy to evaluate. Symbolic calculation is required to maintain high precision, as the magnitude of $s(k)$ resonant drastically. A plot of $|s(k)|$ is illustrated in Fig. 3, as can be seen, when N is large, the magnitude of the series varies from 10^0 to 10^{30}. If there is no special treatment for $s(k)$, numerical calculation is easy to diverge for large N and wrong results could be obtained.

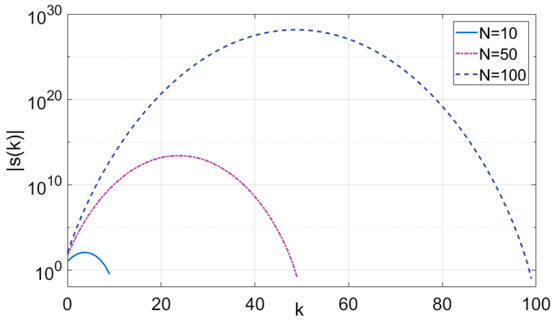

Fig. 3. Plots of $s(k)$ for different N, symbolic calculation is used to keep precision.

It seems we cannot go further from (4). Instead, we can approach it physically. Suppose an E-field probe (the Rx antenna) is placed inside a well-stirred RC, it can be found that the maximum received power ($\max(P_{\text{rRC}}) = \lceil P_{\text{rRC}} \rceil_N$) can be expressed as [2]:

$$\sqrt{\max(P_{\text{rRC}})} \approx \frac{\max(|E_x|)\ \lambda \sqrt{\eta_{\text{Rx}}}}{8\pi\sqrt{5}}, \tag{5}$$

where $|E_x|$ represents the tangential component of the E-field in an RC ($\langle |E_x|^2 \rangle = 4\langle |E_x| \rangle^2/\pi$, $\max(|E_x|) = \lceil |E_x| \rceil_N$), λ is the wavelength, and η_{Rx} is the efficiency (including mismatch loss) of the Rx antenna respectively. It is interesting to compare it with received power in an anechoic chamber (AC):

$$\sqrt{P_{\text{rAC}}} = \frac{E_{\text{AC}} \lambda \sqrt{\eta_{\text{Rx}}}}{8\pi\sqrt{5}} \sqrt{2D/3}, \tag{6}$$

where E_{AC} is the magnitude of the incident E-field and D is the directivity of the Rx antenna in the direction of the incident wave. Not surprisingly, D plays an important role in an AC. it can be found that when $D = 3/2$, (5) and (6) give the same results. This means that if the E-field probe is calibrated in an AC, only when the directivity of the E-field probe is 3/2 (electrically small dipole antenna), the measured E-field in an RC is statistically accurate. When the frequency is high, the E-field probe is no longer an electrically small antenna; the measured mean E-field in an RC using the free space antenna factor is no longer accurate and η_{Rx} is actually the key parameter. This effect is well known in standards related to RC measurements [1]. At high frequencies, an antenna is normally used to monitor the E-fields inside an RC instead of using an E-field probe.

From statistical analysis in [2]:

$$\frac{\max(P_{\text{rRC}})}{\langle P_{\text{rRC}} \rangle} \approx \sum_{k=1}^{N} \frac{1}{k}. \tag{7}$$

Note that [2], [7]:

$$\langle P_{\mathrm{rRC}}\rangle = \frac{1}{2}\frac{E_0^2}{\eta}\frac{\lambda^2}{4\pi}\eta_{\mathrm{Rx}} = \frac{3}{2}\frac{\langle|E_x|^2\rangle}{\eta}\frac{\lambda^2}{4\pi}\eta_{\mathrm{Rx}} = \frac{6\langle|E_x|\rangle^2}{\pi\eta}\frac{\lambda^2}{4\pi}\eta_{\mathrm{Rx}}. \quad (8)$$

From (5), (7) and (8) we have:

$$\max(|E_x|) \approx \frac{8\pi\sqrt{5}}{\lambda\sqrt{\eta_{\mathrm{Rx}}}}\sqrt{\frac{6\langle|E_x|\rangle^2}{\pi\eta}\frac{\lambda^2}{4\pi}\eta_{\mathrm{Rx}}\sum_{k=1}^{N}\frac{1}{k}}. \quad (9)$$

Thus for large *N:*

$$\alpha(N) \approx \frac{\max(|E_x|)}{\langle|E_x|\rangle} \approx \sqrt{\frac{4}{\pi}\sum_{k=1}^{N}\frac{1}{k}}. \quad (10)$$

The problem is now converted to the partial sum of the harmonic series. The following equation can be used [8]:

$$\sum_{k=1}^{N}\frac{1}{k} = \gamma + \psi_0(N+1), \quad (11)$$

where $\gamma \approx 0.5772$ is the Euler-Mascheroni constant, $\psi_0(x)$ is the digamma function:

$$\psi_0(N+1) \approx \ln N + \frac{1}{2N} - \sum_{n=1}^{\infty}\frac{B_{2n}}{2nN^{2n}} = \ln N + \frac{1}{2N} - \frac{1}{12N^2} + \frac{1}{120N^4} - \frac{1}{252N^6} + \cdots,$$

and B_{2n} is the Bernoulli number $\frac{x}{(e^x-1)} = \sum_{n=0}^{\infty}\frac{B_n x^n}{n!}$. Thus we have:

$$\alpha(N) \approx \sqrt{\frac{4}{\pi}\left(\gamma + \ln N + \frac{1}{2N} - \frac{1}{12N^2} + \frac{1}{120N^4} - \frac{1}{252N^6} + \cdots\right)}. \quad (12)$$

Now we have obtained an analytical approximation for (3). In [4], the CDF value of 0.5 is used to calculate the expected value:

$$\alpha(N) \approx \sqrt{\frac{4}{\pi}\ln\frac{1}{\left[1-0.5^{\frac{1}{N}}\right]}}. \quad (13)$$

In [1] and [5], a similar expression is given with $\alpha(N) \approx \sqrt{\frac{4}{\pi}\left[0.5772 + \ln(N+1) - \frac{1}{2(N+1)}\right]}$ with slightly different parameters. Another approximation is given in [8] for the partial sum of harmonic series

$$\sum_{k=1}^{N}\frac{1}{k} \approx (2N+1)\tan^{-1}\left(\frac{1}{2N+1}\right) + \frac{1}{2}\ln\left(\frac{2N^2+2N+1}{2}\right) + \frac{56N^6+168N^5+140N^4-42N^2-14N-1}{2520(2N^2+2N+1)^7} - \frac{6N^2+6N+1}{180(2N^2+2N+1)^3} + \gamma - 1. \quad (14)$$

A comparison of $\alpha(N)$ is given in Fig. 4 (a) using (12)-(14), (12) is truncated with 3 terms, while the exact value is calculated using symbolic calculation in (4). The difference between (12)-(14) and the exact values (the error plots) are illustrated in Fig. 4 (b), respectively. As can be seen, (12) and (14) give smaller errors than (13). However, they all give good approximations when *N* is large.

For the approximate value of the relative standard deviation of $\lceil|E_x|\rceil_N$, we can start from the definition

$$\begin{aligned}\mathrm{std}_{\mathrm{rel}}(\lceil|E_x|\rceil_N) &= \frac{\sqrt{\int_0^{\infty}x^2p(x)\,dx - \frac{\pi}{2}\alpha(N)^2}}{\alpha(N)\sqrt{\frac{\pi}{2}}} \\ &= \frac{\sqrt{\sum_{k=0}^{N-1}N\binom{N-1}{K}(-1)^k\int_0^{\infty}x^3\left[\exp\left(\frac{-x^2}{2}\right)\right]^{k+1}dx - \alpha(N)^2}}{\alpha(N)\sqrt{\frac{\pi}{2}}} \\ &= \frac{\sqrt{\sum_{k=0}^{N-1}\frac{N!(-1)^k 2}{(N-k-1)!(k+1)!(k+1)} - \frac{\pi}{2}\alpha(N)^2}}{\alpha(N)\sqrt{\frac{\pi}{2}}} \\ &= \frac{\sqrt{2\sum_{k=1}^{N}\frac{1}{k} - \frac{\pi}{2}\alpha(N)^2}}{\alpha(N)\sqrt{\frac{\pi}{2}}} \\ &= \sqrt{\frac{4}{\pi}\frac{\sum_{k=1}^{N}\frac{1}{k}}{\alpha(N)^2} - 1}. \end{aligned} \quad (15)$$

It seems we cannot go further from (15). To obtain the approximate value of (15), a different approach can be used [5]. We start from the relative standard deviation

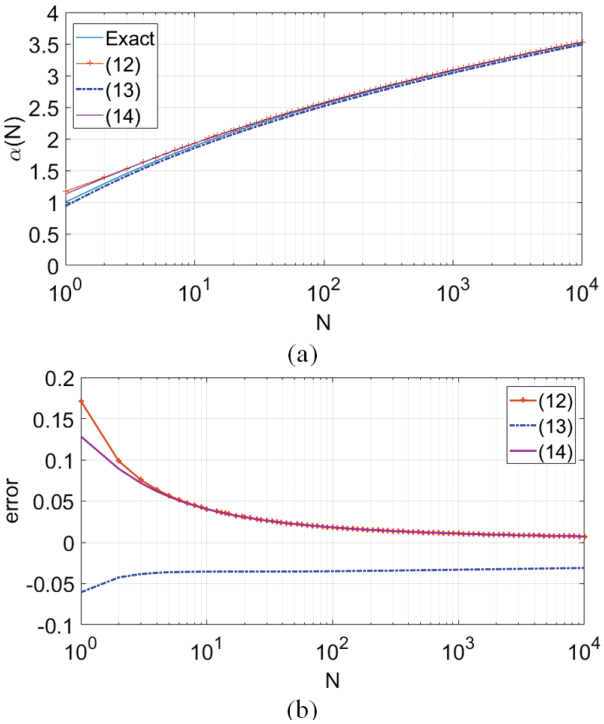

Fig. 4. (a) Plots of (4), (12)-(14) for different *N*, (b) error plot of (12)-(14), units are in linear.

of $\lceil |E_x|^2 \rceil_N$. From [2], we have:

$$\text{std}_{\text{rel}}(\lceil |E_x|^2 \rceil_N) = \frac{\text{std}(\lceil |E_x|^2 \rceil_N)}{\langle \lceil |E_x|^2 \rceil_N \rangle} = \frac{\sqrt{\sum_{k=1}^{N} \frac{1}{k^2}}}{\sum_{k=1}^{N} \frac{1}{k}}, \quad (16)$$

and we know that the uncertainty of power is 2 times the uncertainty of E-field (from $P \propto |E_x|^2$we have $dP/P \approx 2d|E_x|/|E_x|$) [5], thus the relative standard deviation of $\lceil |E_x| \rceil_N$ can be approximated as:

$$\text{std}_{\text{rel}}(\lceil |E_x| \rceil_N) \approx \frac{1}{2}\text{std}_{\text{rel}}\left(\lceil |E_x|^2 \rceil_N\right) \approx \frac{1}{2}\frac{\sqrt{\frac{\pi^2}{6} - \frac{1}{N}}}{\gamma + \psi_0(N+1)}$$

$$= \frac{1}{2}\frac{\sqrt{\frac{\pi^2}{6} - \frac{1}{N}}}{\gamma + \ln N + \frac{1}{2N} - \frac{1}{12N^2} + \ldots}, \quad (17)$$

$$\approx \frac{\pi}{2\sqrt{6}}\frac{1}{\gamma + \ln N}. \quad (18)$$

In [5], a similar expression is given with $\frac{1}{2}\frac{\sqrt{\frac{\pi^2}{6} - \frac{N+1}{N(N+2)}}}{0.5772 + \ln(N+1) - \frac{1}{2(N+1)}}$.

The plot of (15),(17) and (18) are illustrated in Fig. 5 (a), (15) is used as the reference values (the exact values), and the difference between (17), (18) and (15) are presented in Fig. 5 (b), respectively. It is interesting to note that the convergence speed of (18) is different from the mean value (by using the central limit theorem) which is $\frac{1}{\sqrt{N}}$ [5].

We can also link the parameters to the generalized extreme value distribution (GEV) [10]–[18] when $N \to \infty$. By applying [10]:

$$s = \frac{\sqrt{6}}{\pi}\text{std} = \frac{\sqrt{6}}{\pi}\text{std}_{\text{rel}}(\lceil |E_x| \rceil_N)\,\alpha(N), \quad (19)$$

$$m = \alpha(N) - \gamma s. \quad (20)$$

The approximated GEV CDF is:

$$G_{\text{GEV}}(x) = \exp\left[-\exp\left(-\frac{x-m}{s}\right)\right], \quad (21)$$

the PDF is:

$$p_{\text{GEV}}(x) = \frac{1}{s}\exp\left[\frac{m - x - s\exp(-\frac{x-m}{s})}{s}\right] \quad (22)$$

When $N \to \infty$, (19) and (20) can be approximated as:

$$s = \frac{\sqrt{6}}{\pi}\text{std} \approx \frac{1}{\sqrt{\pi}\sqrt{\gamma + \ln N + \frac{1}{2N}}}, \quad (23)$$

$$m \approx \sqrt{\frac{4}{\pi}\left(\gamma + \ln N + \frac{1}{2N}\right)} - \frac{\gamma}{\sqrt{\pi}\sqrt{\gamma + \ln N + \frac{1}{2N}}}. \quad (24)$$

The plot for the exact PDFs (1) and GEV PDFs (22) of the normalized maximum rectangular E-field are given in Fig. 6. As expected, when $N \to \infty$, two PDFs are close to each other.

For the PDF of the maximum-to-mean ratio of the received power $\lceil |E_x|^2 \rceil_N$, we have the same $p_{\text{GEV}}(x)$ when $N \to \infty$. The only difference is: the standard deviation and the expected value ($\alpha(N)$) in (19) and (20) are replaced by the values of $\sqrt{\sum_{k=1}^{N} k^{-2}}$ and $\sum_{k=1}^{N} k^{-1}$, respectively.

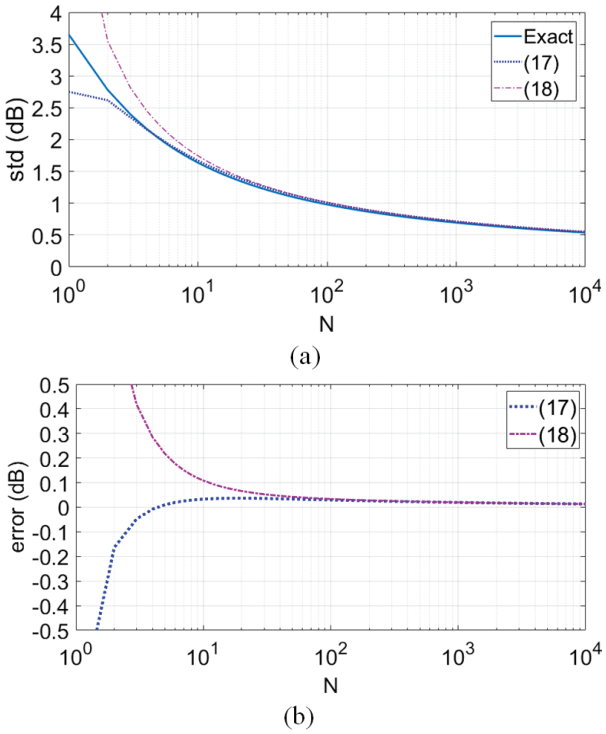

Fig. 5. (a) Plots of the approximated relative standard deviation in dB units ($20\log 10(1 + \text{std}_{\text{rel}})$), (b) error plot of (17), (18), units are in dB.

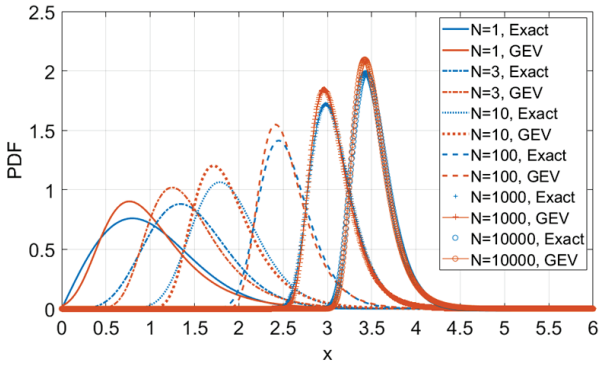

Fig. 6. Comparison plots of exact PDFs and GEV PDFs for different N.

Table 1: A summary of maximum-to-mean ratio expressions

Form	Expected value $\alpha(N)$	Relative standard deviation	where
Integral	$\frac{\int_0^\infty xp(x)dx}{\sqrt{\pi/2}}$	$\frac{\sqrt{\int_0^\infty x^2p(x)dx-\frac{\pi}{2}\alpha(N)^2}}{\alpha(N)\sqrt{\pi/2}}$	$p(x)=\frac{Nx}{\sigma^2}\left[1-\exp\left(\frac{-x^2}{2}\right)\right]^{N-1}\exp\left(\frac{-x^2}{2}\right)$
Series	$\sum_{k=0}^{N-1}\frac{N!\,(-1)^k}{(N-k-1)!\,(k+1)!\,\sqrt{k+1}}$	$\sqrt{\frac{4}{\pi}\frac{\sum_{k=1}^{N}\frac{1}{k}}{\alpha(N)^2}-1}$	
[4]	$\sqrt{\frac{4}{\pi}\ln\frac{1}{\left[1-0.5^{\frac{1}{N}}\right]}}$		
[5]	$\sqrt{\frac{4}{\pi}\left[0.5772+\ln(N+1)-\frac{1}{2(N+1)}\right]}$	$\frac{1}{2}\frac{\sqrt{\frac{\pi^2}{6}-\frac{N+1}{N(N+2)}}}{0.5772+\ln(N+1)-\frac{1}{2(N+1)}}$	
This paper	$\sqrt{\frac{4}{\pi}\left(\gamma+\ln N+\frac{1}{2N}-\frac{1}{12N^2}+\cdots\right)}$	$\frac{1}{2}\frac{\sqrt{\frac{\pi^2}{6}-\frac{1}{N}}}{\gamma+\ln N+\frac{1}{2N}-\frac{1}{12N^2}+\cdots}$	$\gamma\approx0.5772$, $\psi_0(x)$ is the digamma function

III. CONCLUSIONS

We have reviewed different analytical equations for the expected value and the standard deviation of the normalized maximum rectangular E-field in a well-stirred RC. Useful derivations are revisited and similar results are obtained. Numerical results show that: for small independent sample number *N*, we can calculate the results using the finite series directly; when $N > 5$, very good approximations can be obtained for both the expected value and the standard deviation. Table 1 summarizes the expressions in different forms. The approximated analytical expressions are also linked to the parameters of the GEV parameters when $N \to \infty$.

ACKNOWLEDGMENT

This work was supported in part by the Fund of Prospective Layout of Scientific Research for NUAA (Nanjing University of Aeronautics and Astronautics).

REFERENCES

[1] IEC 61000-4-21, Electromagnetic compatibility (EMC) – Part 4-21: Testing and measurement techniques – Reverberation chamber test methods, IEC Standard, Ed 2.0, 2011-01.

[2] J. Ladbury, G. Koepke, and D. Camell, Evaluation of the NASA Langley Research Center mode-stirred chamber facility, National Institute of Standards and Technology, Gaithersburg, MD, USA, Tech. Note 1508, Jan. 1999.

[3] T. H. Lehman and G. J. Freyer, "Characterization of the maximum test level in a reverberation chamber," *IEEE International Symposium on Electromagnetic Compatibility,* pp. 44-47, 1997.

[4] L. R. Arnuat and P. D. West, *Electric Field Probe Measurements in the NPL Untuned Stadium Reverberation Chamber*, NPL CETM13, Sep. 1999.

[5] L. R. Arnaut, *Measurement Uncertainty in Reverberation Chambers – I. Sample Statistics*, NPL Report TQE 2, Dec. 2008.

[6] Q. Xu and Y. Huang, *Anechoic and Reverberation Chambers: Theory, Design and Measurements*, Wiley-IEEE, 2019.

[7] D. A. Hill, *Electromagnetic Fields in Cavities: Deterministic and Statistical Theories*, Hoboken, NJ, USA, Wiley, 2009.

[8] E. W. Weisstein, Harmonic Series, From MathWorld – A Wolfram Web Resource. https://mathworld.wolfram.com/HarmonicSeries.Html

[9] T. N. Vu, A New Approximation Formula for Computing the N-th Harmonic Number (Update), from Series Math Study Resource. http://www.seriesmathstudy.com/sms/ApproximateFormulaHarmonicNum, 11/11/2011.

[10] G. Gradoni and L. R. Arnaut, "Generalized extreme-value distributions of power near a boundary inside electromagnetic reverberation chambers," *IEEE Transactions on Electromagnetic Compatibility,* vol. 52, no. 3, pp. 506-515, Aug. 2010.

[11] G. Orjubin, "Maximum field inside a reverberation chamber modeled by the generalized extreme value distribution," *IEEE Transactions on Electromagnetic Compatibility,* vol. 49, no. 1, pp. 104-113, Feb. 2007.

[12] C. E. Hager and J. D. Rison, "On applying the generalized extreme value distribution to undermoded

cavities within a reverberation chamber," *IEEE International Symposium on Electromagnetic Compatibility & Signal/Power Integrity (EMCSI),* pp. 681-686, 2017.

[13] N. Nourshamsi, J. C. West, and C. F. Bunting, "Effects of aperture dimension on maximum field level inside nested chambers by applying the generalized extreme value distribution," *IEEE Symposium on Electromagnetic Compatibility, Signal Integrity and Power Integrity (EMC, SI & PI),* pp. 628-633, 2018.

[14] N. Nourshamsi, J. C. West, and C. F. Bunting, "Investigation of electromagnetic complex cavities by applying the generalized extreme value distribution," *IEEE Symposium on Electromagnetic Compatibility, Signal Integrity and Power Integrity (EMC, SI & PI),* pp. 622-627, 2018.

[15] N. Nourshamsi, J. C. West, C. E. Hager, and C. F. Bunting, "Generalized extreme value distributions of fields in nested electromagnetic cavities," *IEEE Transactions on Electromagnetic Compatibility,* vol. 61, no. 4, pp. 1337-1344, Aug. 2019.

[16] P. Hu, Z. Zhou, X. Zhou, J. Li, J. Ji, M. Sheng, and P. Li, "Generalized extreme value distribution based framework for shielding effectiveness evaluation of undermoded enclosures," *International Symposium on Electromagnetic Compatibility - EMC EUROPE*, pp. 1-6, 2020.

[17] P. Hu, X. Zhou, and Z. Zhou, "On the modelling of maximum field distribution within reverberation chamber using the generalized extreme value theory," *IEEE MTT-S International Conference on Numerical Electromagnetic and Multiphysics Modeling and Optimization (NEMO),* pp. 1-4, 2020.

[18] P. Hu, Z. Zhou, X. Zhou, and M. Sheng, "Maximum field strength within reverberation chamber: A comparison study," *6th Global Electromagnetic Compatibility Conference (GEMCCON),* pp. 1-4, 2020.

Qian Xu (Member, IEEE) received the B.Eng. and M.Eng. degrees from the Department of Electronics and Information, Northwestern Polytechnical University, Xi'an, China, in 2007 and 2010, and received the PhD degree in electrical engineering from the University of Liverpool, U.K, in 2016. He is currently an Associate Professor at the College of Electronic and Information Engineering, Nanjing University of Aeronautics and Astronautics, China.

He was as a RF engineer in Nanjing, China in 2011, an Application Engineer at CST Company, Shanghai, China in 2012. His work at University of Liverpool was sponsored by Rainford EMC Systems Ltd. (now part of Microwave Vision Group) and Centre for Global Eco-Innovation. He has designed many chambers for the industry and has authored the book *Anechoic and Reverberation Chambers: Theory, Design, and Measurements* (Wiley-IEEE, 2019). His research interests include statistical electromagnetics, reverberation chamber, EMC and over-the-air testing.

Rui Jia received the B.Eng. degrees from the Department of Electronics and Information, Zhengzhou University, Zhengzhou, China, in 2008, and received the M.Eng. and Ph.D. degrees in electronic engineering from Mechanical Engineering College, Shijiazhuang, China, in 2010 and 2014, respectively. His research interests include statistical electromagnetics, reverberation chamber, and EMC.

Lifei Geng received the B.Eng., M.Eng. and Ph.D. degrees from the Department of Electronics and Information, Mechanical Engineering College, Shijiazhuang, China, in 2006, 2008 and 2013, respectively. His research interests include electromagnetic theory, reverberation chamber, and EMC.

Hao Guo received the B.Sc. and M.Sc. degrees from the Department of Physics, Dalian University of Technology, Dalian, China, in 2004, and 2009, respectively. His research interests include plasma, reverberation chamber, and EMC.

Yongjiu Zhao received the M.Eng. and Ph.D. degrees in electronic engineering from Xidian University, Xi'an, China, in 1990 and 1998, respectively. Since March 1990, he has been with the Department of Mechano-Electronic Engineering, Xidian University where he was a professor in 2004. From December 1999 to August 2000, he was a Research Associate with the Department of Electronic Engineering, The Chinese University of Hong Kong. His research interests include antenna design, microwave filter design and electromagnetic theory.

Tri-polarization Reconfigurable Fabry-Perot Resonator Antenna in Ku-band

Shichao Zhu, Jiagang He, Jie Yu, Yang Feng, Shaopeng Pan, and Gaosheng Li

College of Electrical and Information Engineering
Hunan University, Changsha 410082, China
zsc_08@163.com, 609288490@qq.com, antennayujie@hnu.edu.cn, fengyang@hnu.edu.cn, shaop1128@163.com, Gaosheng7070@vip.163.com

***Abstract* –** In this paper, a broadband tri-polarization reconfigurable antenna applied to polarization diversity is proposed. A partially reflective surface (PRS) is designed to form an air-filled resonator cavity. The reflection phase of the PRS has a positive phase gradient in order to achieve the characteristics of the proposed antenna gain enhancement in the wideband. A metal patch of a four-arm meander structure is used as the radiation structure and the feeding is realized through a four-channel rotating feeding network with equal amplitude and 90° phase difference. The feeding network is connected to the radiation structure through four metallized vias. In order to realize the polarization reconfigurability, the PIN diodes and the corresponding DC bias circuit are integrated in the rotating feeding network. The characteristics of horizontal polarization (HP), vertical polarization (VP) and right-hand circular polarization (RHCP) are realized by changing the ON/OFF states of PIN diodes integrated in the feeding network. In order to verify the performance of the proposed antenna, fabrication and testing were carried out. The measurement results show that the −10 dB impedance bandwidths of HP, VP, RHCP are 11% (12.5-14 GHz), 6.4% (13.7-14.6 GHz) and 20% (12.2-14.9 GHz), and the peak realized gains are 9.1, 9.2 and 11.5 dBi, respectively. For RHCP mode, the 3-dB axial ratio bandwidth reaches about 17% (12.35-13.4 GHz and 13.6-14.9 GHz).

***Index Terms* –** partially reflective surface (PRS), polarization diversity, rotating feeding network, tri-polarization reconfigurable, wideband antenna.

I. INTRODUCTION

Antenna with high gain and reconfigurable polarization plays an increasingly important role in some special scenarios such as mobile communication, and has been studied more and more deeply in recent years. An antenna that can be applied to polarization diversity can reduce the complexity of the system to a certain extent. For example, by controlling DC signal, the polarization states of the antenna can be flexibly and conveniently adjusted, which greatly reduces the attenuation loss, enhances the communication capacity of the system, and improves the rate of channel multiplexing [1–6]. At present, there are several mature methods of polarization reconfigurable antenna design, and the reconfigurable feeding network is one of the effective ways. In [7], a low-frequency quad-polarization reconfigurable antenna based on the feeding network is proposed. The mode is switched by controlling the state of the PIN diode. Since the feeding network does not have the characteristics of broadband, the bandwidth of the antenna is relatively narrow, which is not suitable for scenarios that require wide band. Polarization reconfiguration can also be achieved by loading the polarization conversion surface. For example, in [8], a reconfigurable polarization converter is proposed to realize the linear-circular polarization conversion, but the gain of the unit cell is relatively low.

For the high gain characteristics of antenna, it is generally realized by combining elements to form an array. However, for the array, on the one hand, the size of the array is usually large and cannot be realized in some small spaces. On the other hand, for most reconfigurable antennas, the array introduces a large amount of DC bias circuits. Although the gain can be improved, the system becomes very complex. In order to avoid the use of arrays to increase gain, Fabry-Perot (FP) resonant cavity antenna can be used, and high gain performance can be achieved by designing a reasonable feed source and PRS [9–13]. In [14], a FP antenna that uses linear polarization sources and PRS layer to achieve circular polarization is proposed. The improved PRS layer achieves gain increase and RCS reduction at the same time. Linearly polarized waves are converted into circularly polarized waves after passing through the PRS layer, but the reconfiguration of polarization is not realized. At present, most polarized reconfigurable antennas operate in low frequency bands, and there are few broadband and linear-circular polarization reconfigurable antennas that operate in high frequency bands, such as Ku-band. In [15], a linear polarization reconfigurable antenna based on the

Submitted On: February 3, 2022
Accepted On: September 3, 2022

https://doi.org/10.13052/2022.ACES.J.370803

reconfigurable feeding network is proposed. It adopts a double feed and a positive phase gradient PRS to achieve high gain performance. Compared with a single feed, double-feed can indeed further improve the antenna gain.

In this paper, a wideband tri-polarization reconfigurable FP resonator antenna operating in Ku-band is proposed. The feeding antenna is composed of a meandering bend line structure and a rotating feeding network [16]. Four PIN diodes and DC bias circuit are integrated in the feeding network for switching HP, VP and RHCP states. The PRS layer is located above the feeding antenna and forms the resonant cavity. The PRS layer can improve the antenna gain only when the reflection phase is positive gradient (reflection phase increase with frequency) and the reflection coefficient is relatively high. The PRS proposed in this paper can satisfy the above two conditions well in the whole operating frequency range. Simulation and measurement results show that the proposed antenna has high-gain wideband and polarization reconfigurable characteristics.

This paper is organized as follows: Section II mainly introduces the operation mechanism of the proposed PRS's unit cell, rotating feeding network and feed antenna. Section III gives the simulation and measurement results of the proposed antenna, and has been analyzed and discussed. The last section is a brief summary.

II. POLARIZATION RECONFIGURABLE FP ANTENNA

Figure 1 shows the overall structure of the proposed tri-polarization reconfigurable antenna with broadband and gain enhancement. The proposed antenna consists of the following parts: feeding network, metal ground, radiation patch and PRS layer. The distance H between the PRS layer and the metal ground of the antenna is about 10mm. A PRS array is composed of 11×12 periodic units as the PRS layer to increase the antenna gain. The PRS layer and the feeding antenna are connected by four M2 nylon bolts, so the overall size of the proposed antenna is 45mm×50mm×10mm (2.1λ×2.3λ×0.46λ at 14 GHz). The radiation part is composed of a four-arm meandering line structure. Its four arms are connected to a rotating feeding network at the bottom. The PIN diodes are integrated on the rotating feeding network, and the radiation mode can be changed by controlling the state of the PIN diodes.

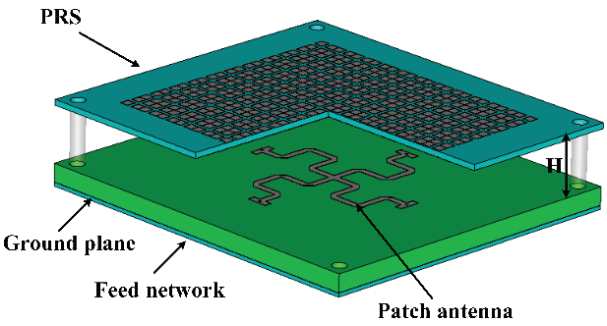

Fig. 1. Structure of tri-polarization reconfigurable antenna.

A. Design of PRS

The PRS has high reflection characteristics and can be regarded as a reflective surface, which can be loaded on top of the antenna as a cladding to form a Fabry-Perot resonant cavity, and the antenna ground serves as the lower reflective surface. In the resonant state, the electromagnetic wave generated by the feed is reflected in the cavity for many times, and the same phase is superimposed on the PRS, thereby realizing the characteristics of high-gain unidirectional radiation. However, the PRS needs to meet the following conditions to achieve broadband gain improvement:

$$\varphi_{PRS} + \varphi - \frac{4\pi}{\lambda} H = 2n\pi, n = 0, 1, 2..., \qquad (1)$$

where φ_{PRS} and φ represent the reflection phase of PRS and metal floor respectively. H is the distance between them, and λ is the operating wavelength of the antenna. It can be seen from (1) that the reflective phase of the PRS needs to be positively correlated with the frequency. That is to say, in order to realize the high-gain FP antenna operating in broadband, the reflective phase of the PRS should increase linearly with the increase of frequency while maintaining the high reflective coefficient of the PRS.

The PRS designed in this paper can well satisfy the resonant condition. The proposed PRS is composed of metal patches with etched square ring and cross groove as shown in Fig. 2 (a). The structure is printed on F4B dielectric material with a thickness of 0.933mm, dielectric constant of 3.0, and loss tangent (tan δ) of 0.001. The dimensions of the proposed PRS unit operating in the Ku-band as follows: P =3.14mm, a=1.7mm, w = 0.63mm, d = 0.66mm. In order to better explain the proposed PRS based on positive phase gradient, the single-sided cross groove and single-sided square ring structures are simulated respectively. It can be seen from Fig. 2 (b) that the reflection coefficient of the square ring structure decreases with the increase of frequency, that is, it reflects low frequency electromagnetic waves and transmits high frequency electromagnetic waves. On the contrary, the reflection coefficient of the single-sided cross groove structure increases with the increase of frequency, so it reflects high frequency electromagnetic waves and transmits low frequency electromagnetic waves. Therefore, the combination of the single-sided square ring structure and cross groove structure can achieve partial reflection characteristics. The

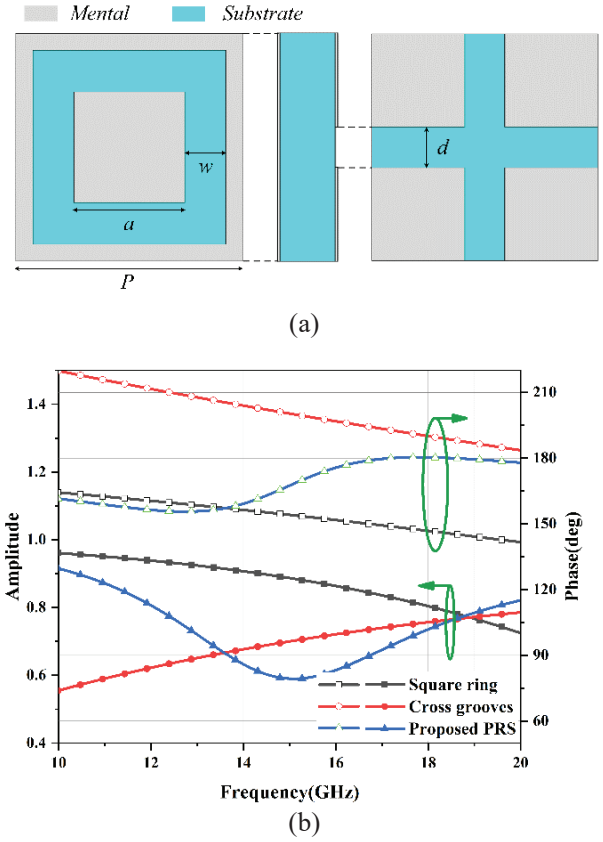

Fig. 2. (a) Structure of the proposed PRS unit. (b) Reflection amplitude and phase comparison of the proposed PRS unit and the single-sided structure.

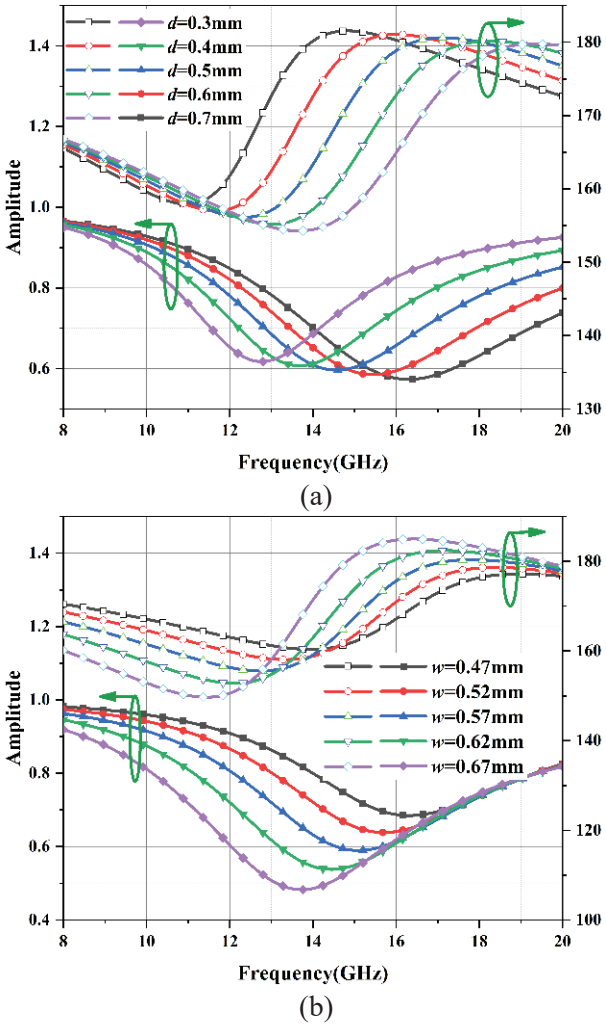

Fig. 3. Influence of unit size (a) parameter *d*, (b) parameter *w* on reflection characteristics.

reflection phase is positively correlated with frequency while achieving the high reflection coefficient.

In order to further understand the reflection characteristics of the unit, the effects of parameters *w* and *d* on the unit are investigated, as shown in Fig. 3. The center frequency of unit resonance shifts to high frequency with the increase of parameter *d*, which can be attributed to the decrease of capacitance between metal patches. In addition, with the increase of *w*, the reflection amplitude of PRS unit decreases and the reflection phase slope increases. Therefore, the resonant frequency can be adjusted without changing the structural period by adjusting parameter *d*, and the ideal wideband reflection phase curve positively correlated with frequency can be obtained by adjusting parameter *w*.

B. Feeding Network and Radiation Structure

Figure 4 show the structure of the tri-polarization reconfigurable feeding antenna. Figure 4 (a) shows the meandering curve structure etched on the front of F4BM with a thickness of 2.44mm, dielectric constant of 2.2, and loss tangent (tan δ) of 0.0015. The metal ground is printed on the back of the F4BM. In order to realize the circular polarization of the antenna, it is necessary to design a four-channel output rotating feeding network with equal amplitude and 90° phase difference. Figure 4 (b) shows that the feeding network is printed on Rogers 3003 dielectric material with thickness of 0.508mm, dielectric constant of 3.0 and loss tangent (tan δ) of 0.001. The rotating feeding network is mainly designed based on the idea of cascading power dividers and phase shifters. By designing power divider, inverter and 90° phase shifter, the four output ports can achieve the characteristics of equal signal amplitude and 90° phase difference.

Figure 4 (b) shows the detailed parameters of the feeding network. Since the proposed antenna needs to operate in broadband, it is necessary to design a broadband feeding network. There are two main reasons why the feeding network can operate in broadband. First, the two-stage Wilkinson power divider is different from the

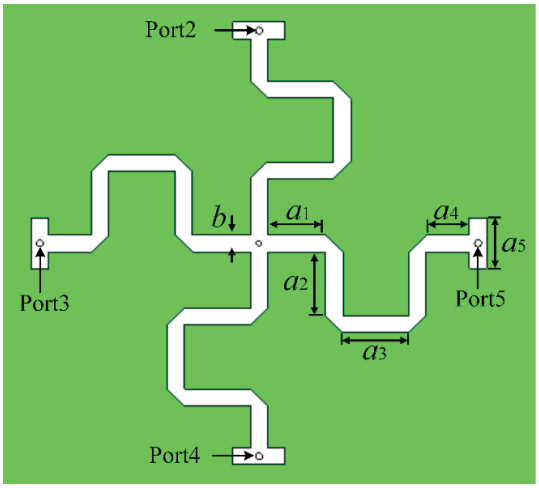

(a)

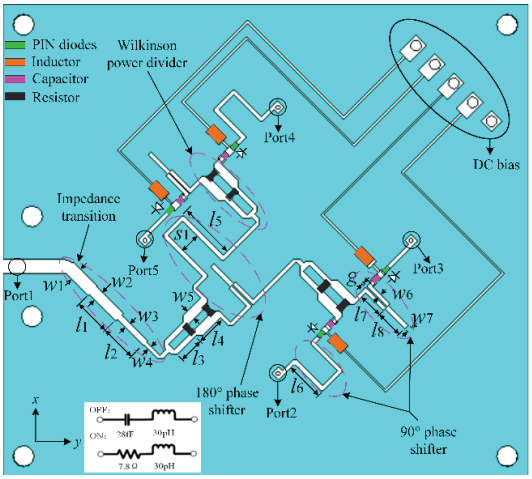

(b)

Fig. 4. Structure of the proposed antenna. (a) Radiation structure of meandering curves. (b) Configurations of the feeding network and equivalent circuit of the PIN diode. The dimensions of the feeding network are given as follows (unit: mm): a_1=3.35, a_2=3.8, a_3=3.8, a_4=2.5, a_5=3, b=3.8, l_1=3.53, l_2=3.53, l_3=2.39, l_4=2.87, l_5=5.26, l_6=3.56, l_7=2.4, l_8=2.65, w_1=1.28, w_2=1, w_3=0.58, w_4=0.4, w_5=0.94, w_6=0.36, w_7=0.41, S_1=2, g=0.12.

traditional Wilkinson power divider. The power divider in this paper belongs to the dual-band coupled-line divider and there are two resonant points to achieve the broadband. Second, the 90° and 180° phase shifters consist of weak coupled line and short-circuited line, which can also operate in broadband. The working mechanism of Wilkinson power divider and phase shifter can be explained by the odd- and even- mode theory [17–18].

Table 1: Polarization by different states of PIN diodes

Polarization	PIN1	PIN2	PIN3	PIN4
HP	ON	OFF	ON	OFF
VP	OFF	ON	OFF	ON
RHCP	ON	ON	ON	ON

In order to obtain the reconfigurable polarization of the antenna, some lumped elements are integrated on the feeding network, and the polarization state of radiation wave can be changed by controlling the ON/OFF states of four PIN diodes (MACOM MADP-000907-14020). The forward bias state of PIN diode can be equivalent to the series of resistor and inductor, and the reverse bias state can be equivalent to the series of capacitor and inductor, as shown in Fig. 4 (b). Through changing the states of PIN diodes, it is possible to control whether the four-arms of the antenna operate or not. When PIN1 and PIN3 are forward biased and PIN2 and PIN4 are reverse biased, the proposed antenna works in horizontal polarization state. When PIN1 and PIN3 are reverse biased and PIN2 and PIN4 are forward biased, the proposed antenna operates in vertical polarization state. If all PIN diodes are forward biased, the proposed antenna operates in a circularly polarized state.

The ON/OFF states of PIN diodes need to be controlled by a DC voltage, so the DC bias circuit is designed in the feeding network. The DC bias line and the microstrip feed-line are connected by the high-frequency inductance, which not only realizes the control of the PIN diodes, but also achieves the purpose of isolating the RF signal and the DC signal. The DC signal forms a loop through the ground via in the center of the radiating structure. The function of the capacitors is mainly to avoid the influence of DC voltage on the RF signal and to enhance the isolation of AC/DC. The absorption resistances used on the Wilkinson power divider are 91Ω and 300Ω, respectively.

Since the performance of the proposed antenna depends on the performance of the feeding network, a full-wave electromagnetic simulation analysis of the rotating feeding network is performed separately. Figure 5 shows the S-parameters and phase difference curves of each port of the proposed rotating feeding network. It can be observed that the amplitudes of the four output ports are roughly equal and the phase difference is about 90°. The simulation results show that the performance of the feeding network can meet the requirements of the circular polarization antenna.

III. SIMULATION AND MEASUREMENT PERFORMANCE

In order to verify whether the simulation results of the tri-polarization reconfigurable FP antenna are

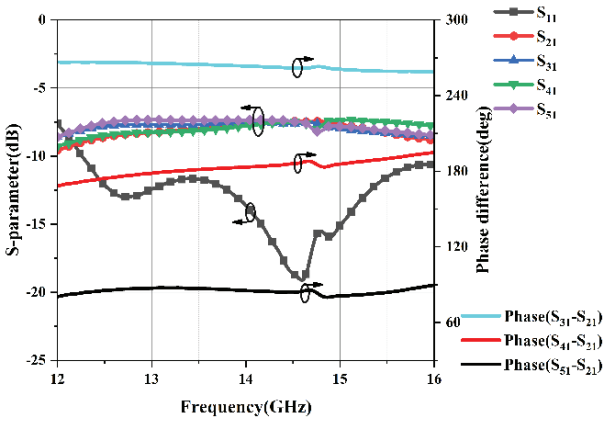

Fig. 5. Simulated results of rotating feeding network.

consistent with the actual measurement results, a the PRS layer and feeding antenna are fabricated based on the above structural parameters. Figure 6 shows the produced antenna prototype and the test environment in an anechoic chamber. The S-parameter, realized gain and axial ratio of the prototype antenna were measured in the anechoic chamber.

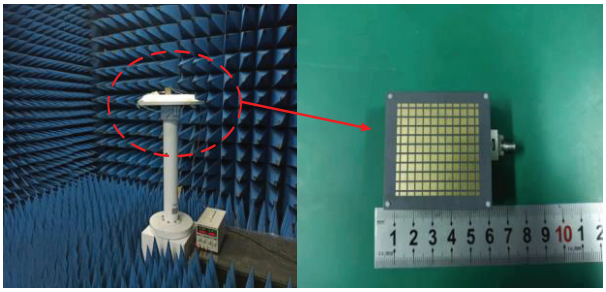

Fig. 6. Photograph of the proposed antenna and test environment.

The reflection coefficient, axial ratio, realized gain and radiation pattern of the proposed antenna were measured [19]. Figure 7 shows the simulated and measured S-parameter, realized gain and axial ratio of the RHCP for the proposed antenna. Figure 7 (a) shows that the simulated and measured -10 dB impedance bandwidth is about 11% (12.5-14 GHz) and the peak realized gain is about 9.1 dBi for HP state. The measured S-parameter and realized gain of VP are depicted in Fig. 7 (b). It is observed that the measured impedance BW of S11<-10 dBf is about 6.4% (13.7-14.6 GHz) and the peak realized gain is about 9.2 dBi. The reflection coefficient and realized gain of RHCP state are presented in Fig. 7 (c), and it can be observed that the measured impedance BW of S11< -10 dB is about 20% (12.2-14.9 GHz) and the peak realized gain is about 11.5 dBic. Figure 7 (d) describes the AR performance of the RHCP state. It can be found that the 3dB AR bandwidth is about 17% (12.35-13.4 GHz and 13.6-14.9 GHz).

The results show that the measured reflection coefficient of the proposed antenna is basically consistent with the simulation results. The gain and AR performance of measurement and simulation are different to some extent. The main reason for this difference may be that the equivalent circuit of the PIN diode is different from the actual parameters, which causes more loss. In addition, errors generated during antenna fabricating and testing are also included.

Simulated and measured normalized radiation patterns are compared at 12.7, 14 and 14.4 GHz for the HP, VP and RHCP modes shown in Figs. 8, 9 and 10, respectively. It is observed from Figs. 8 and 9 that for linearly polarized waves, similar pencil-beam patterns can be obtained on both sides. Due to the meandering curve structure, the instability of lumped elements integrated in the feeding network and the coupling between microstrip lines, the cross-polarization performance under HP and VP is worse than that of the RHCP. Overall, the radiation patterns of the proposed antenna remain relatively stable in the operating frequency band.

Due to the limitation of the measurement system, the 3D far-field radiation pattern of the antenna prototype cannot be obtained to calculate its directivity. Here, the measured efficiency is obtained by the ratio of the measured gain to the simulated directivity [20], as shown in Fig. 11. The efficiency of the antenna is more than 60% in the three polarization states. The loss of antenna is mainly due to DC bias circuit, PIN diodes and poor match. The loss is studied by replacing the PIN diode with metal strip and removing the DC bias circuit. Investigation shows that the loss of DC bias circuit is about 1.5 dB and the loss of the PIN diodes is about 0.3 dB. Other losses are due to poor match. Therefore, the efficiency of the antenna can be further improved by optimizing the DC bias circuit.

Table 2 presents a comparison among the proposed antenna and the reported reconfigurable antenna. It can be noted that the proposed antenna shows the advantages in high gain and wide BW.

IV. CONCLUSION

In this paper, gain enhancement for wideband tri-polarization reconfigurable FP antenna is realized by loading a metallic PRS layer. The designed single-layer PRS achieves a good performance with a positive gradient of the reflection phase in broadband, and can well improve the gain of the proposed antenna. Three polarization states, including HP, VP and RHCP states, have been realized using four PIN diodes integrated into the feeding network. The measured results have confirmed that the antenna is able to achieve −10 dB bandwidth

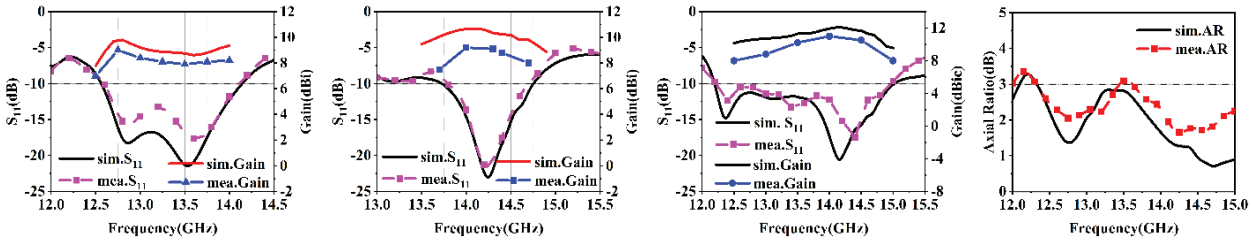

Fig. 7. Simulated and measured performance of the proposed antenna. (a) Reflection coefficients and gain under HP. (b) Reflection coefficients and gain under VP. (c) Reflection coefficients and gain under RHCP. (d) AR under RHCP.

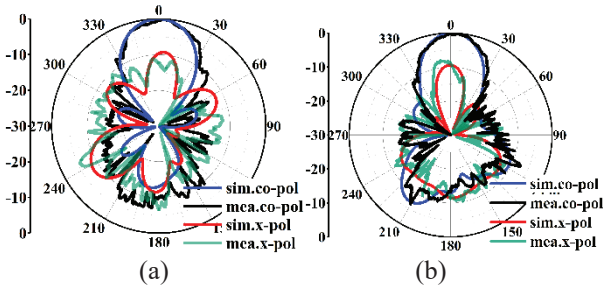

Fig. 8. Simulated and measured normalized radiation patterns of HP at 12.7 GHz. (a) H-plane. (b) E-plane.

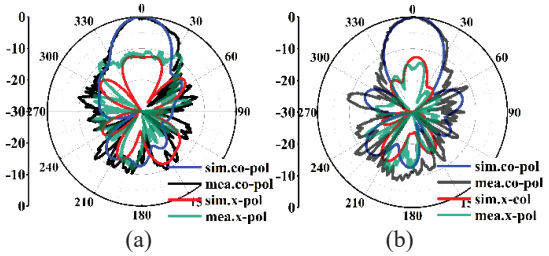

Fig. 9. Simulated and measured normalized radiation patterns of VP at 14 GHz. (a) H-plane. (b) E-plane.

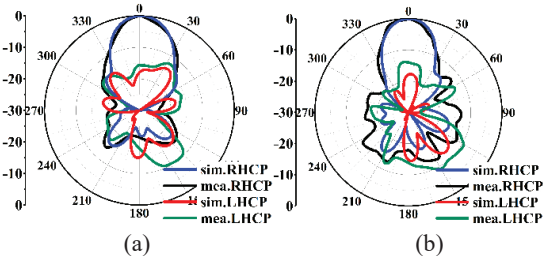

Fig. 10. Simulated and measured normalized radiation patterns of RHCP at 14.4 GHz. (a) H-plane. (b) E-plane.

of 11%, 6.4% and 20% for HP, VP and RHCP, and the peak realized gain achieved 9.1, 9.2 and 11.5 dBi, respectively. For RHCP mode, the 3 dB axial ratio bandwidth of about 17% is achieved. The simulation and measurement results show that the radiation patterns of E-plane and

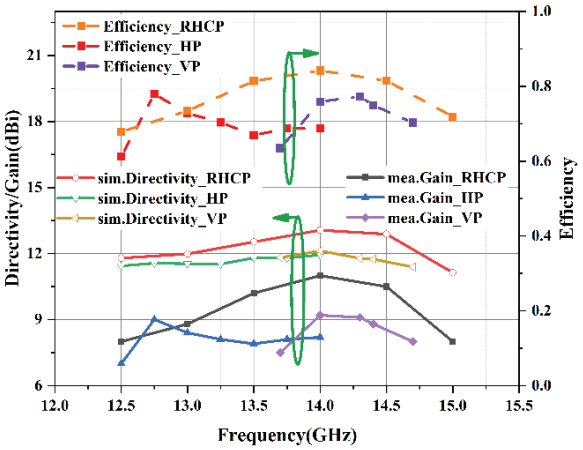

Fig. 11. Measured efficiency of the proposed antenna.

Table 2: Performance comparison with previously reported polarization reconfigurable antennas

Ref.	[4]	[6]	[13]	This work
Freq. (GHz)	2.4	5	7.4	14
Size (λ)	-	1.8×1.8 ×0.5	2×2×0.6	2.1×2.3 ×0.46
Polarization	3	3	3	3
Feeding network	No	Yes	Yes	Yes
AR BW(%)	7.9	13.1	4	17
No. of switches	4	8	2	4
Gain(dBi)	∼9	11.2	15.1	11.5

H-plane in the tri-polarization states of the antenna are similar and symmetrical, with good directivity. In addition, the DC bias circuit that controls the state of the PIN diodes can be easily integrated into the rotating feeding network. The proposed antenna is suitable for polarization diversity applications.

REFERENCES

[1] J. Row and Y. Wei, "Wideband reconfigurable crossed-dipole antenna with quad-polarization diversity," *IEEE Transactions on Antennas and Propagation*, vol. 66, no. 4, pp. 2090-2094, 2018.

[2] H. Sun and Z. Pan, "Design of a quad-polarization-agile antenna using a switchable impedance converter," *IEEE Antennas and Wireless Propagation Letters*, vol. 18, no. 2, pp. 269-273, 2019.

[3] K. M. Mak, H. W. Lai, K. M. Luk, and K. L. Ho, "Polarization reconfigurable circular patch antenna with a C-shaped," *IEEE Transactions on Antennas and Propagation*, vol. 65, no. 3, pp. 1388-1392, 2017.

[4] F. Wu and K. M. Luk, "Wideband tri-polarization reconfigurable magneto-electric dipole antenna," *IEEE Transactions on Antennas and Propagation*, vol. 65, no. 4, pp. 1633-1641, 2017.

[5] H. H. Tran, N. Nguyen-Trong, T. T. Le, and H. C. Park, "Wideband and multipolarization reconfigurable crossed bowtie dipole antenna," *IEEE Transactions on Antennas and Propagation*, vol. 65, no. 12, pp. 6968-6975, 2017.

[6] L. Ji, P. Qin, Y. J. Guo, C. Ding, G. Fu, and S. Gong, "A wideband polarization reconfigurable antenna with partially reflective surface," *IEEE Transactions on Antennas and Propagation*, vol. 64, no. 10, pp. 4534-4538, 2016.

[7] J. Hu, Z. Hao, and W. Hong, "Design of a wideband quad-polarization reconfigurable patch antenna array using a stacked structure," *IEEE Transactions on Antennas and Propagation*, vol. 65, no. 6, pp. 3014-3023, 2017.

[8] J. A. Ganie and K. Saurav, "High gain polarization reconfigurable antenna arrays using a polarization reconfigurable converter," *International Journal of RF and Microwave Computer-Aided Engineering*, p. e22765, 2021.

[9] P. Qin, L. Ji, S. Chen, and Y. J. Guo, "Dual-polarized wideband fabry–perot antenna with quad-layer partially reflective surface," *IEEE Antennas and Wireless Propagation Letters*, vol. 17, no. 4, pp. 551-554, 2018.

[10] W. Li, S. Gao, Y. Cai, Q. Luo, M. Sobhy, G. Wei, J. Xu, J. Li, C. Wu, and Z. Cheng, "Polarization-reconfigurable circularly polarized planar antenna using switchable polarizer," *IEEE Transactions on Antennas and Propagation*, vol. 65, no. 9, pp. 4470-4477, 2017.

[11] M. A. Meriche, H. Attia, A. Messai, S. S. I. Mitu, and T. A. Denidni, "Directive wideband cavity antenna with single-layer meta-superstrate," *IEEE Antennas and Wireless Propagation Letters*, vol. 18, no. 9, pp. 1771-1774, 2019.

[12] W. Cao, X. Lv, Q. Wang, Y. Zhao, and X. Yang, "Wideband circularly polarized fabry–perot resonator antenna in Ku-band," *IEEE Antennas and Wireless Propagation Letters*, vol. 18, no. 4, pp. 586-590, 2019.

[13] H. H. Tran and H. C. Park, "A simple design of polarization reconfigurable fabry-perot resonator antenna," *IEEE Access*, vol. 8, pp. 91837-91842, 2020.

[14] J. Ren, W. Jiang, K. Zhang, and S. Gong, "A high-gain circularly polarized fabry–perot antenna with wideband low-RCS property," *IEEE Antennas and Wireless Propagation Letters*, vol. 17, no. 5, pp. 853-856, 2018.

[15] R. Lian, Z. Tang, and Y. Yin, "Design of a broadband polarization-reconfigurable fabry–perot resonator antenna," *IEEE Antennas and Wireless Propagation Letters*, vol. 17, no. 1, pp. 122-125, 2018.

[16] K. Gao, X. Ding, L. Gu, Y. Zhao, and Z. Nie, "A broadband dual circularly polarized shared-aperture antenna array using characteristic mode analysis for 5G applications," *International Journal of RF and Microwave Computer-Aided Engineering*, vol. 31, no. 3, p. e22539, 2021.

[17] Q. Liu, H. Liu, and Y. Liu, "Compact ultra-wideband 90° phase shifter using short-circuited stub and weak coupled line," *Electronics Letters*, vol. 50, no. 20, pp. 1454-1456, 2014.

[18] Y. Wu, Y. Liu, and Q. Xue, "An analytical approach for a novel coupled-line dual-band Wilkinson power divider," *IEEE Transactions on Microwave Theory and Techniques*, vol. 59, no. 2, pp. 286-294, 2011.

[19] B. Y. Toh, R. Cahill, and V. F. Fusco, "Understanding and measuring circular polarization," *IEEE Transactions on Education*, vol. 46, no. 3, pp. 313-318, 2003.

[20] J. Hu and Z. C. Hao, "A compact polarization-reconfigurable and 2-D beam-switchable antenna using the spatial phase shift technique," *IEEE Transactions on Antennas and Propagation*, vol. 66, no. 10, pp. 4986-4995, 2018.

Shichao Zhu received the Bachelor degree in School of Electrical and Automation Engineering from East China Jiaotong University, Nanchang, China in 2020. He is currently pursuing the Master degree in the College of Electrical and Information Engineering, Hunan University, Changsha China, under the supervision of Prof. G.S. Li. His research interests include reconfigurable antennas, electromagnetic metamaterials and their antenna applications.

Jiagang He was born in Xiangtan, Hunan province, China, in 1997. He received the Bachelor degree in College of electronic science and technology from Hunan University of Technology, Zhuzhou, China, in 2019. He is now studying for postgraduate in the College of electronic science and technology, Hunan University. His research interests is terminal antenna and EMC.

Jie Yu was born in Xinyang, Henan province, China, in 1998. He received the Bachelor degree in optoelectronic information science and engineering from Changsha University of Science and Technology, Changsha, China, in 2019. He is currently working as postgraduate in Hunan University. His research interest is the liquid antennas.

Yang Feng was born in Yongzhou, Hunan province, China, in 1997. He received the Bachelor degree in Communication Engineering from Beijing Union University, Beijing, China, in 2019. He received the Master degree in Electronics and Communication Engineering from Hunan University, Changsha, China, in 2022. His research interests are in antenna theory and technology, including implantable antenna technology, antenna miniaturization technology.

Shaopeng Pan received the Bachelor degree in School of Physics and Electronic Science, Hunan University of Science and Technology (HNUST), Xiangtan, China, in 2019. He received the Master degree in Electronic Science and Technology form Hunan University (HNU), Changsha, China in 2022. His research interests include holographic antenna technology, electromagnetic metamaterials and programmable metamaterial antenna.

Gaosheng Li received his B.S. degree in electromagnetic field and microwave and his M.S. degree as well as his PH. D. in electronic science and technology from the National University of Defense Technology (NUDT), Changsha, China, in 2002, 2004 and 2013, respectively. He was with NUDT as a Teaching Assistant from 2004 to 2006, a Lecturer from 2006 to 2011, and then as an Associate Professor from 2011 to 2017. He joined Hunan University as a Professor in 2018. From 2014 to 2016, he was with Nanjing University of Aeronautics and Astronautics (NUAA) and Wuxi Huace Electronic Systems Co., Ltd., China as a Postdoctoral Research Fellow. From 2016 to 2017, he was a Visiting Scholar at the University of Liverpool (UoL), United Kingdom, sponsored by China Scholarship Council (CSC). His research interests include Antennas and Propagation (AP), Electromagnetic Compatibility (EMC), Wireless Propagation and Microwave Systems. Prof. Li is the author or co-author of 8 books and 170 papers published in journals and conference proceedings. He owns 3 international patents, 45 Chinese patents and 14 software copyrights. He won 3 national scientific prizes in 2008, 2013 and 2015, respectively. He is now a Senior Member of IEEE (2019), a Member of ACES (2017) and IEICE (2011), a Senior Member of Chinese Institute of Electronics (CIE, 2014), China Institute of Communications (CIC, 2017) and China Instrument and Control Society (CIS, 2020).

Bayesian Optimization Based on Student's T Process for Microstrip Antenna Design

Qing Li[1], Fei Meng[2], Yubo Tian[3], and Xiaoyan Wang[4]

[1]Ocean College
Jiangsu University of Science and Technology, Zhenjiang 212003, China
leo199808@163.com

[2]School of Information and Communication Engineering
Guangzhou Maritime University, Guangzhou 510725, China
mengfei@gzmtu.edu.cn

[3]School of Information and Communication Engineering
Guangzhou Maritime University, Guangzhou 510725, China
tianyubo@just.edu.cn
Corresponding to Yubo Tian, Qing Li, and Fei Meng are co-first authors.

[4]Ocean College
Jiangsu University of Science and Technology, Zhenjiang 212003, China
1836351293@qq.com

***Abstract* –** Bayesian Optimization (BO) is an efficient global optimization algorithm, which is widely used in the field of engineering design. The probabilistic surrogate model and acquisition function are the two keys to the algorithm. Building an efficient probabilistic surrogate model and designing a collection function with excellent exploring capabilities can improve the performance of BO algorithm, allowing it to find the optimal value of the objective function with fewer iterations. Due to the characteristics of small samples and non-parametric derivation of the Gaussian Process (GP), traditional BO algorithms usually use the GP as a surrogate model. Compared with the GP, the Student's T Process (STP) retains the excellent properties of GP, and has more flexible posterior variance and stronger robustness. In this paper, STP is used as the surrogate model in BO algorithm, the hyperparameters of the model are optimized by STP, and the estimation strategy function (EST) is improved based on the posterior output of the optimized STP, thus realizing the improved BO algorithm based on the STP. To verify the performance of the proposed algorithm, numerical experiments are designed to compare the performances of the traditional BO algorithm, which includes the lower confidence bound function (LCB) and EST as acquisition function respectively and GP as the surrogate model, and the proposed BO algorithm with STP as the surrogate model and LCB, expected improvement function (EI), expected regret minimization function (ERM) as acquisition function respectively. The results show that the proposed algorithm in this paper performs well when finding the global minimum of multimodal functions. Based on the developed algorithm in this paper, the resonant frequency of printed dipole antenna and E-shaped antenna is modeled and optimized, which further confirms the good design ability and design accuracy of the BO algorithm proposed in this paper.

***Index Terms* –** acquisition function; antenna optimization; Bayesian optimization; Gaussian process; Student's T process

I. INTRODUCTION

Constructing efficient global optimization algorithms has always been the focus of research topic. As an advanced and efficient global optimization algorithm, the Bayesian optimization (BO) algorithm has received extensive attention and research [1]. The BO algorithm is a kind of acquisition function and surrogate model as its cores to fit the objective function, collecting new sample observations to achieve fast iteration and find the maximum or minimum value of the objective function [2].

In recent years, the research on the BO algorithm is inseparable from three aspects: the establishment of a new surrogate model [3], the optimization of the surrogate model [4], and the design of the acquisition function [5]. The performance of BO algorithms can be improved by constructing efficient surrogate models, such as ran-

Submitted On: April 18, 2022
Accepted On: September 3, 2022

https://doi.org/10.13052/2022.ACES.J.370804

dom forests surrogate models [6], making multiple decision trees to improve computational efficiency and accuracy, and deep neural network surrogate models [7] to improve the model's ability to handle large-scale data. In recent years, the optimization of surrogate models in BO algorithms has also become a research hotspot. Chowdhury [8] proposed a scheme to dynamically adjust the domain boundary of the surrogate model to solve the complex problem of high-dimensional data analysis. Yenicelik [4]designed an algorithm named BORING to deal with the dimensionality reduction of data. The acquisition function in parallel BO can collect multiple sample points simultaneously to improve its efficiency. Ginsburg et al. [9] studied Monte Carlo to simulate the acquisition function to generate multiple sample points at a time. Some scholars [10] also use the multimodal method to solve multiple candidate sample points, reducing the time-consuming problem of the simulation.

As a classical surrogate model in BO, Gaussian Process (GP) has a rigorous mathematical theoretical foundation and can deal with complex problems [11, 12]. However, GP has two apparent shortcomings. Its posterior variance depends on the observed sample points, and its outliers are based on a prior assumption, which makes GP not very good at rejecting outlier ability. Student's T Process (STP) is a generalization of the GP, which obeys the Student's T distribution rather than the Gaussian distribution [13]. The study of STP makes up for the lack of robustness of GP, and it has a more flexible posterior variance. Shah [14] proposed to perform the inverse Wishart process on the kernel function of the GP to realize the STP and use it to deal with outliers in the data. This is because the kurtosis of the Student's T distribution is higher than that of the Gaussian distribution, which means it can contain outliers. More likely.

Särkkä [15] uses an STP instead of a GP and incorporates the noise term into the kernel function to simplify the computation. Tang et al. [16] proposed that when the input has noise that depends on the Student's T distribution, if the kernel function does not have the β property, the STP has a better ability to handle abnormal data. Chen et al. [17] proposed a multi-output GP and a multi-output STP, which solved the multi-output problem under the matrix variable of the STP. An effective way of improving the prediction accuracy and enhancing the performance of the model is to optimize the model's hyperparameters. For example, the gradient descent method [18], particle swarm optimization algorithm [19], and ant colony algorithm [20] are used to optimize the super parameters of the nonparametric model, so as to improve the performance of the model.

Scholars have also studied the combination of STP and BO algorithm. In 2013, Shah [21] implemented the Bayesian algorithm using STP and the expected improvement function, and compared it with the Bayesian algorithm using the GP as a surrogate model for the function optimization problem. In 2018, Tracey [22] implemented the Bayesian algorithm combining the STP and the expected improvement function, and applied it to the design of aerodynamic structures. In 2020, Clare [23] used the improved expected regret minimization function and confidence bound minimization function, respectively, to combine with STP to form a new Bayesian algorithm, enhancing the ability of BO.

As we all know, the optimization of electromagnetic devices through full-wave electromagnetic simulation software requires enormous computing resources, which is very time-consuming. Therefore, exploiting optimizing algorithms to design electromagnetic devices quickly is a good solution [24]. Gao [25] proposed a semi-supervised algorithm for antenna design, but this algorithm requires an additional round of antenna size. Torun [26] designed a two-stage BO algorithm and applied it to the minimization optimization of integrated circuits, and the surrogate model used in this algorithm is the GP model.

In this paper, a BO algorithm is proposed, which uses the combination of an improved maximum evaluation policy function [27] and a hyperparameter-optimized STP. Moreover, it is applied to optimize multimodal functions, printed dipole antenna, and E-shaped antenna. The results show that the proposed BO algorithm has better exploration and global optimization abilities than the traditional BO algorithm.

The rest of the paper is organized as follows. The second part briefly reviews the derivation of GP and STP. The third part cover the proposed BO algorithm, including the hyperparameters for the STP, optimization and improvement of the maximum evaluation policy function. The fourth part is the numerical experiment, which verifies the performance of the proposed algorithm. The fifth part is the application of the proposed algorithm to two microstrip antennas, including printed dipole antenna and E-shaped antenna. The subsequent parts is the summary and outlook.

II. BACKGROUND

A. Gaussian process

Gaussian Process (GP), as a non-parametric model being suitable for small sample, has strict mathematical theoretical derivation. Generally, we use (1) to describe the GP [28, 29]:

$$f(x) \sim GP(\mu(x), k(x,x)), \tag{1}$$

where the $\mu(x)$ is the mean function and the $k(x,x')$ is the covariance function. If $D_{1:n} = \{\{x_1,y_1\},\{x_2,y_2\},\ldots,\{x_n,y_n\}\}$ represents the observed

set, then the covariance matrix K is recorded as:

$$K = \begin{bmatrix} k(x_1,x_1) & \cdots & k(x_1,x_n) \\ \vdots & \ddots & \vdots \\ k(x_n,x_1) & \cdots & k(x_n,x_n) \end{bmatrix}. \quad (2)$$

For each input new observation x_{n+1}, assuming that the mean of the GP is zero, the joint Gaussian distribution of the outputs $y_{1:n}$ and y_{n+1} can be expressed as:

$$\begin{bmatrix} y_{1:n} \\ y_{n+1} \end{bmatrix} \sim N\left(0, \begin{bmatrix} K(X,X) & K(X,X_{n+1}) \\ K(X_{n+1},X) & K(X_{n+1},X_{n+1}) \end{bmatrix}\right). \quad (3)$$

Where, $K(X,X_{n+1})$ is the covariance matrix of the order $n\times(n+1)$ between the observation value and the training input samples, and is the covariance matrix of the observation value itself.

The posterior probability is obtained by calculating formula (4):

$$p(y_{n+1} \mid D_{1:n}, x_{n+1}) = N\left(\mu(x_{n+1}), \sigma^2(x_{n+1})\right), \quad (4)$$

Here:

$$\mu(x_{n+1}) = k^T K^{-1} y_{1:n}, \quad (5)$$

$$\sigma^2(x_{n+1}) = k(x_{n+1},x_{n+1}) - k^T K^{-1} k. \quad (6)$$

The GP can fit the corresponding test output value by calculating the above Process. It can be seen from equation (6) that the posterior variance of the GP depends on the test sample points. In BO, the acquisition function can use the information of the predicted mean and predicted variance of the GP to mine the next observation with high reliability. The acquisition function is introduced in Section 3.1.

B. Student's T process

Student's T Process (STP) is a generalization of GP, which refers to a functional distribution of an infinite set of random variables that obeys the joint Student's T distribution. For the Student's T distribution, we describe it as [18]:

$$\mathrm{T}(\mu,\Sigma,v) = \frac{\Gamma((v+d)/2)}{\Gamma(v/2)v^{d/2}\pi^{d/2}|\Sigma|^{1/2}} \cdot \left(1+\frac{1}{v}(y-\mu)^T\Sigma^{-1}(y-\mu)\right)^{-(v+d)/2}, \quad (7)$$

where d is the size of the T distribution, μ is the position parameter of the T distribution, Σ is the symmetric positive definite scattering matrix parameter of the T distribution, and $v>2$ is the degree of freedom.

$$\mathrm{E}\left[(\mathrm{y}-\mu)^T(\mathrm{y}-\mu)\right] = \frac{v}{v-2}\sum. \quad (8)$$

STP is parameterized by the mean function $m(x)$ and the covariance function $k(x,x')$; however, it has an additional parameter, the degrees of freedom v. The properties of STP can be determined jointly by $m(x)$, $k(x,x')$ and v, $x,x' \in R^d$ is an arbitrary random variable. Therefore, STP can be expressed as:

$$f(x) \sim STP\left(m(x), k(x,x'), v\right). \quad (9)$$

With increasing degrees of freedom, the multivariate Student's T distribution converges to a multivariate Gaussian distribution with the same mean, and the scattering parameter matrix approaches infinity.

In STP, $m(x)$ defines the prior expected value of each location, the kernel function represents the covariance of the objective function between the values of any two locations x and x_0, the joint distribution probability of a finite subset of locations is:

$$p(y \mid x) = T(\mu,\Sigma,v)(y) = T\left(\mu, \frac{v-2}{v}K, v\right)(y), \quad (10)$$

Where μ is the mean vector, $\mu_i = m(x_i)$, $K_{i,j} = k(x_i,x_j)$ is the kernel matrix.

Given a set of samples $D = [(x_1,y_1),\cdots,(x_n,y_n)]$, the posterior of STP is given by (11), (12), (13), (14).

$$p(y \mid x, D) = T\left(\mu, \frac{v-2}{v}K, v\right)(y), \quad (11)$$

$$\hat{\mu} = K_{x,x}K_{\tilde{x},\tilde{x}}^{-1}\tilde{y}, \quad (12)$$

$$\widehat{K} = \frac{\left(v+\tilde{y}^T K_{\tilde{x},\tilde{x}}^{-1}\tilde{y}-2\right)\cdot\left(K_{x,x}-K_{x,\tilde{x}}K_{\tilde{x},\tilde{x}}{}^{-1}K_{\tilde{x},x}\right)}{v+|D|-2}, \quad (13)$$

$$\hat{v} = v+|D|. \quad (14)$$

In general, the square exponential kernel is selected [30]:

$$K_{SEard}(x,x') = \sigma_f^2 \exp\left(-\frac{(x-x')^T(x-x')}{2\ell^2}\right), \quad (15)$$

where σ_f^2 is the signal variance,which also is the output scale amplitude, and the parameter ℓ is the input (length or time) scale.

Combining equation (13) with the kernel function, we can see that the posterior covariance of the STP depends on not only the test observations, but also the training observations [31]. Therefore, using a STP as a surrogate model for a BO will have a more flexible posterior variance than a GP. The hyperparameter optimization of the STP is obtained by maximizing the likelihood function, whose negative log-likelihood function has the form:

$$\begin{aligned} L(\theta) &= -\log p(y \mid x,\theta) \\ &= \frac{N}{2}\log((v-2)\pi) + \frac{1}{2}\log|K_\theta| \\ &\quad -\log\Gamma\left(\frac{v+N}{2}\right) + \log\Gamma\left(\frac{v}{2}\right) \\ &\quad + \frac{v+N}{2}\log\left(1+\frac{\beta}{v-2}\right). \end{aligned} \quad (16)$$

III. THE PROPOSED BAYESIAN OPTIMIZATION ALGORITHM

As a supervised learning method, BO can effectively seek the global optimal solution of the black-box objective function within the design space. By updating the prior knowledge of the objective function, we can obtain the corresponding observation value to update the posterior distribution closer, and find the optimal solution quickly [32].

The BO algorithm consists of two modules, the surrogate model module for fitting the objective function and the acquisition function module for acquiring new observations. The framework is shown in Fig. 1. The study of Bayesian architecture is inseparable from three directions: the construction of the surrogate model, the optimization of the surrogate model, and the design of the acquisition function.

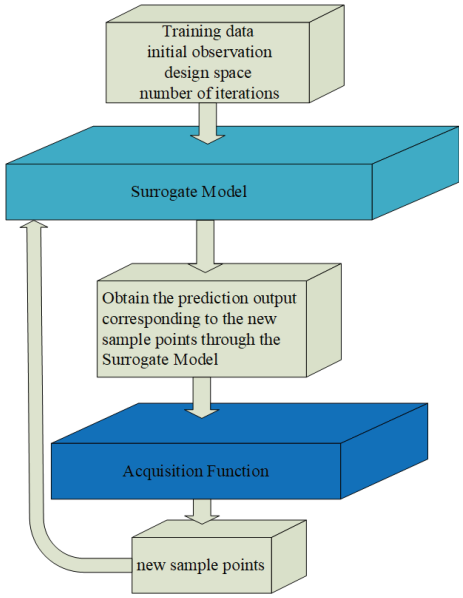

Fig. 1. Bayesian optimization framework.

In this paper, the STP is used as the surrogate model of BO, and the kernel function (17) without the β property is selected. The hyperparameters of the STP, including the degrees of freedom, noise variance, and hyperparameters of the kernel function, are globally optimized using the pattern search algorithm toolbox [33]. The optimization flowchart is shown in Fig. 2.

$$K_{SEisoU} = \exp\left(-\frac{1}{2\ell^2}(x-z)^T(x-z)\right). \tag{17}$$

The pattern search algorithm uses the negative log-likelihood of STP as the objective function to perform global optimization, obtain the final hyperparameters, and then determine the STP model. The model can output the corresponding prediction function value when given a new observation.

In the BO framework, the acqisition function use the information outputted by the surrogate model to explore the next observation. Common acquisition functions include confidence UCB/LCB [34, 35], EI [36], probability improvement (PI) function [26], entropy search (ES) function [37], EST [38] and ERM [39].

Martín presented a detailed derivation of GP upper/lower-confidence bound functions [36]:

$$\alpha_{\mathrm{UCB}}(x) = \mu_{t-1}(x) + \sqrt{\beta_t}\sigma_{t-1}(x), \tag{18}$$

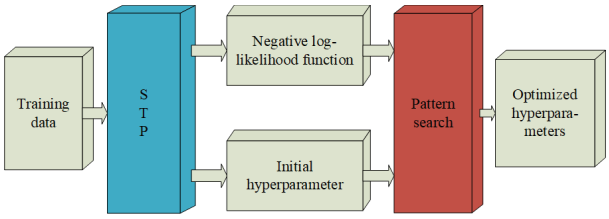

Fig. 2. Pattern search toolbox to optimize STP hyperparameters.

$$\alpha_{\mathrm{LCB}}(x) = \mu_{t-1}(x) - \sqrt{\beta_t}\sigma_{t-1}(x). \tag{19}$$

Where β_t is the assumed given learning rate, which are different from the LCB function under the GP. In this paper, the $\mu(x), \sigma(x)$ in LCB are changed to the prediction mean and prediction variance of STP.

Shah proposes a closed-form solution to the EI function for the STP [21]:

$$\alpha_{EI}(x;(x_n,y_n),\theta) = \gamma\sigma\Phi_v + N(\gamma(x)) + \sigma\left(1+\frac{\gamma(x)^2-1}{v+N-1}\right)\phi_v, \tag{20}$$

where

$$\gamma(x) = \sigma((x_n,y_n),\theta)^{-1}\left[f(x_{best} - \mu((x_n,y_n),\theta))\right]. \tag{21}$$

$\mu((x_n,y_n),\theta)$ and $\sigma((x_n,y_n),\theta)$ are represent the predicted mean and variance of STP, respectively, ϕ, Φ represent the probability density function and distribution function of T distribution, and θ define the set of hyperparameters of STP.

The estimation strategy function selects the maximum posterior value m in each iteration, which can be expressed as $\arg\max_{x\in\chi} \Pr(M_x|m,D_t)$, M_x is the event when the point reaches the maximum value. The EST function can be defined explicitly as:

$$\alpha_{EST}(x) = \frac{\hat{m} - \mu_{t-1}(x)}{\sigma_{t-1}(x)}. \tag{22}$$

Obtained by approximation, in this paper, the EST method mentioned in the literature [27] is used to obtain approximately $\hat{m}$. Unlike wang [27], we replace the predicted mean and predicted standard deviation of STP in the function $\mu(x), \sigma(x)$ respectively.

As a result, the pseudocode of the proposed BO algorithm, called BO-STP-EST in the paper, is presented in Algorithm 1.

IV. NUMERICAL EXPERIMENT

In order to verify the generalization performance and global optimization effect of the proposed BO-STP-EST algorithm, numerical experiment is carried out based on the multimodal function (23), where the independent variable interval is $[-512, 512]$. So we finally obtained the training data $X \in {}^{50\times1}, Y \in {}^{50\times1}$ through the program. The experimental goal is to find the global minimum of this function, and the total number of itera-

Algorithm 1 BO-STP-EST.

Require:

Sample set,$D_{1:n} = ((\tilde{x_1}, \tilde{y_1}), \cdots, (\tilde{x_n}, \tilde{y_n}))$;
Initial point,$x_0 = [x_1, x_2, \cdots, x_m]^T$;
The number of iterations,iters;
Lower bound and upper bound of the design space;

1: **for** each $i \in [1, iters]$ **do**
2: $D_{1:n} \rightarrow$ Optimize Hyperparameters for STP using pattern search algorithm, and then train STP;
3: $x_0 \rightarrow$Obtain the posterior prediction mean μ_{i-1} and posterior variance ${\sigma_{i-1}}^2$ of x_0 by the trained STP;
4: $\arg\min \frac{\hat{m}-\mu_{i-1}(x)}{\sigma_{i-1}(x)} \rightarrow x_i^{opt}$, Get the new sample points by the acquisition function;
5: ${x_i}^{opt} \rightarrow STP \rightarrow {f_i}^{opt}$, Use the trained STP to predict the objective function value corresponding to the input sample point;
6: f_{best} take the current minimum value, x_{best} ake the corresponding sample value;
7: **end for**

tions is set to 50. To verify the performance of the algorithm, we compare it with the BO-GP-LCB [1], BO-GP-EST [27], BO-STP-ERM [23], BO-STP-EI [21], and BO-STP-LCB. For the STP in the models of BO-STP-ERM, BO-STP-LCB, and BO-STP-EI, global optimization is not implemented. The experimental results are shown in Figs. 3 and 4.

$$y = -(x+47) \times \sin(\sqrt{|x+47|}) - 512 \times \sin(\sqrt{465-x}). \quad (23)$$

It can be seen intuitively from Fig. 3 that only the

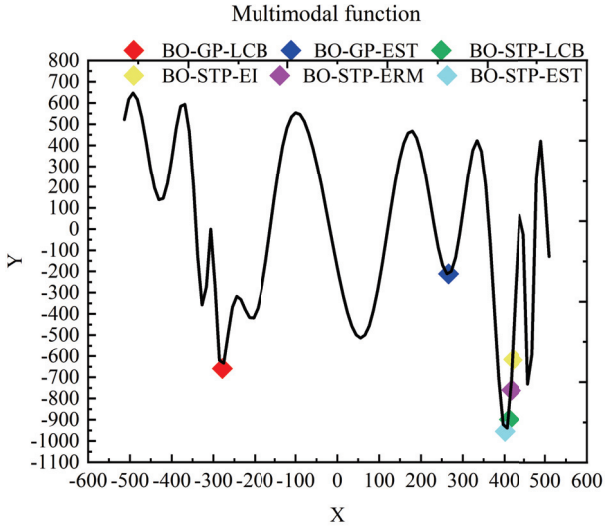

Fig. 3. The found minimum value by different models.

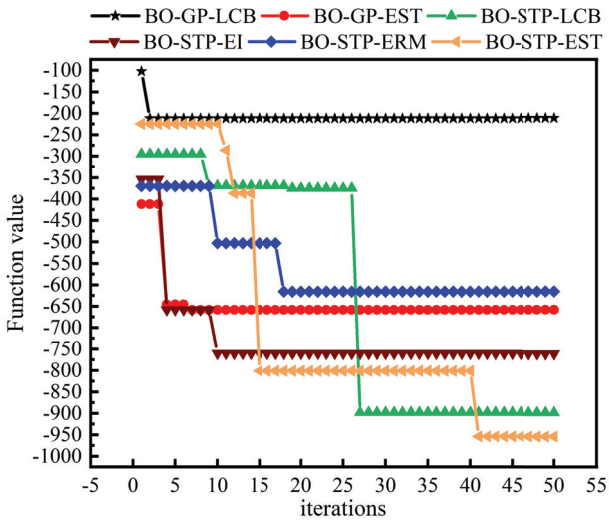

Fig. 4. Function value vs. iteration numbers of different models.

BO-STP-EST proposed in this paper finds the global minimum of the multimodal function. Models such as BO-GP-LCB and BO-GP-EST are trapped in the local minimum of the function, and other BO algorithms are close to the global minimum of the function, which shows that the proposed BO algorithm has a strong global optimization ability. As can be seen from Fig. 4, since we set the first iteration to be the new sample point explored by the model corresponding to the objective function value, the starting points in the figure are inconsistent, which also just shows that the ability of different models to explore sample points is different.

Although the objective function value obtained by BO-GP-LCB for the first time is the smallest, it never explores a function value smaller than the current value after 4th time. Compared with the same acquisition function with EST, the exploration ability of the BO algorithm with the GP as the surrogate model is much lower than that of the BO algorithm with the STP as the surrogate model. Compared with the same surrogate model algorithm, the prediction accuracy of the proposed BO-STP-EST algorithm after hyperparameter optimization is significantly higher than that of other models.

V. OPTIMAL DESIGN OF MICROSTRIP ANTENNAS

A. Printed dipole antenna

The printed dipole antenna comes from the literature [40] and its structure is shown in Fig. 5. The whole antenna can be divided into five parts, which are the dielectric layer, the dipole antenna arm, the microstrip balun line, the microstrip transmission line, and the antenna feeding surface, The dimensional parameters of

Table 1: Antenna size parameters

Variable	Value/mm
L1	21.5
L2	21.5
L3	9.8
W1	3
W2	3
W3	3.5
ε_r	4.4
h	1.6

the antenna are shown in Table 1. The working frequency of the antenna is 2.25 GHz-2.72 GHz, and the design index include that its working frequency is 2.45 GHz, and the return loss S11 is less than -15 dB.

As shown in Fig. 5, the antenna has many variables that affect its performance. We select five size variables that have more significant impact as input, as shown in Table 2, including the transmission line length L1, one dipole arm the length L2, the side length L3 of the balun triangle, the right angle length L4 of the base of the balun triangle, and the width W3 of the balun rectangle.

Therefore, the input is $X = [L_1, L_2, L_3, L_4, W_3]$, the output is the resonant frequency, while other parameters are fixed. The HFSS-MATLAB-API [41] program is used for the co-simulation of the antenna using the orthogonal experiment method. The frequency sweep range is 2 GHz through 3 GHz, and the step size is 0.01 GHz. So, each group of antenna size variables corresponds to 100 resonance frequency points. The training sample size is $X \in {}^{50\times5}, Y \in {}^{50\times1}$.

According to the design index of the antenna, the design objective function is (24), where $f_{resonant} = 2.45\ GHz$, $f_{prediction}$ is the predicted resonant frequency.

$$f_{\text{objective}} = \left|2.45 - f_{\text{prediction}}\right|^2 \& f_{\text{resonant}} < -15\ dB. \tag{24}$$

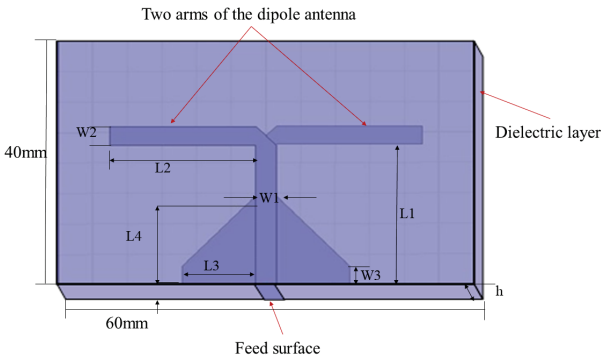

Fig. 5. The found minimum value by different models.

Table 2: Design range and initial design value of the printed dipole antenna

Variable	Min/mm	Max/mm	Initial value/mm
L1	21	23	21.5
L2	20	22.5	21.5
L3	9	10.5	9.8
L4	11.5	13	12.6
W3	3	5	3.5

In order to verify the effectiveness of the BO-STP-EST algorithm proposed in this paper, the BO-GP-LCB, BO-GP-EST, BO-STP-LCB, BO-STP-EI, BO-STP-ERM, and the BO-STP-EST are compared. The iterative performance of the objective function under different models, the optimization results of the antenna size and the actual simulation results of the optimized antenna size are verified by experiments. The design space and initial sample points are shown in Table 2, and the total number of iterations is 50 times. The experimental environment is Inter(R)Corte(TM)i5-7500 CPU @ 3.40 GHz 16GB RAM, MATLAB2019b.

From Fig. 6 and Table 3, we can see that the proposed BO-STP-EST exhibits a good generalization ability, and it can find the minimum in a few iterations. Compared with the BO algorithm with GP as the surrogate model, BO-GP-LCB find a smaller value in the 41st time, but this minimum value is very different from other models. For the same acquisition function, BO-GP-EST takes more time to find the minimum at the 8th iteration, and the proposed BO-STP-EST performs much better than BO-GP-EST, where it finds the minimum value at the 3rd

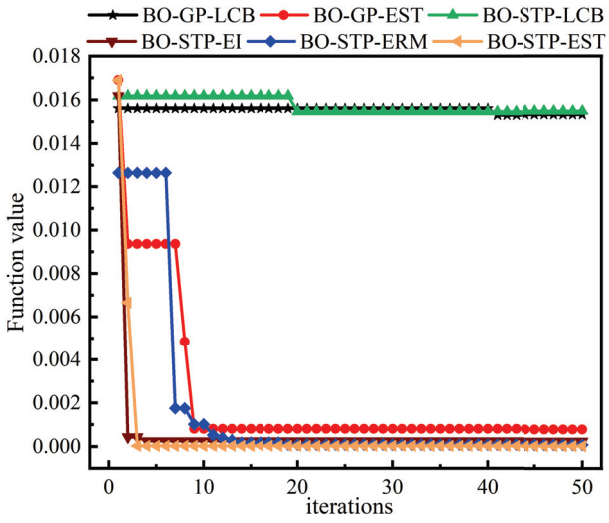

Fig. 6. The found minimum value by different models.

Table 3: Optimization results of different models of the printed dipole antenna

Model	L1	L2	L3	L4	W3	Iteration	$f_{objective}$	time
BO-GP-LCB	23	20.1999	9.0208	12.6053	3	41	1.53e-02	106.8259
BO-GP-EST	22.4373	20.7785	9	12.9988	3.2000	8	8.03e-04	105.4107
BO-STP-LCB	23	22.5000	10.6000	11.5000	3	20	1.55e-02	60.3916
BO-STP-EI	22.8226	21.2913	9.6366	12.1941	3.8591	5	2.65e-04	115.4727
BO-STP-ERM	22.4044	20.0226	9.9722	11.5997	4.5191	19	8.60e-05	137.3362
BO-STP-EST	23	21.0537	10.5999	11.5000	3	3	2.88e-05	93.5832

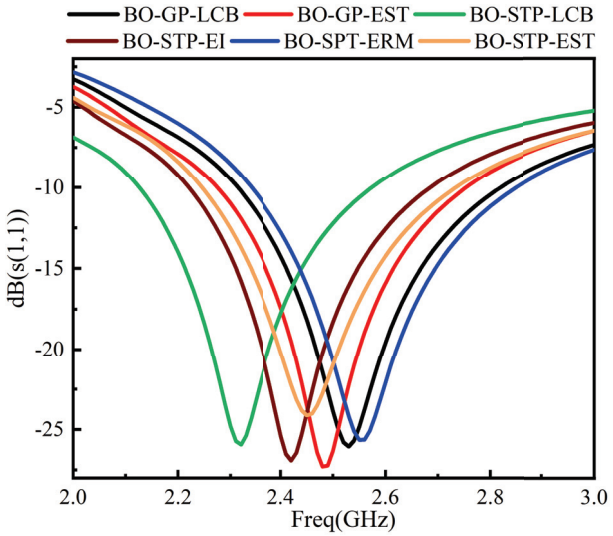

Fig. 7. The found minimum value by different models.

iteration. Compared with other models with STP, BO-STP-EI and BO-STP-ERM are not as good as BO-STP-EST in terms of the objective function and time consumption because the optimized STP has fitting higher-degree posterior outputs which makes the EST collection function have stronger exploration ability.

The antenna optimization results in Fig. 7 verified by HFSS illustrate that, for the design index of the resonant frequency of the antenna, only the proposed BO-STP-EST achieves the design targets with the resonant frequency 2.45 GHz and where $S_{11} < -15$ dB. The resonant frequency points predicted by other models have certain errors, which are also in line with the prediction results of the objective function in Table 3 and Table 4. It can be concluded from the above tables and figures that the proposed BO-STP-EST has greater advantages in convergent speed and accuracy than other models.

B. E-shaped antenna

The E-shaped antenna is evolved from the rectangular patch antenna, and two identical parallel slot antennas are formed by using the slot-loading method [42]. For the E-shaped antenna, it is easy to obtain good performance by adjusting the shape of the slot, which is very suitable for use in portable communication and miniaturized equipment. The E-shaped antenna is shown in Fig. 8, which consists of a radiation patch, a ground plate, a dielectric plate, and a feeding point.

Table 4: The actual resonant frequencies optimized by different models of the printed dipole antenna

Model	Resonant frequency/GHz	Return loss/dB
BO-GP-LCB	2.53	−26.0488
BO-GP-EST	2.49	−27.2250
BO-STP-LCB	2.32	−25.9310
BO-STP-EI	2.42	−26.9227
BO-STP-ERM	2.56	−25.6303
BO-STP-EST	2.45	−24.1248

Table 5: Design range and initial design value of the E-shape antenna

Variable	Min/mm	Max/mm	Initial value/mm
L	25	35	26
W	20	28	29
ls	2	8	4
ws	4	18	7
h	1.57	3.57	1.6

The design index is the working frequency 3.50 GHz, where the return loss S11 is less than −10 dB. According to the structure of the antenna, several parameters that greatly affect the performance of the antenna, including L, W, ls, ws, h, are selected as the training input of the model, and the rests are unchanged, including the dielectric material $\varepsilon_r = 2.33$, as shown in Table 5.

Therefore, the input is $X = [L, W, ls, ws, h]$, and the output is $f_{resonant}$. The frequency sweep range is 2 GHz-5 GHz, the step size is 0.01 GHz. So, each group of antenna size variables corresponds to 100 resonance frequency points, and the training data $X \in {}^{41\times4}, Y \in {}^{41\times1}$ is finally obtained.

To verify the generalization and optimization performance of the proposed BO-STP-EST, we compare

Table 6: Results obtained by different models for the E-shape antenna

Model	L	W	ls	ws	h	Iteration	$f_{objective}$	time
BO-GP-LCB	35	28	2	4.84	3.57	6	0.105	106.83
BO-GP-EST	30.09	24.12	5	14.5	2.57	12	1.616e-05	115.19
BO-STP-LCB	25	28	2	18	1.64	28	0.0424	165.4
BO-STP-EI	30.89	20.30	2.50	16.05	2.77	41	0.0372	198.42
BO-STP-ERM	26.20	27.71	8	16.10	2.62	42	7.626e-05	220
BO-STP-EST	35	28	8	4.95	3.57	7	5.313e-05	197.03

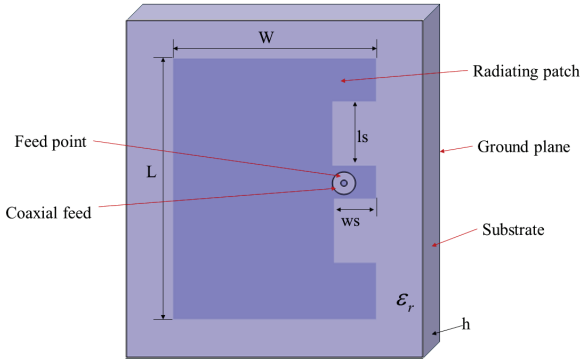

Fig. 8. E-shaped antenna structure diagram.

the performances of the BO-GP-LCB, BO-GP-EST, BO-STP-LCB, BO-STP-EI, and BO-STP-ERM. The design objective function is (25), where $f_{resonant} = 3.50\ GHz$, $f_{prediction}$ is the predicted resonant frequency.

$$f_{\text{opt}} = \left|3.50 - f_{\text{prediction}}\right|^2 \& f_{\text{resonant}} < -10\ dB. \quad (25)$$

The experiment compares the differences in the number of iterations, the minimum value, and the duration of the six models. The results are shown in Table 6. The return loss of the antenna obtained by the final optimization of each model is also compared, and the results are shown in Fig. 9 and Table 6.

As can be seen from Fig. 9, since the sample points recorded in the first setting of the model program are ones collected by the acquisition function, we can see the ability of different models to explore the sample points in the sample space. Compared with the same acquisition function EST, although the value of the objective function corresponding to the sample points first explored by the proposed BO-STP-EST algorithm is greater than BO-GP-EST, it is much stronger than BO-GP-EST in the subsequent exploration ability. It finds the global minimum value in the 7th iteration and is better than that found by BO-GP-EST in the 12th iteration.

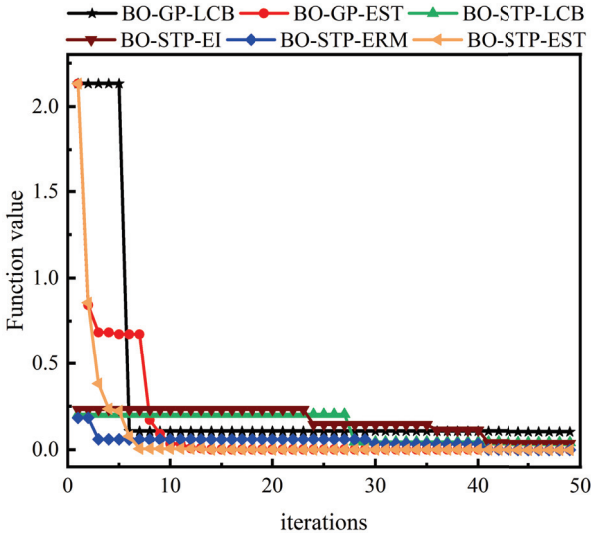

Fig. 9. Objective functions vs. iteration of different model for the E-shape antenna.

Compared with other models by STP, BO-STP-EST can find the minimum value of objective function which is much smaller than BO-STP-LCB and BO-STP-EI. As we can see from table 6,7, although the final objective function value found by BO-STP-ERM is close to BO-STP-EST, it takes more time. Therefore, BO-STP-EST is still the most competitive among several models in terms of minimum value and time-consuming of objective function.

In the experiment of this part, we deliberately reduce the number of training samples, so as to verify that the hyperparametric optimization of the model can improve the prediction ability of the algorithm proposed in this paper when the training samples are reduced. The simulation results (Fig. 10) verified by HFSS show that when the training samples are reduced (Table 7), the prediction accuracy of the different models mentioned in the

Table 7: The actual resonant frequencies optimized by different models of the printed dipole antenna

Model	Resonant frequency/GHz	Return loss/dB
BO-GP-LCB	3.49	−13.460
BO-GP-EST	3.69	−33.945
BO-STP-LCB	3.30	−17.399
BO-STP-EI	4.27	−20.067
BO-STP-ERM	3.19	−28.231
BO-STP-EST	3.50	−12.837

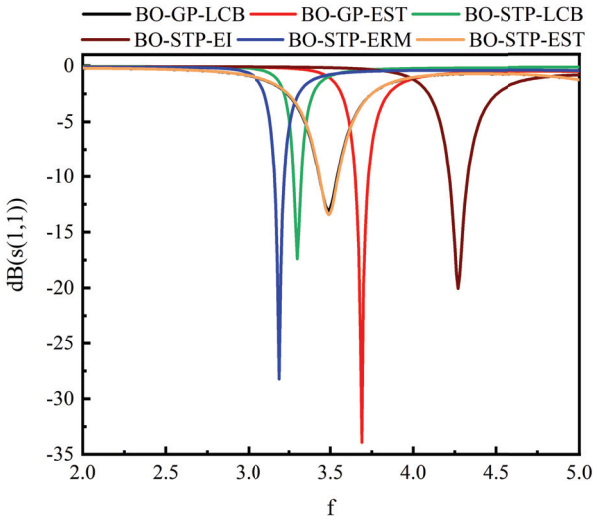

Fig. 10. Simulation results obtained by different models for the E-shape antenna.

paper begins to decline, however, the accuracy of the BO-STP-EST is much higher than that of the algorithm without global hyperparametric optimization. Taking the STP as surrogate model, the algorithm still maintains good prediction accuracy under the condition of reducing the number of training samples. At the same time, the proposed BO-STP-EST realizes the design index of $S_{11} < -10\ dB$ at the resonant frequency at 3.5 GHz. It shows that the hyper-parameter optimization of surrogate model can improve the accuracy and optimization performance of Bayesian optimization algorithm.

VI. CONCLUSION

This paper proposes a BO algorithm that combines an improved maximum evaluation policy function with a hyperparameter-optimized STP. Numerical experimental verification of finding the minimum value through multimodal functions shows that the proposed BO algorithm with the STP as the surrogate model has better prediction accuracy than these with the GP as the surrogate model. At the same time, the acquisition function EST can improve the exploration ability of the BO algorithm. The proposed algorithm in this paper is applied to the antenna modeling problems, and the design index can be well completed. The simulation results of electromagnetic simulation software also verify the effectiveness of the algorithm.

Although the proposed algorithm is only applied to the optimization problem of single-band antennas in this paper, following, we will study the multi-band antenna optimization by the proposed algorithm.

ACKNOWLEDGMENT

This work was supported by the special projects in key fields of Guangdong Universities of China under No. 2022ZDZX1020, the scientific research capacity improvement project of key developing disciplines in Guangdong Province of China under No. 2021ZDJS057, and the university scientific research project of Bureau of Education of Guangzhou Municipality of China under No. 202234598.

REFERENCES

[1] L. Acerbi and W. J. Ma, "Practical Bayesian optimization for model fitting with Bayesian adaptive direct search," *Advances in Neural Information Processing Systems*, vol. 30, 2017.

[2] V. Nguyen, S. Schulze, and M. Osborne, "Bayesian optimization for iterative learning," *Advances in Neural Information Processing Systems*, vol. 33, pp. 9361-9371, 2020.

[3] M. Wistuba and J. Grabocka, "Few-shot bayesian optimization with deep kernel surrogates," *arXiv preprint arXiv:2101.07667*, 2021.

[4] D. Yenicelik, "Parameter Optimization using high-dimensional Bayesian Optimization," *arXiv preprint arXiv:2010.03955*, 2020.

[5] J. Mockus, V. Tiesis, and A. Zilinskas, "The application of Bayesian methods for seeking the extremum," *Towards Global Optimization*, vol. 2, no. 117-129, p. 2, 1978.

[6] L. Breiman, "Random forests," *Machine Learning*, vol. 45, no. 1, pp. 5-32, 2001.

[7] J. Snoek, O. Rippel, K. Swersky, R. Kiros, N. Satish, N. Sundaram, M. Patwary, M. Prabhat, and R. Adams, "Scalable bayesian optimization using deep neural networks," *International Conference on Machine Learning*, pp. 2171-2180, 2015.

[8] S. R. Chowdhury and A. Gopalan, "No-regret algorithms for multi-task bayesian optimization," *International Conference on Artificial Intelligence and Statistics*, pp. 1873-1881, 2021.

[9] D. Ginsbourger, R. L. Riche, and L. Carraro, "Kriging is well-suited to parallelize optimization," *Computational Intelligence in Expensive Optimization Problems*, pp. 131-162, 2010.

[10] Z. Feng, Q. Zhang, Q. Zhang, Q. Tang, T. Yang, and Y. Ma, "A multiobjective optimization based framework to balance the global exploration and local exploitation in expensive optimization," *Journal of Global Optimization*, vol. 61, no. 4, pp. 677-694, 2015.

[11] S. Han, Y. Tian, W. Ding, and P. Li, "Resonant frequency modeling of microstrip antenna based on deep kernel learning," *IEEE Access*, vol. 9, pp. 39067-39076, 2021.

[12] T. Zhang, Y. Tian, X. Chen, and J. Gao, "Antenna Resonant Frequency Modeling based on AdaBoost Gaussian Process Ensemble," *Applied Computational Electromagnetics Society (ACES) Journal*, pp. 1485-1492, 2020.

[13] A. O'Hagan, "On outlier rejection phenomena in Bayes inference," *Journal of the Royal Statistical Society: Series B (Methodological)*, vol. 41, no. 3, pp. 358-367, 1979.

[14] A. Shah, A. Wilson, and Z. Ghahramani, "Student-T processes as alternatives to Gaussian processes," *Artificial Intelligence and Statistics*, pp. 877-885, 2014.

[15] A. Solin and S. Särkkä, "State space methods for efficient inference in Student-t process regression," *Artificial Intelligence and Statistics*, pp. 885-893, 2015.

[16] Q. Tang, L. Niu, Y. Wang, T. Dai, W. An, J. Cai, and S.-T. Xia, "Student-T process regression with Student-T likelihood," *IJCAI*, pp. 2822-2828, 2017.

[17] Z. Chen, B. Wang, and A. N. Gorban, "Multivariate Gaussian and Student-T process regression for multi-output prediction," *Neural Computing and Applications*, vol. 32, no. 8, pp. 3005-3028, 2020.

[18] W. Wang, Q. Yu, and M. Fasli, "Altering Gaussian process to Student-T process for maximum distribution construction," *International Journal of Systems Science*, vol. 52, no. 4, pp. 727-755, 2021.

[19] L. Kang, R.-S. Chen, N. Xiong, Y.-C. Chen, Y.-X. Hu, and C.-M. Chen, "Selecting hyper-parameters of Gaussian process regression based on non-inertial particle swarm optimization in Internet of Things," *IEEE Access*, vol. 7, pp. 59504-59513, 2019.

[20] Z. Le, L. Zhong, Z. Jianqiang, and R. Xiongwei, "Improved Gaussian process model based on artificial bee colony algorithm optimization," *Journal of National University of Defense Science and Technology*, p. 7, 2014.

[21] A. Shah, A. G. Wilson, and Z. Ghahramani, "Bayesian optimization using Student-T processes," *NIPS Workshop on Bayesian Optimization*, 2013.

[22] B. D. Tracey and D. Wolpert, "Upgrading from Gaussian processes to Student's T processes," *2018 AIAA Non-Deterministic Approaches Conference*, p. 1659, 2018.

[23] C. Clare, G. Hawe, and S. McClean, "Expected regret minimization for bayesian optimization with Student's-T processes," *Artificial Intelligence and Pattern Recognition*, pp. 8-12, 2020.

[24] W. Ding, Y. Tian, P. Li, H. Yuan, and R. Li, "Antenna optimization based on master-apprentice broad learning system," *International Journal of Machine Learning and Cybernetics*, vol. 13, no. 2, pp. 461-470, 2022.

[25] J. Gao, Y. Tian, X. Zheng, and X. Chen, "Resonant frequency modeling of microwave antennas using Gaussian process based on semisupervised learning," *Complexity*, vol. 2020, 2020.

[26] H. M. Torun, M. Swaminathan, A. K. Davis, and M. L. F. Bellaredj, "A global Bayesian optimization algorithm and its application to integrated system design," *IEEE Transactions on Very Large Scale Integration (VLSI) Systems*, vol. 26, no. 4, pp. 792-802, 2018.

[27] Z. Wang, B. Zhou, and S. Jegelka, "Optimization as estimation with Gaussian processes in bandit settings," *Artificial Intelligence and Statistics*, pp. 1022-1031, 2016.

[28] C. E. Rasmussen, "Gaussian processes in machine learning," *Summer School on Machine Learning*, pp. 63-71, 2003.

[29] W. P. du Plessis and J. P. Jacobs, "Improved Gaussian Process Modelling of On-Axis and Off-Axis Monostatic RCS Magnitude Responses of Shoulder-Launched Missiles," *Applied Computational Electromagnetics Society (ACES) Journal*, pp. 1750-1756, 2019.

[30] J. Vanhatalo, P. Jylänki, and A. Vehtari, "Gaussian process regression with Student-t likelihood," *Advances in Neural Information Processing Systems*, vol. 22, 2009.

[31] Q. T. Y. Wang and S.-T. Xia, "Student-T process regression with dependent Student-t noise," *ECAI 2016: 22nd European Conference on Artificial Intelligence*, 29 August-2 September 2016, The Hague, The Netherlands-Including Prestigious Applications of Artificial Intelligence (PAIS 2016), vol. 285, p. 82, 2016.

[32] S. Greenhill, S. Rana, S. Gupta, P. Vellanki, and S. Venkatesh, "Bayesian optimization for adaptive experimental design: A review," *IEEE Access*, vol. 8, pp. 13937-13948, 2020.

[33] A. M. Beigi and A. Maroosi, "Parameter identification for solar cells and module using a hybrid firefly

and pattern search algorithms," *Solar Energy*, vol. 171, pp. 435-446, 2018.

[34] D. Calandriello, L. Carratino, A. Lazaric, M. Valko, and L. Rosasco, "Gaussian process optimization with adaptive sketching: Scalable and no regret," *Conference on Learning Theory*, pp. 533-557, 2019.

[35] L. A. Martín and E. C. Garrido-Merchán, "Many Objective Bayesian Optimization," *arXiv preprint arXiv:2107.04126*, 2021.

[36] L. Tani and C. Veelken, "Comparison of Bayesian and particle swarm algorithms for hyperparameter optimisation in machine learning applications in high energy physics," *arXiv preprint arXiv:2201.06809*, 2022.

[37] J. M. Hernández-Lobato, M. W. Hoffman, and Z. Ghahramani, "Predictive entropy search for efficient global optimization of black-box functions," *Advances in Neural Information Processing Systems*, vol. 27, 2014.

[38] I. Bogunovic and A. Krause, "Misspecified gaussian process bandit optimization," *Advances in Neural Information Processing Systems*, vol. 34, 2021.

[39] V. Nguyen and M. A. Osborne, "Knowing the what but not the where in Bayesian optimization," *International Conference on Machine Learning*, pp. 7317-7326, 2020.

[40] W.-T. Ding, F. Meng, Y.-B. Tian, and H.-N. Yuan, "Antenna optimization based on auto-context broad learning system," *International Journal of Antennas and Propagation*, vol. 2022, 2022.

[41] W. Tian, D. Wu, Q. Chao, Z. Chen, and Y. Wang, "Application of genetic algorithm in M× N reconfigurable antenna array based on RF MEMS switches," *Modern Physics Letters B*, vol. 32, no. 30, p. 1850365, 2018.

[42] D. Ustun, A. Toktas, and A. Akdagli, "Deep neural network–based soft computing the resonant frequency of E–shaped patch antennas," *AEU-International Journal of Electronics and Communications*, vol. 102, pp. 54-61, 2019.

Qing Li was Born in Anqing, Anhui Province, China, studying in Jiangsu University of science and technology, master's degree, research direction: intelligent optimization algorithm, intelligent electromagnetic optimization.

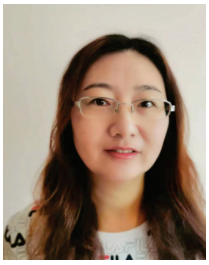

Fei Meng was born in Shenyang, Liaoning Province, China, in 1977. She is currently with the School of Information and Communication Engineering, Guangzhou Maritime University, Guangzhou, China. She has authored and coauthored 10 Journal papers. Her research interest is surrogates and their applications.

Yubo Tian was born in Tieling, Liaoning Province, China, in 1971. He received the Ph.D. degree in radio physics from the De-partment of Electronic Science and Engineering, Nanjing University, Nanjing, China. He has been a visiting scholar at the University of California Los Angeles in 2009 and the Griffith University in 2015, respectively. From 1997 to 2004, he was with the Department of Information Engineering, Shenyang University, Shenyang, China. From 2005 to 2020, he was with the School of Electronics and Information, Jiangsu University of Science and Technology, Zhenjiang, China, where he was a full professor and vice Dean from 2011. He is currently with the School of Information and Communication Engineering, Guangzhou Maritime University, Guangzhou, China. Dr. Tian has authored and coauthored more than 100 Journal papers and 3 books. He also holds more than 20 filed/granted China patents. His current research interest is Machine Learning methods and their applications in electronics and electromagnetics.

Xiaoyan Wang studying in Jiangsu University of science and technology, master's degree, research direction: intelligent optimization algorithm, intelligent electromagnetic optimization.

Eight-port Diagonal Antenna with High Isolation and High Efficiency for 5G Smartphone

Rui Shao, Junlin Wang*, Xin Wang*, and Yonghao Wang

College of Electronic and Information Engineering
Inner Mongolia University, Hohhot, 010021, China
17853313635@163.com, *wangjunlin@imu.edu.cn, *wangxin219@imu.edu.cn, yhwangimu@163.com

Abstract – In this letter, an 8×8 multiple-input-multiple-output (MIMO) antenna that operates in the sub-6 GHz (4.7-5.1 GHz) spectrum for 5G MIMO smartphone applications is presented. The design consists of a fully grounded plane with closely orthogonal antenna pairs placed symmetrically on the corners of the smartphone and each antenna element consists of an F-type monopole with dimensions of 18×7.5 mm^2. Firstly, the diversity characteristics of orthogonally placed antennas are used to reduce the coupling between antennas. On the other hand, diagonal antennas are connected by a neutral line (NL) to further improve isolation and etched slots on the ground to reduce the coupling between antenna pairs. A good frequency bandwidth ($S_{11} < -10$ dB) of 4.7-5.1 GHz has been obtained for the MIMO antenna, and the isolation is lower than 16 dB. In addition, total efficiency (TE) is greater than 77.5%, and the envelope correlation coefficient (ECC) is lower than 0.025. The fabricated antenna prototype is tested and offers good performance.

Index Terms – high efficiency, high isolation, MIMO, smartphone antenna.

I. INTRODUCTION

With the rapid development of communication technology, people's demand for the throughput of mobile communication system is increasing, which has become the main factor for the fifth generation (5G) mobile communication. In the 5G era, it is compatible with 2G / 3G / 4G, WiFi, Bluetooth, satellite navigation and other systems and standards. The number of antennas in the system increases sharply, and the MIMO antenna is regarded as an appropriate choice for 5G mobile applications. One of the main challenges in MIMO antenna design is the isolation enhancement and low ECC within a compact size. Several techniques exist that can improve the isolation between antenna elements for mobile communication when they are closely spaced together.

Distance optimization and selection of different elements are easy methods without employing any other structure to suppress coupling between antennas [1, 4]. An ultra-wideband (3.3-6 GHz) eight-antenna MIMO array was better than 11 dB by selecting an appropriate distance between neighboring elements [4]. Since space is limited, the improvement of isolation is limited by adjusting only the distance between elements. However, adjusting the distance between elements to obtain acceptable isolation may result in a large size of the MIMO system, which cannot meet the requirements of small space.

Adding external decoupling structure is an efficient method to further improve the isolation, such as the (NL) technique, defected ground structure (DGS) technique, and grounded branch. The NL technique is firstly presented by Diallo in 2006 [5]. The principle of this technology is that the NL connects the antenna radiation element, and the current generated in the NL is the same amplitude and opposite phase as the excited antenna, which cancels out the coupling current, thereby reducing the coupling between the antenna elements; this technique has been demonstrated successfully in [6, 8]. However, when the NL structure is connected to the antenna elements, the improper selection of the connection position will make it resonate with the radiator. The DGS is a slot structure etched on the ground. The slot structure can be equivalent to a filter, which limits the ground current from ant 1 to ant 2 to suppress the coupling caused by the current on the ground surface. High isolation can be realized by loading the DGS to block coupling current [9, 11]. In general, when using the DGS to improve the isolation of the MIMO antenna, the etched structure needs to satisfy that its length is greater than a quarter wavelength. The disadvantage of the DGS is that when the antenna works at a high frequency, the overall size of the antenna cannot be guaranteed to meet the long wavelength due to the limitation of antenna miniaturization. The principle of enhancing the isolation of the MIMO antenna by loading the grounded branch is that by increasing the coupling path, the current generated by the excited antenna element is more coupled to the grounded branch, and only a small amount of current is coupled

Submitted On: January 24, 2022
Accepted On: September 12, 2022

https://doi.org/10.13052/2022.ACES.J.370805

to another antenna element [12, 13]. Ref [12] presented a compact dual-band MIMO antenna operating at 3.3 - 3.6 GHz, and the isolation between inner antenna elements was improved from 10 dB to 15.1 dB by introducing a grounded branch. The disadvantage of the method is that the coupling of the grounded branch would affect the impedance matching of the antenna and reduce the radiation efficiency of the antenna.

In addition to the above-mentioned partial decoupling techniques, there are other decoupling techniques. In [14], a very compact building block composed of two asymmetrically mirrored loop antennas was proposed to implement a multi-antenna MIMO array (operating at 3.4-3.6 GHz). Acceptable isolation was attained by asymmetrically arranging the two mirrored loop antennas. To reduce coupling, self-isolated antennas have been investigated [15–17]. In [17], the compact design structure was composed of inverted U-shaped and two circular-ring structures embedded across two vertical stubs, and the antenna achieved good isolation between the four-antenna elements without using any additional decoupling techniques at 3.5 GHz. In [18] and [19], a mode cancellation method is also proposed to design shared-radiator antenna pairs across a wide bandwidth operating at sub-6 GHz. In [20, 21], high isolation without additional decoupling structures is achieved under the shared radiation patch by equivalent transmission theory or mode orthogonality. In [22], a wideband planar inverted-F antenna (PIFA) covering n77/n78/n79 and LTE band 46 was designed by using multimode technology. By combining two PIFAs, the design of high isolation and advanced MIMO antenna is realized. In [23], two orthogonally polarized antennas (3.4-3.6 GHz) were excited by the odd-even mode of coplanar waveguide feed, and the isolation performance is better than 20 dB.

For the proposed eight-port diagonal MIMO smartphone antenna proposed in this paper, the layout between the antenna elements is orthogonal, and the low mutual coupling is realized by spatial diversity technology. The antenna structure is simple, and high isolation can be achieved without additional decoupling structure and complex operation. Then, the proposed antenna achieved a compact, high isolation, and high efficiency assisted by other techniques. Finally, the overall ground space occupied by the antenna is very small, leaving a lot of space for other types of antennas.

II. ANTENNA PAIR

A. Structure of the antenna pair

For the proposed eight-port MIMO antenna, the study designed an antenna pair firstly as shown in Fig. 1. The proposed antenna pair was simulated using the full-wave simulation software HFSS version 2020, and it was

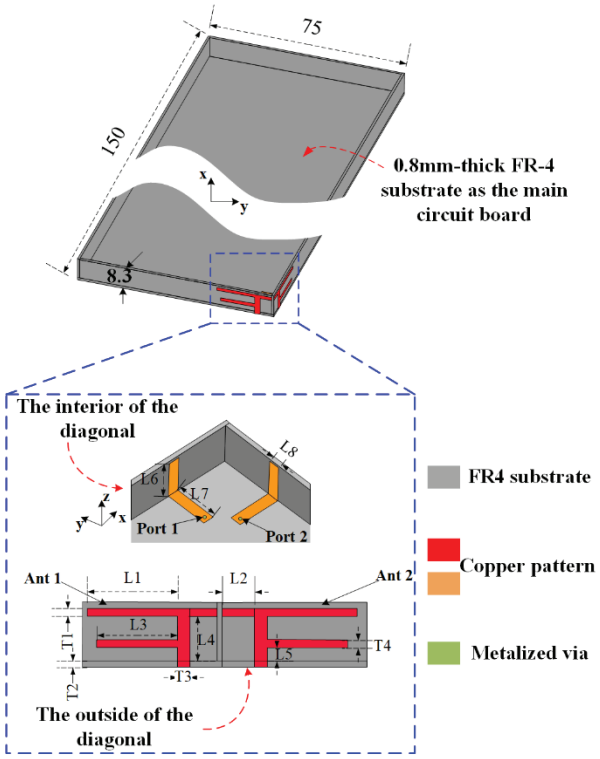

Fig. 1. Geometry of the realized antenna pair.

Table 1: Parameters dimension of the design

Parameters	Value, mm	Parameters	Value, mm
L1	16	L7	8
L2	4.4	L8	2
L3	13	T1	1
L4	5.7	T2	0.8
L5	1.7	T3	2
L6	7	T4	1

simulated based on the high precision solution of automatic mesh generation technology.The optimal dimensions for each single antenna element are summarized in Table 1. The size of the system ground plane was $0.8 \times 75 \times 150$ mm^3, typical for the dimension of a 5.3-inch handset, and four dielectric substrates (dielectric constant is 4.4, loss tangent is 0.02) are placed vertically around the system ground as borders, and the thickness of all dielectric substrates was 0.8 mm. As shown in Fig. 1, a pair of F-type monopole structures (red) was etched outside the dielectric substrate, and the feeder (orange) was etched inside. The antenna pair was placed orthogonally on the corner of the border, and the length of the longer side above was 16 mm, and the length of the shorter side below was 13 mm. The F-type monopole

was fed by the microstrip feed line (while connecting to 50 Ω SMA connectors when measuring.) to make the antenna work at 4.9 GHz.

Configurations and S-parameter (S_{11} and S_{21}) results of the F-type antenna pair without the NL and the final design are illustrated and compared in Figs. 2 (a)-(b), respectively. We can see that the resonant frequency of the antenna pair at 4.9 GHz ($S_{11} < -10dB$) from the results obtained shown in Fig. 2 (a), and the isolation is 14 dB. From what we know, the above performance can meet the general requirement of smartphone MIMO antennas. Based on the above structure, we made a further attempt, that is, a NL was introduced between the two antenna elements as shown in Fig. 2 (b). We can observe that the resonant frequency and bandwidth of the antenna pair did not change, but the isolation of the antenna is 17 dB, which is a reduction of 3 dBi. Therefore, we finally adopted the second structure.

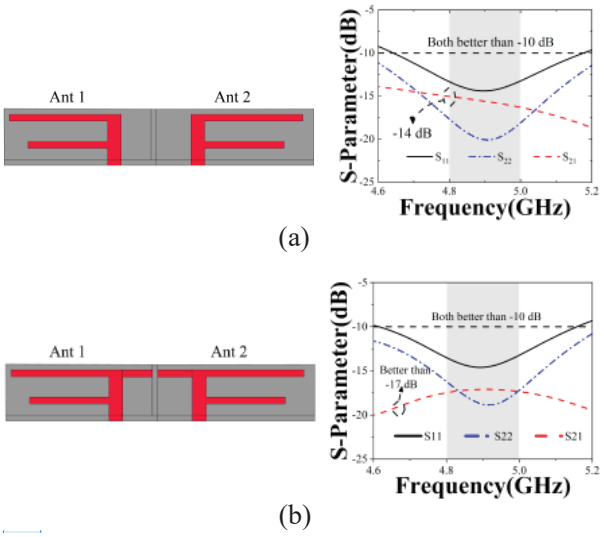

Fig. 2. Different configurations and S-parameter for the antenna design with (a) without the NL, (b) the proposed.

B. Parameter analysis

In the process of antenna design, the parameter scan is usually performed to select the most suitable parameter. Here, two scanned parameters were set up to determine the most suitable parameter by analyzing the S-parameter in Figs. 3 (a)-(b).

Figure 3 (a) investigates the effects of the long side (L_1) of F-type monopoles on the operation band. We can see from Fig. 3 (a), when its size changes from 13 to 19 mm. The resonant frequency of the design varies from 5.5 to 4.5 GHz. When L_1=16 mm, the resonant frequency is 4.9 GHz. It can be also affected by changing the short side (L_3) of the F-type monopole. As shown Fig. 3 (b), the resonant frequency tunes to lower or upper frequencies with the change of L_3. When L_3=13 mm, the resonant frequency is at 4.9 GHz. Therefore, L_1=16 mm and L_3=13 mm are selected to the final design.

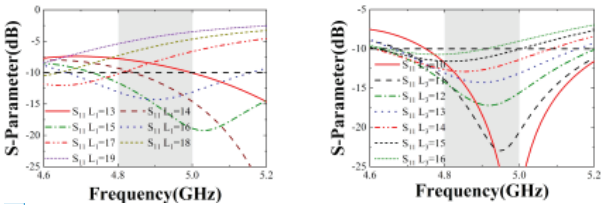

Fig. 3. Simulated results of the proposed antenna for different values. (a) S-parameter for different L_1 (b) S-parameter for different L_3.

C. Performance of the antenna pair

The simulated results of the final proposed F-type antenna pair are presented in Fig. 4 (a)-(c), respectively. The S-parameter is shown in Fig. 4 (a). The reflection coefficients of both antennas are better than −10 dB across the desired sub-6 GHz band (4.8-5 GHz). Owing to the layout of the antenna elements being orthogonal to each other, the antenna elements are orthogonally polarized and can only sense the weak signal sent by each other. Therefore, an excellent isolation level is achieved: better than 17 dB across the operation band.

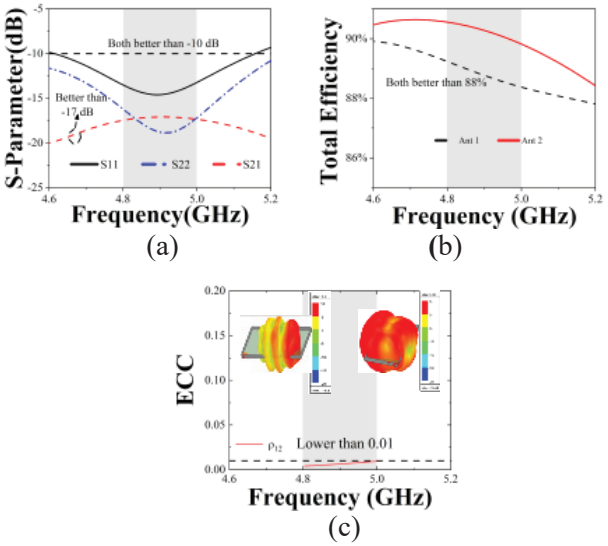

Fig. 4. Simulated performance of the dual antenna pair. (a) S-parameters. (b) Total efficiency. (c) ECC. Inserts: realized gain patterns at 4.9 GHz.

Figure 4 (b) shows the TE of the antenna pair. Across the operation band, the efficiency ranges of Ant 1 and Ant 2 are both better than 88%, which achieved greatly high.

Figure 4 (c) shows the simulated ECC, which is the dot product of the two antennas' complex radiation patterns. ECC is also a measurement of how tightly coupled antenna elements are, and it is calculated by ANSYS HFSS simulation software. The acceptable ECC criterion for MIMO antenna is less than 0.5. The simulated ECC is less than 0.01 across the operation band, indicating that the proposed antenna pair is with excellent diversity performance. Realized radiation patterns at 4.9 GHz of the two antennas are shown in the insets. Benefiting from orthogonal polarization, the main lobes of the two patterns are nearly orthogonal: Ant 1's main lobe points to +x, −y-direction; while Ant 2's main beam points to –x-direction. Therefore, an extremely low ECC is achieved.

The resonance mechanism is derived from the one-half wavelength working mode realized by the folding of the monopole arm. Figure 5 (a) shows the current distribution when port 1 is excited and port 2 terminal is terminated to 50 Ω. The upper and lower arms of the F-type monopole are used to generate resonance at 4.9 GHz, and the electric length can be observed to be about one-half wavelength. Other parts are used to complete impedance matching. Figure 5 (b) shows the electric field distribution of the antenna pair. When port 1 is excited, little current is registered on port 2, which is also the reason for the high isolation between antennas.

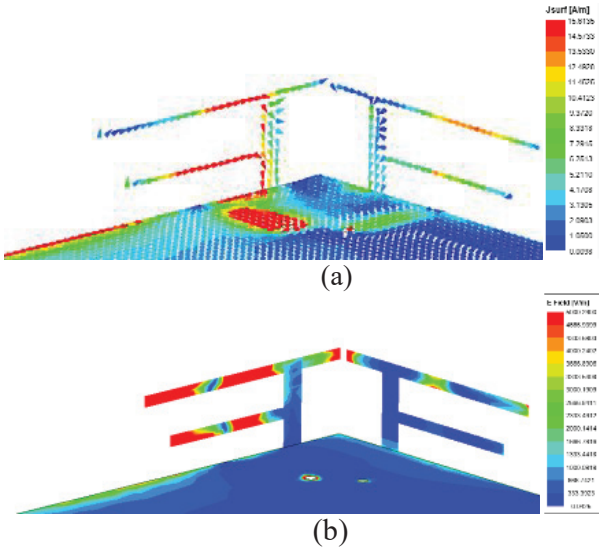

Fig. 5. Field distributions at 4.9 GHz. (a) Vector current distribution, (b) Mag E-field distribution.

III. EIGHT-PORT ANTENNA

A. Eight-port antenna performance

The last part effectively verifies the feasibility of the antenna pair. On the above basis, the 8×8 MIMO antenna system is constructed by placing four reciprocally symmetric F-type monopole antenna pairs at four diagonal of the smartphone, and grounded slots on short sides to improve isolation, as shown in Fig. 6 (a). An FR-4 substrate is employed as the main board of the smartphone. A metal ground plane is printed at the back side of the FR-4 substrate. Four FR-4 substrates are vertically placed around the ground plane to imitate the rim of the smartphone. A prototype was fabricated to demonstrate the feasibility of the proposed 8×8, MIMO antenna in the experiment, and its side, front and back photographs are depicted in Fig. 6 (b). Each antenna element is fed by a 50Ω microstrip feed line that is directly connected to a 50Ω Sub-Miniature-A (SMA) connector via the system ground.

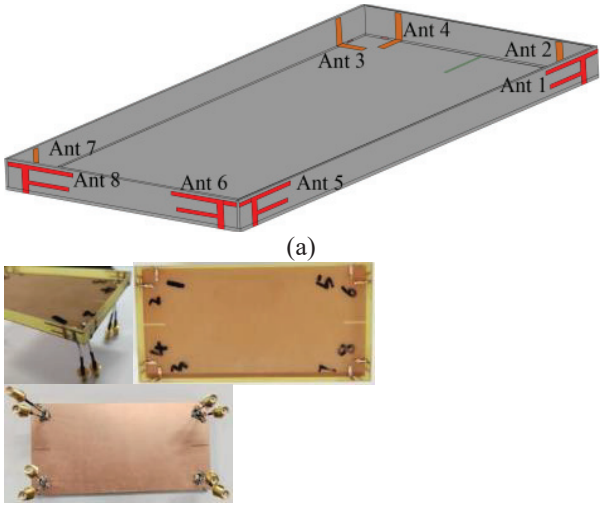

Fig. 6. (a) Simulated, (b) Prototyped photographs of 8×8 MIMO antenna.

Before forming the eight-port antenna, we made some improvements when forming the four-port antenna. As shown in Fig. 7, when there is no slot on the ground, the isolation between the two antenna pairs on the short side is low as shown in Fig. 7 (a). When we etched the appropriate grounded slot on the short side of the ground, the isolation dropped to 16 dB and showed better performance.

In the eight-port MIMO antenna, as shown in Fig. 8, it can also be seen from the three-dimensional (3-D) patterns that there is a pattern diversity phenomenon when port 1, port 2, port 3, and port 4 are excited respectively (the radiation patterns of the remaining four antennas are symmetrical with above ports due to symmetry). When port 1 or port 3 is excited, the radiation direction is the − x direction, and when port 2 or port 4 is excited, the radiation direction is the +x and +z direction. The maximum radiation direction of each antenna unit does not overlap. The radiation direction is different when the antenna is excited separately, and this further illustrates the high

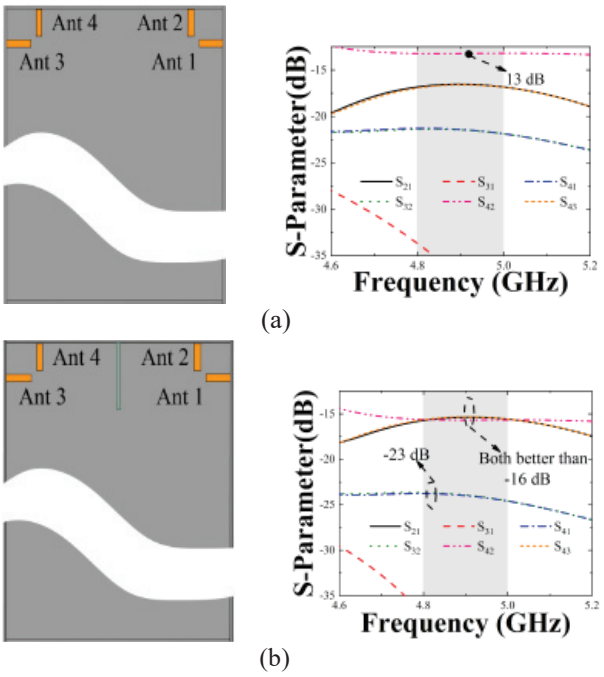

Fig. 7. Isolation performance of the four-port antenna structure (a) Without grounded slot, (b) With grounded slot.

isolation performance. In addition, the two-dimensional (2-D) radiation patterns of the four ports at 4.9 GHz are also shown in Fig. 8, the maximum gains of the four ports point in different directions, which also can explain the good isolation and low ECC.

In this section, the performance of the proposed eight-port MIMO antenna is also analyzed and the measured results are compared to the simulated ones. Figure 9 is the test procedure for the antenna prototype using the Agilent E5071C vector network measurement analyzer. Figure 10 shows the simulated and measured results respectively.

As the structure is symmetrical in terms of placement of the orthogonal pairs, only port 1, port 2, port 3, and port 4 are discussed in this section. The results for the S-parameter in relation to port 5–port 8 are omitted. Figure 10 (a) shows the simulated and measured $|S_{ii}|$ for port 1, port 2, port 3, and port 4. A resonant response is achieved at 4.9 GHz. Although some slight discrepancies can be observed due to minor production and welding errors, the measured results agree with the simulated ones covering well the bands of interest. In Fig. 10 (b), the measured $|S_{ij}|$ is compared to the simulated one. The worst $|S_{ij}|$ is less than 16 dB by connecting the orthogonal antennas with an NL and etching grounded slots between antenna pairs. Since the matching degree of test data in Fig. 10 (a) is worse than simulation data,

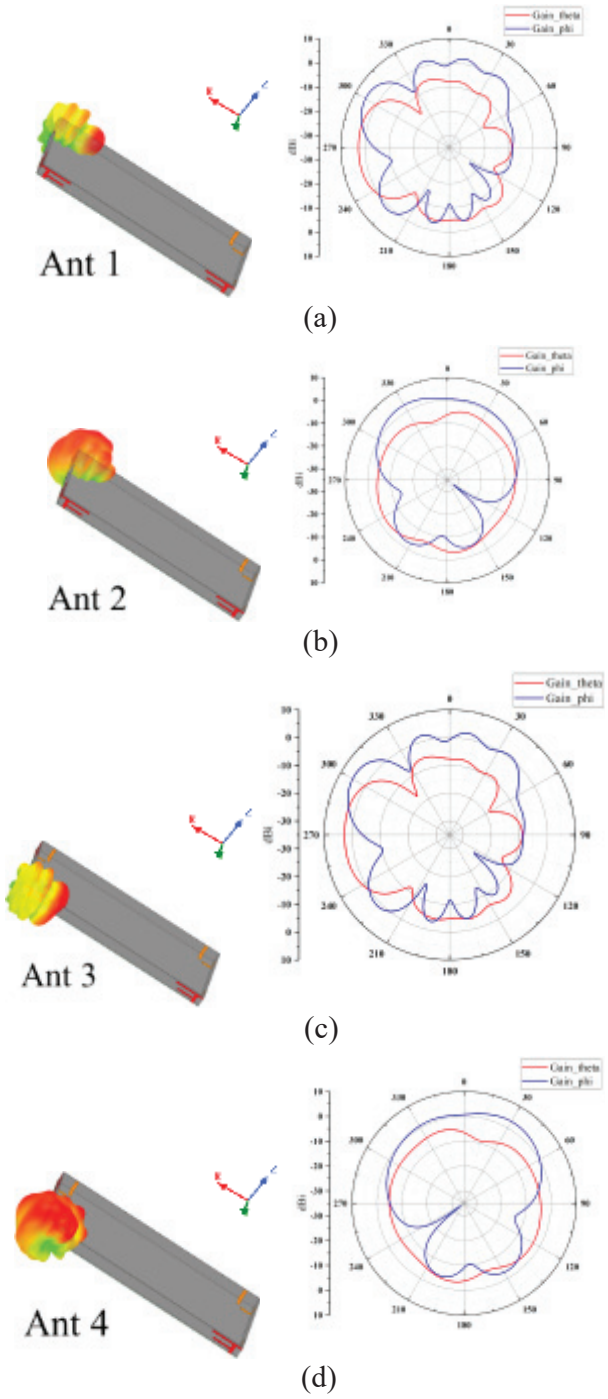

Fig. 8. 3-D and 2-D radiation patterns at 4.9 GHz from (a) Port 1, 2-D pattern in *xoz* plane, (b) Port 2, 2-D pattern in *yoz* plane, (c) Port 3, 2-D pattern in *xoz* plane, (d) Port 4, 2-D pattern in *yoz* plane.

the test data is better than the simulation data for isolation performance, which is at the expense of resonant characteristics.

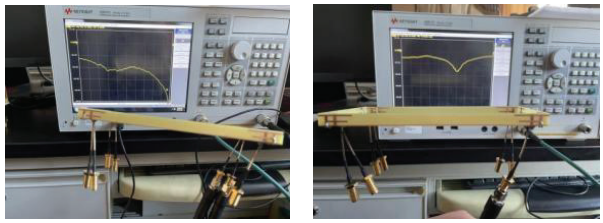

(a) (b)

Fig. 9. Photos of the test procedure. (a) Single-port. (b) Dual-port.

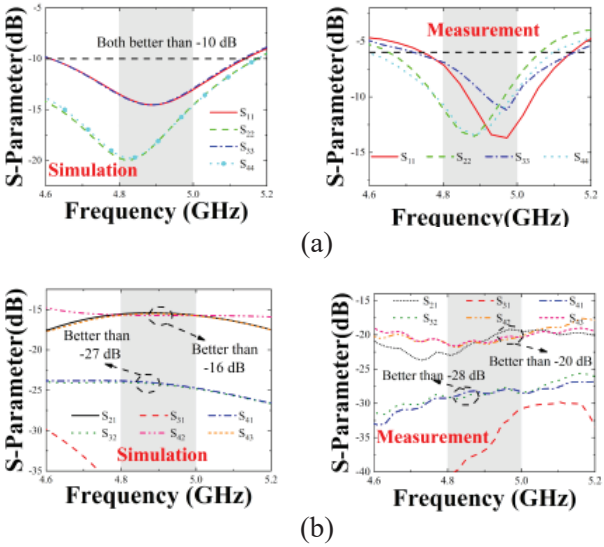

Fig. 10. Simulated and measured results of the eight-antenna MIMO array (a) reflection coefficient, (b) isolation.

B. MIMO performance

This part gives the MIMO performance index of this design from the TE and ECC.

The TE of port 1, port 2, port 3 and port 4 in eight-port MIMO antenna are shown in Fig. 11 (a). The total efficiency of antenna 2 and antenna 4 is the same: 80% $\sim$ 83%, and the total efficiency of antenna 1 and antenna 3 is the same: 77.5% $\sim$ 79%. Overall, the total efficiency achieved by port 1, port 2, port 3, and port 4 is high and desirable.

Figure 11 (b) shows ECC curves between two pairs of antenna pairs. It can be seen from the figure that ECC between any two elements is less than 0.025, the smartphone antenna requires ECC of less than 0.5, so the proposed antenna in this paper meets the requirement.

Table 2 exhibits the comparison of the proposed antenna with the references. Compared to the references, it can draw a conclusion that the designed antenna performs better isolation (better than 16 dB), excellent ECC (low than 0.025), and good total efficiency (high than

Table 2: Contrast of the referenced and proposed

Ref	Decoupling Method	Working Band (GHz)	Isolation (dB)	TE (%)	ECC	Complexity
[1]	Distance optimization	3.4 – 3.8 ($-6dB$)	<-10	> 42	< 0.1	Simple
[2]	LC tank	0.6 – 0.96 1.7 – 2.69 3.3 – 4.2 ($-6dB$)	<-10	> 42	< 0.4	Complex
[4]	Distance optimization	3.3 – 6 ($-6dB$)	< -11	> 40	< 0.12	Simple
[6]	Orthogonal polarization	3.4 – 3.6 ($-6dB$)	< -17	> 49	< 0.06	Medium
[7]	Orthogonal Polarization & NL	3.1 – 3.8 4.8-6 ($-10dB$)	< -10	> 60	< 0.06	Simple
[8]	DGS & NL	3.3 – 3.6 ($-6dB$)	¡-15	> 45	< 0.15	Simple
[9]	DGS	3.3 – 6 ($-6dB$)	< -18	> 40	< 0.05	Simple
[14]	Asymmetrically Mirrored	3.4 – 3.6 ($-6dB$)	< -12	> 40	< 0.1	Medium
[18]	Self-decoupled	3.3 – 4.2 ($-6dB$)	< -10.5	> 63.1	< 0.2	Medium
[20]	Self-decoupled	3.4 – 3.6 ($-6dB$)	<-16	> 38.75	< 0.042	Complex
[22]	Shorting Stub	3.3 – 7.5 ($-6dB$)	<-16	> 50	< 0.05	Medium
Proposed	Orthogonal Polarization	4.7 – 5.1 ($-10dB$)	< -16	> 77.5	< 0.025	Simple

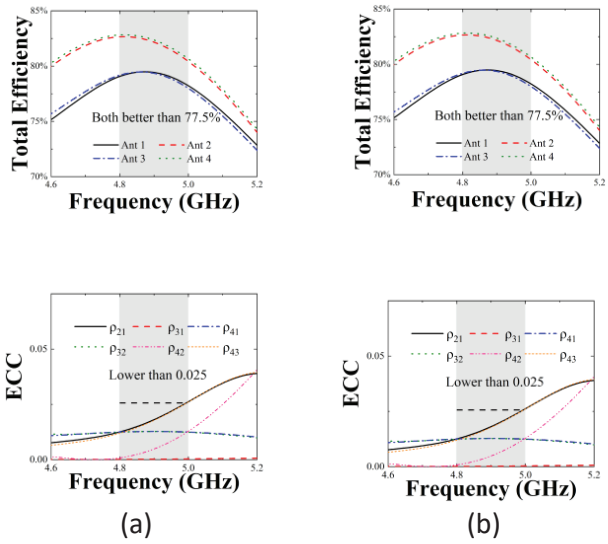

Fig. 11. (a) Total efficiency, (b) ECC.

77.5%). In addition, due to print on the corner of the smartphone border, the designed antenna leaves much space for other types of antennas and is an eligible candidate for a 5G full-screen smartphone.

IV. CONCLUSION

In this letter, a new design of an eight-port diagonal MIMO antenna with a compact size and simple structure

is designed to operate in 4.8-5 GHz for 5G smartphone applications. Isolation between the orthogonal antenna elements better than −16 dB and it is improved due to the addition of an NL and grounded slot. A good ECC of less than 0.025 is obtained and total efficiency is better than 77.5%.

ACKNOWLEDGMENT

The authors extend appreciation to the support of the National Natural Science Foundation of China (Grant No. 51965047), the Natural Science Foundation of Inner Mongolia (Grant No. 2021MS06012), and the Key Scientific and Technological Project of Inner Mongolia (Grant No. 2020GG0185) for this project.

REFERENCES

[1] K. L. Wong and J. Y. Lu, "10-antenna array in the smartphone for 3.6-GHz," *Microwave Opt. Technol. Lett*., vol. 57, pp. 1699-1704, 2015.

[2] K. L. Wong, H. J. Chang, and W. Y. Li, "Integrated triple-wideband triple-inverted-F antenna covering 617-960/1710-2690/3300-4200 MHz for 4G/5G communications in the smartphone," *Microwave and Optical Technology Letters,* vol. 60, no. 9, pp. 2091-2096, 2018.

[3] Q. Chen, H. Lin, J. Wang, L. Ge, Y. Li, T. Pei, and C. -Y. -D. Sim, "Single ring slot-based antennas for metal-rimmed 4G/5G smartphones," *IEEE Transactions on Antennas and Propagation,* vol. 67, no. 3, pp. 1476-1487, 2019.

[4] X. Zhang, Y. Li, W. Wang, and W. Shen, "Ultra-wideband 8-Port MIMO antenna array for 5G metal-frame smartphones," *IEEE Access,* vol. 7, pp. 72273-72282, 2019.

[5] A. Diallo, C. Luxey, P. Le Thuc, R. Staraj, and G. Kossiavas, "Study and reduction of the mutual coupling between two mobile phone PIFAs operating in the DCS1800 and UMTS bands," *IEEE Transactions on Antennas and Propagation,* vol. 54, no. 11, pp. 3063-3074, 2006.

[6] L. Sun, H. Feng, Y. Li, and Z. Zhang, "Compact 5G MIMO mobile phone antennas with tightly arranged orthogonal-mode pairs," *IEEE Transactions on Antennas and Propagation,* vol. 66, no. 11, pp. 6364-6369, 2018.

[7] D. Serghiou, M. Khalily, V. Singh, A. Araghi, and R. Tafazolli, "Sub-6 GHz dual-band 8 × 8 MIMO antenna for 5G smartphones," *IEEE Antennas and Wireless Propagation Letters,* vol. 19, no. 9, pp. 1546-1550, 2020.

[8] W. Jiang, B. Liu, Y. Cui, and W. Hu, "High-isolation eight-element MIMO array for 5G smartphone applications," *IEEE Access,* vol. 7, pp. 34104-34112, 2019.

[9] X. T. Yuan, W. He, K. D. Hong, C. Z. Han, Z. Chen, and T. Yuan, "Ultra-wideband MIMO antenna system with high element-isolation for 5G smartphone application," *IEEE Access,* vol. 8, pp. 56281-56289, 2020.

[10] X. T. Yuan, X. J. Wu, Z. Chen, C. Z. Han, X. Zhang, and T. Yuan, "Wideband 8-antenna array with high isolation for Sub-6 GHz MIMO applications," *2020 9th Asia-Pacific Conference on Antennas and Propagation (APCAP)*, PP. 1-2, 2020.

[11] Y. Hei, J. He, and W. Li, "Wideband decoupled 8-element MIMO antenna for 5G mobile terminal applications," *IEEE Antennas and Wireless Propagation Letters,* vol. 20, no. 8, pp. 1448-1452, 2021.

[12] W. Jiang, Y. Cui, B. Liu, W. Hu, and Y. Xi, "A dual-band MIMO antenna with enhanced isolation for 5G smartphone applications," *IEEE Access,* vol. 7, pp. 112554-112563, 2019.

[13] Z. Ren, A. Zhao, and S. Wu, "MIMO antenna with compact decoupled antenna pairs for 5G mobile terminals," *IEEE Antennas and Wireless Propagation Letters,* vol. 18, no. 7, pp. 1367-1371, 2019.

[14] K. L. Wong, C. Y. Tsai, and J. Y. Lu, "Two asymmetrically mirrored gap-coupled loop antennas as a compact building block for eight-antenna MIMO array in the future smartphone," *IEEE Transactions on Antennas and Propagation,* vol. 65, no. 4, pp. 1765-1778, 2017.

[15] K. L. Wong, Y. H. Chen, and W. Y. Li, "Conjoined ultra-wideband (2,300-6,000 MHz) dual antennas for LTE HB/WiFi/5G multi-input multi-output operation in the fifth-generation tablet device," *Microwave and Optical Technology Letters,* vol. 61, no. 8, pp. 1958-1963, 2019.

[16] A. Zhao and Z. Ren, "Size reduction of self-isolated MIMO antenna system for 5G mobile phone applications," *IEEE Antennas and Wireless Propagation Letters,* vol. 18, no. 1, pp. 152-156, 2019.

[17] F. Ghawbar, A. S. Jumadi, H. A. Majid, F. A. Saparudin, A. S. A. Ghafar, and B. A. F Esmail, "Compact self-isolated MIMO antenna system with low mutual coupling for 5G mobile applications," *2020 IEEE Student Conference on Research and Development (SCOReD)*, pp. 200-205, 2020.

[18] L. Sun, Y. Li, Z. Zhang, and H. Wang, "Self-decoupled MIMO antenna pair with shared radiator for 5G smartphones," *IEEE Transactions on Antennas and Propagation,* vol. 68, no. 5, pp. 3423-3432, 2020.

[19] L. Sun, Y. Li, and Z. Zhang, "Wideband decoupling of integrated slot antenna pairs for 5G smartphones," *IEEE Transactions on Antennas and Propagation,* vol. 69, no. 4, pp. 2386-2391, 2021.

[20] B. Yang, Y. Xu, F. Lu, R. Li, L. Zhang, and Y. Liu, "High-isolation dual-port antenna with self-decoupling characteristics for 5G smartphone applications," *International Journal of RF and Microwave Computer-Aided Engineering,* vol. 31, no. 8, 2021.

[21] L. Y. Nie, X. Q. Lin, S. Xiang, B. Wang, L. Xiao, and J. Y. Ye, "High-isolation Two-port UWB antenna based on shared structure," *IEEE Transactions on Antennas and Propagation,* vol. 68, no. 12, pp. 8186-8191, 2020.

[22] X. T. Yuan, Z. Chen, T. Gu, and T. Yuan, "A wideband PIFA-pair-based MIMO antenna for 5G smartphones," *IEEE Antennas and Wireless Propagation Letters,* vol. 20, no. 3, pp. 371-375, 2021.

[23] L. Chang, Y. Yu, K. Wei, and H. Wang, "Orthogonally polarized dual antenna pair with high isolation and balanced high performance for 5G MIMO smartphone," *IEEE Transactions on Antennas and Propagation,* vol. 68, no. 5, pp. 3487-3495, 2020.

Rui Shao received a bachelor's degree in communication engineering from Shandong University of Technology,Zibo, China, in July 2020. From September 2020, she studies for the master's degree of Information and Communication Engineering at Inner Mongolia University, Hohhot, China. Her research interests include research and design of 5G high isolation MIMO antenna.

Junlin Wang received a doctor's degree in engineering in Instrument Science and Technology of Zhongbei University. He is currently working in the College of Electronic Information Engineering, Inner Mongolia University, Hohhot, China. His research interests include micro-nano RF devices (antennas, filters, couplers, etc.) and metamaterial antennas.

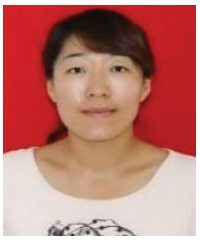

Xin Wang received a Ph.D. in engineering in Instrument Science and technology from Zhong-bei University, she is currently working in the College of Electronic Information Engineering, Inner Mongolia University, Hohhot. China. Her research interests include micro-nano RF devices (antennas, filters, couplers, etc.) and metamaterial antenna.

Yonghao Wang received his bachelor's degree in Communication Engineering from Shandong University of Science and Technology in Qingdao, China in July 2020. Since September 2020, he is studying for a master's degree in Electronic and Communication Engineering at Inner Mongolia University, Hohhot, China. His research interests include research and design of 5G miniaturized high isolation dual-band MIMO antennas for mobile phones.

Quad-band Compact MIMO Antennas for 5G Mobile Communications

Asmaa E. Farahat and Khalid F. A. Hussein

Microwave Engineering Department
Electronics Research Institute, Cairo, 11843, Egypt
asmaa@eri.sci.eg, fkhalid@eri.sci.eg

Abstract – Three types of quad-band millimetric-wave two-port MIMO antenna systems are proposed for the forthcoming generations of mobile handsets. A novel printed antenna is introduced to be the single element of the proposed MIMO antennas. It is shown that the proposed MIMO antennas are capable of producing both spatial and polarization diversities that enhance the performance of mobile communications. Two configurations of co-polarized two-port MIMO antennas are proposed to provide spatial diversity, whereas a cross-polarized two-port MIMO antenna is proposed to produce polarization diversity. It is shown that all the proposed MIMO antennas can operate efficiently over the four frequency bands centered at 28, 43, 52, and 57 GHz. Prototypes are fabricated for the proposed MIMO antennas for the sake of experimental evaluation. The measurements agree with the simulation results showing high performance of the proposed types of MIMO antennas including the impedance matching, radiation patterns, envelop correlation coefficient, and diversity gain. Both the experimental and simulation results show that the achieved bandwidths, at the four operational frequency bands, are 0.6, 0.6, 1.8, and 1.5 GHz, respectively. Also, the radiation efficiencies calculated at the four operational frequencies are 86.5%, 87.5%, 89.2%, and 90.0%, respectively. The dimensions and the results concerning the performance of the proposed MIMO antennas are compared to other designs for MIMO antennas available in some recently published work.

Index Terms – 5G, MIMO antennas, quad-band.

I. INTRODUCTION

One of the essential demands for future generations of mobile communications is the capability of mobile handsets to transfer data at very high speeds. A mobile handset antenna should have a compact profile and simple structure [1, 2]. To meet the standards of long-term-evolution (LTE) and fifth-generation (5G) mobile communications [3] the handheld device's antenna should provide broadband operation, high data rate, and low power consumption. This recommends that a mobile handset antenna should be able to operate in the range of mm-wave of the electromagnetic spectrum to support the required data rates for future applications. Moreover, due to size limitations, it is recommended that a mobile handset antenna is able to operate efficiently at multiple frequency bands in the mm-wave spectrum to support the applications of the forthcoming mobile generations [4, 5]. In various situations, the antenna structure may be complicated as those having a three-dimensional shape to operate efficiently in a single frequency band and to perform some function in special applications [6, 7] and may include layers with high electromagnetic absorbance [8] to produce radiation patterns of the desired shape. However, for mobile handsets, due to size and weight limitations, it is preferable to have a planar antenna of simple-structure, multi-band operation, and omnidirectional radiation patterns.

The design of MIMO antenna systems for operation in mobile handsets for the next generations of mobile communications faces many challenges. First of all, the MIMO antenna on a handset should be miniaturized due to space limitations. The second challenge is to achieve high isolation between the antenna elements in spite of the small area available for the antenna on the mobile handset. The third challenge is to have the MIMO antenna operational at multiple frequencies with enough wideband at each frequency (multiple-band operation). The fourth challenge is to produce the required shape of the radiation patterns over the operational frequency bands. Also, it may be required from a MIMO antenna to provide many types of diversity such as spatial, polarization, and pattern diversities.

Various types of MIMO antenna systems for 5G mobile handsets, recently, have been designed in a lot of research articles. For example, in [9], a compact microstrip line fed dual-band printed two-port and four-port MIMO antennas are proposed for wireless communications. In [10], a seven-port MIMO antenna system is proposed as a candidate for future mobile communications to operate at 37.5 GHz. A cross-polarized four-port dual-band MIMO antenna array is proposed in [11]

Submitted On: March 25, 2022
Accepted On: September 20, 2022

https://doi.org/10.13052/2022.ACES.J.370806

to operate at 28 and 37.5 GHz for 5G communications. The work of [12] proposes a dual-band two-port MIMO antenna to operate at 28 and 38 GHz for 5G mobile applications. In [13], a planar dual-band (27/39 GHz) millimeter-wave two-port MIMO antenna is suggested for 5G mobile communications. The work of [14] introduces a compact four-port MIMO antenna with high isolation and a single wideband for mm-Wave Applications. In [15] and [16], quad-band ($28/45/51/56\ GHz$) two-port and four-port MIMO antenna systems are proposed for 5G mobile communications. The work of [17] proposes a dual-band (28/38 GHz) four-port MIMO antenna system for 5G mobile communications for efficient Estimation of the directional of arrival in noisy communication channels. In [18] and [19], dual-Band (28/38 GHz) cross-polarized four-port MIMO antenna systems composed of high-gain Yagi-Uda antenna with corrugated radiators and enhanced reflectors are proposed to provide spatial, polarization, and pattern diversities for 5G mobile communications.

In this work, compact-size quad-band two-port MIMO antenna systems are proposed to operate in the millimetric-wave bands (28/43/52/57 GHz) for the forthcoming generations of mobile communications. The proposed MIMO antennas provide various types of diversity to enhance the performance of mobile communication systems. Two types of co-polarized two-port MIMO antenna systems with high isolation among the antenna elements are proposed to provide spatial polarization. Also, a cross-polarized two-port MIMO antenna is proposed to provide polarization diversity.

II. DESIGN OF THE QUAD-BAND SINGLE-ELEMENT ANTENNA

The geometry of the patch antenna proposed to construct the MIMO antenna systems is demonstrated in Fig. 1. It is designed to be printed on Rogers RO3003 substrate with $W \times L = 8 \times 18\ mm^2$ and 0.25 mm thickness, dielectric constant $\varepsilon_r = 3$, and loss tangent $tantan\ d = 0.001$. The substrate has a solid ground plane to reduce the back radiation from the antenna. The printed antenna is fed through a 50Ω microstrip line of length $L_f = 10\ mm$. The width of the microstrip line is set to $W_f = 0.63\ mm$ to achieve its characteristic impedance equal to 50Ω. An inset feed is used to match the antenna impedance to 50Ω. The inset length is $L_i = 1.23\ mm$ and the width of each slot made on the sides of the feeding line for the inset feed is $W_i = 0.3\ mm$. The remaining dimensions are listed in Table 1.

In the electromagnetic simulations, for a substrate of size 8 mm×18 mm and height 0.25 mm, the simulation (execution) time for each of the studied cases to reach the final design is approximately 10 minutes with accuracy −40 dB using the time domain solver on a core I7-3.6 GHz processor, 16G RAM, and 64-bit operating system. Hexahedral meshing is used to model the design with 15 cells/wavelength for all simulations.

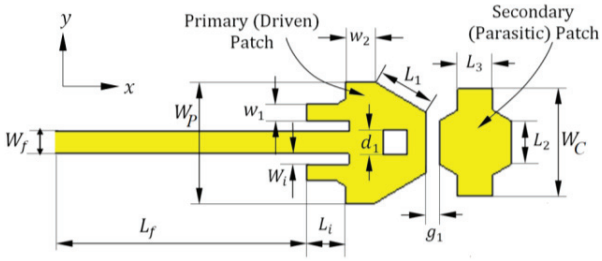

(a)

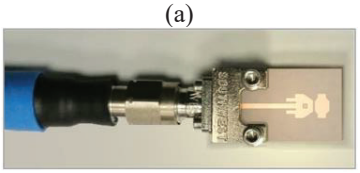

(b)

Fig. 1. The quad-band millimetric-wave antenna proposed for MIMO antenna systems. (a) Geometry of the printed antenna. (b) Fabricated antenna prototype is connected to end launcher and coaxial cable for measurements.

Table 1: Dimensions of the quad-band printed antenna proposed for the MIMO antenna system

Dimension	L_1	L_2	L_3	w_i	w_1	w_2	d_1	g_1	W_P	W_C
Value (mm)	1.7	1.2	1	0.3	0.45	0.85	0.7	0.38	3.4	3.0

The millimetric-wave antenna with the geometry shown in Fig. 1 and the dimensional parameters listed in Table 1 is used to construct various configurations of two-port MIMO antenna systems with various types of diversity proposed for the handsets of the forthcoming generations of mobile communications. Accordingly, it is important to investigate the characteristics of this antenna through electromagnetic simulation and laboratory measurements. Figure 2 presents the dependence of the scattering parameter $|S_{11}|$ at the antenna port as obtained by both simulation and experimental measurements. It is shown that the antenna has four operational millimetric-wave frequency bands at which the antenna is matched to 50Ω feeder and, hence, the return loss is very low. The operational frequency bands are 28, 43, 52, and 57 GHz. Fortunately the four frequencies are distributed over very important range of the millimetric-wave which makes this antenna a promising candidate for future mobile applications. Both the simu-

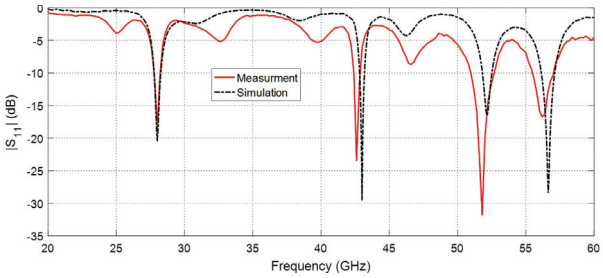

Fig. 2. Dependence of $|S_{11}|$ on the frequency for the proposed quad-band patch antenna.

lation results and the measurements come in good agreement with each other.

The elevation radiation patterns in the planes $\phi = 0^{\circ}$ and $\phi = 90^{\circ}$ at the four frequencies 28, 43, 52, and 57 GHz are presented in Figs. 3, 4, 5, and 6, respectively. The experimental measurements show good agreement with the simulation results at all the operational frequencies of the proposed antenna.

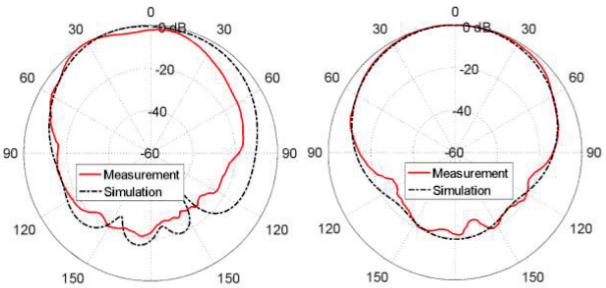

Fig. 3. Radiation patterns of the proposed quad-band patch antenna at 28 GHz in the planes (a) $\phi = 0^{\circ}$ and (b) $\phi = 90^{\circ}$.

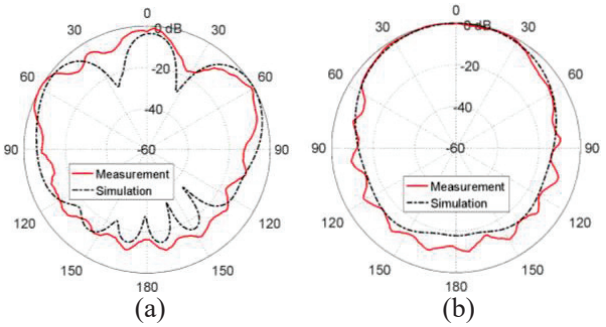

Fig. 4. Radiation patterns of the proposed quad-band patch antenna at 43 GHz in planes (a) $\phi = 0^{\circ}$ and (b) $\phi = 90^{\circ}$.

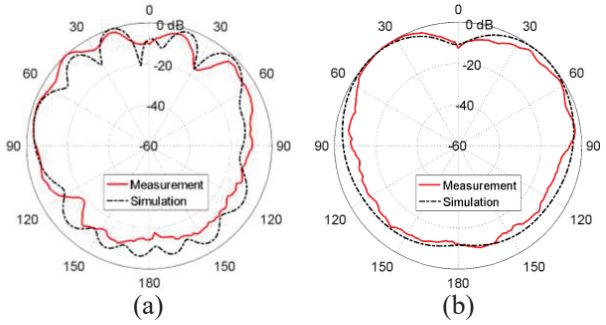

Fig. 5. Radiation patterns of the proposed quad-band patch antenna at 53 GHz in planes (a) $\phi = 0^{\circ}$ and (b) $\phi = 90^{\circ}$.

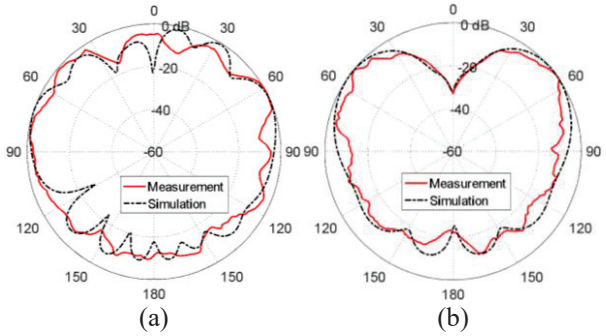

Fig. 6. Radiation patterns of the proposed quad-band patch antenna at 56.5 GHz in planes (a) $\phi = 0^{\circ}$ and (b) $\phi = 90^{\circ}$.

III. TWO-PORT MIMO ANTENNAS FOR QUAD-BAND OPERATION

Printed MIMO antennas are recommended for future generations of mobile handsets to enhance the performance of the mobile communication systems by providing various types of antenna diversity such as spatial, polarization, and pattern diversity. Due to space and power limitations in a mobile handset, two-port MIMO antennas are appropriate and may be the most suitable solution among the other MIMO antenna systems to provide the required types of diversity. The present section provides various designs of two-element MIMO antennas. The proposed MIMO antennas are fabricated and subjected to experimental evaluation. The simulation and experimental results are compared to each other for the confirmation of the obtained results.

A. Co-polarized two-port MIMO antennas for spatial diversity

Keeping large enough distance between two antennas of the same polarization on the mobile handset provides spatial diversity that can mitigate fading problems due to multipath propagation in wireless communication channels.

In the present section, three types of co-polarized two-port MIMO antennas using the single-element antenna shown in Fig. 1 are investigated theoretically and experimentally. Each of the three types of the proposed two-port MIMO antenna is described and its performance is investigated in the following subsections. In spite of being of almost equal performance, the three types have different dimensions and are proposed to provide a variety of solutions that can fit the available space on the electronic board of a specific mobile handset.

A.1. Design and fabrication of co-polarized two-port MIMO antennas

The patches of the first type of the proposed two-port MIMO antennas were arranged as shown in Fig. 7 (a). To reduce the mutual coupling, the two patch antennas were horizontally shifted from each other such that the space between their axes was 5 mm. However, the vertical separation between the two antennas was only 2 mm. For a more compact MIMO antenna, the patches of the second MIMO configuration were arranged face-to-face as shown in Fig. 7 (b). The patches of the third MIMO system were arranged side-by-side as shown in Fig. 8 (a). A prototype was fabricated for each type of the MIMO antenna systems as shown in Figs. 7 (c) and 8 (b), respectively, and connected to a coaxial feeder using coaxial end launchers for experimental assessment. It should be noted that the patch of all the proposed types of MIMO antennas were well-matched to the 50Ω feeder and, on the other hand, the feeding microstrip line was well-designed to have its characteristic impedance equal to 50Ω. Consequently, the length of the feeding microstrip lines could be variable without affecting antenna performance. For this reason, the length of the feeding line was not considered as a part of the antenna structure and, hence, the lengths of all the feeding lines are excluded from the antenna dimensions.

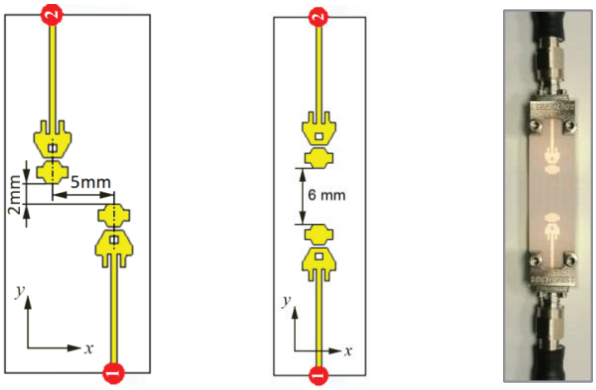

(a) (b) (c)

Fig. 7. Two types of two-port MIMO antenna system constructed as two elements of the quad-band patch element. (a) Model with shifted antennas. (b) Model with face-to-face arrangement. (c) Fabricated prototype connected to end launchers and coaxial cables for measurements.

A.2. Mutual coupling between the antenna elements and the diversity gain

The self and mutual S-parameters of the co-polarized two-port MIMO antenna systems whose designs are presented in Figs. 7 and 8 have their frequency dependencies as shown in Figs. 9 (a) and 9 (b), respectively. The results were obtained by electromagnetic simulation using the commercially available CST® simulator. When comparing the frequency dependencies of the self S-parameters of the two-port MIMO antennas to those presented in Fig. 2, for the single-element antenna, it is clear that the locations of the resonant frequencies (anti-peaks of $|S_{11}|$ and $|S_{22}|$ with the frequency) for the two configurations of MIMO antennas were almost identical to those of the single-element antenna. This indicates that the mutual coupling between the two antennas is very weak for the face-to-face as well as the side-by-side MIMO configurations. This is emphasized by the low magnitude of the mutual S-parameter, S_{21} over the entire frequency range (20–60 GHz) as shown in Fig. 9 for both two-port MIMO configurations. Microwave measurements are used to confirm the low mutual coupling between the antenna ports. The VNA of Rhode and Schwartz model ZVA67 is used to evaluate the reflection coefficients, S_{11} and S_{22}, and the mutual S-parameters, S_{21} and S_{12}, for the fabricated prototypes of the proposed MIMO antennas. The dependence of $|S_{21}|$ on the frequency over the range (20–60 GHz) obtained by the CST® simulator is compared to that obtained by experimental measurements as shown in Fig. 9. Both

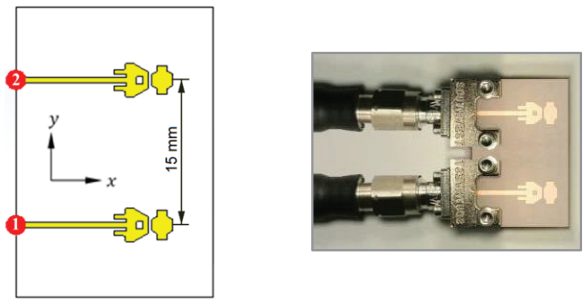

(a) (b)

Fig. 8. Two-port MIMO antenna system constructed as two elements of the quad-band patch arranged side-by-side. (a) Antenna model for simulation. (b) Fabricated prototype connected to end launchers and coaxial cables for measurements.

come in good agreement and confirm low mutual coupling between the antenna ports.

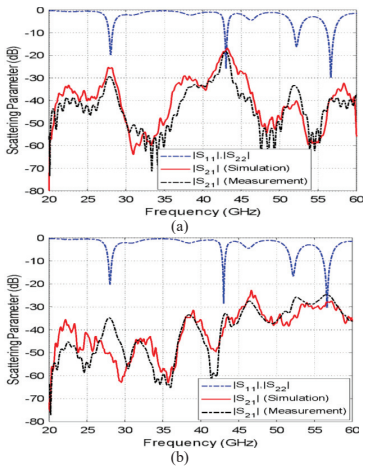

Fig. 9. Frequency dependence of the self and mutual S-parameters of the co-polarized two-port MIMO antenna systems. (b) Face-to-face configuration shown in Fig. 7. (a) Side-by-side configuration shown in Fig. 8.

A.3. Envelope correlation coefficient and diversity gain of the co-polarized two-port MIMO antenna

As a consequence of low mutual coupling and the distance between the two-ports of the co-polarized MIMO antennas, the ECC is very low over the entire frequency range (20-60 GHz) and is almost zero over the operational frequency bands (28, 43, 52, 57 GHz) as shown in Fig. 10 (a). The corresponding DG is almost 10 as shown in Fig. 10 (b).

A.4. Radiation patterns of co-polarized two-port MIMO antenna system

The radiation patterns of the co-polarized two-port MIMO antenna in the elevation planes $\phi = 0^\circ$ and $\phi = 90^\circ$ at the operational frequencies (28, 43, 52, 57 GHz) are presented in Figs. 11, 12, 13, and 14, respectively, for face-to-face configuration, and Figs. 15, 16, 17, and 18, respectively, for the side-by-side configuration, as obtained by simulation when the MIMO antenna is fed through each port alone. The corresponding values of the maximum gain are 7.1, 8.1, 7.7, and 8.6 dBi, respectively, for the face-to-face configuration, and 6.89, 7.9, 7.6, and 8.3 dBi, respectively, for the side-by-side configuration. The radiation patterns and the achieved gain values at the four operational frequencies seem to be appropriate for various wireless communications and mobile applications.

B. Two-port MIMO antennas for polarization diversity

The simplest form of cross-polarized MIMO antenna can be realized by combining pairs of antennas

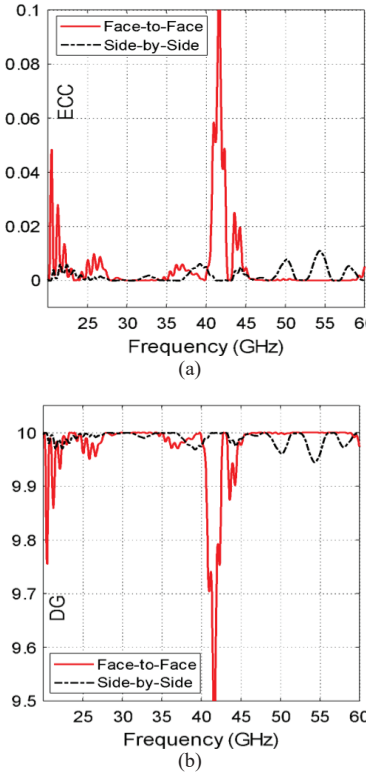

Fig. 10. Frequency dependence of the ECC and DG of the co-polarized two-port MIMO antenna systems with the two arrangements presented in Figs. 7 and 8.

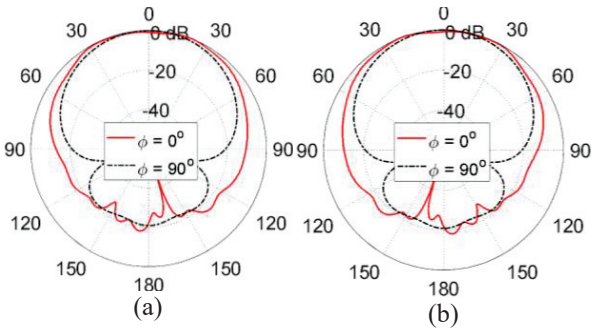

Fig. 11. Radiation patterns in the elevation planes for the co-polarized face-to-face two-port MIMO antenna system at 28 GHz when excited at (a) port 1, (b) port 2.

with orthogonal polarizations (i.e. horizontal/vertical, ± slant 45°, left-hand/Right-hand circular polarization, etc.). Such cross-polarized MIMO antenna systems are able to provide polarization diversity that enhances mobile communication performance.

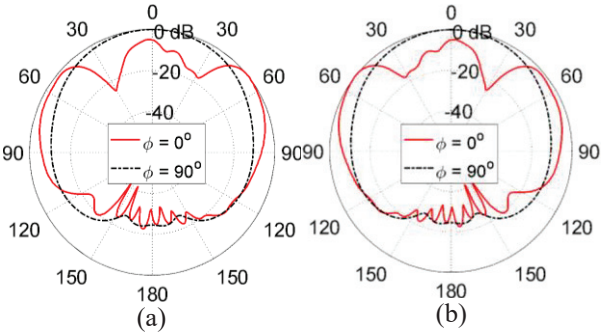

Fig. 12. Radiation patterns in the elevation planes for the co-polarized face-to-face two-port MIMO antenna system at 43 GHz when excited at (a) port 1, (b) port 2.

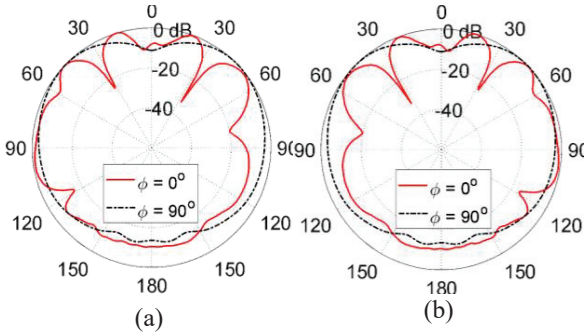

Fig. 13. Radiation patterns in the elevation planes for the co-polarized face-to-face two-port MIMO antenna system at 52 GHz when excited at (a) port 1, (b) port 2.

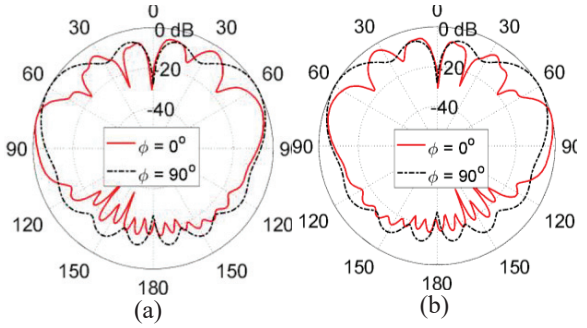

Fig. 14. Radiation patterns in the elevation planes for the co-polarized face-to-face two-port MIMO antenna system at 57 GHz when excited at (a) port 1, (b) port 2.

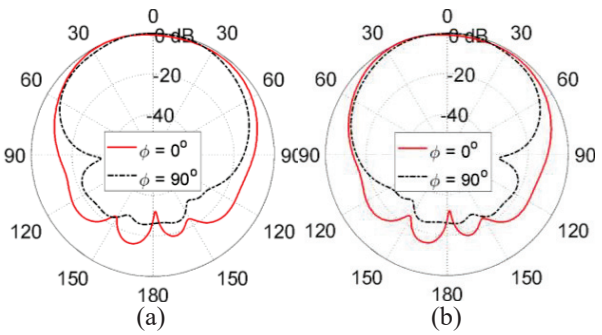

Fig. 15. Radiation patterns in the elevation planes for the co-polarized side-by-side two-port MIMO antenna system at 28 GHz when excited at (a) port, (b) port 2.

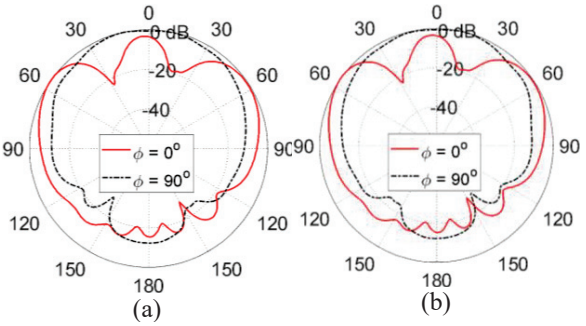

Fig. 16. Radiation patterns in the elevation planes for the co-polarized side-by-side two-port MIMO antenna system at 43 GHz when excited at (a) port, (b) port 2.

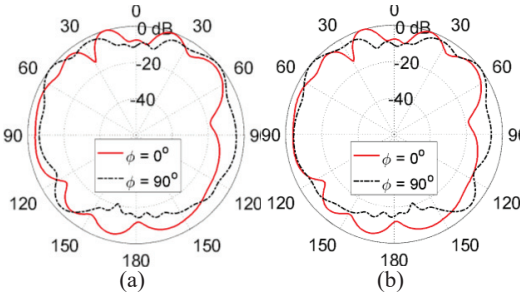

Fig. 17. Radiation patterns in the elevation planes for the co-polarized side-by-side two-port MIMO antenna system at 52 GHz when excited at (a) port, (b) port 2.

B.1. Design and fabrication of cross-polarized two-port MIMO antenna

A cross-polarized two-port MIMO antenna that produces two orthogonal polarizations when fed at port 1 and port 2 can be constructed as shown in Fig. 19. (a) using the single-Element antenna introduced in Section II. When this MIMO antenna is excited at port 1, the electric field in the far zone is *x*-oriented whereas the

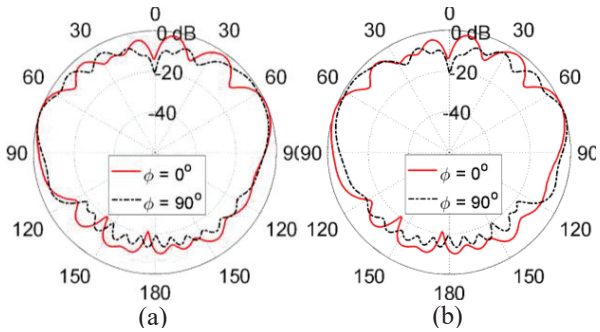

Fig. 18. Radiation patterns in the elevation planes for the co-polarized side-by-side two-port MIMO antenna system at 57 GHz when excited at (a) port, (b) port 2.

excitation at port 2 produces y-oriented electric field in the far zone.

B.2. Mutual coupling between the antenna elements

The self and mutual S-parameters of the cross-polarized two-port MIMO antenna system (presented in Fig. 19. (a)) have their frequency dependencies as shown in Fig. 19. (b). As obtained by simulation, the frequency dependence of $|S_{11}|$ of the cross-polarized two-port MIMO antenna is identical to that of $|S_{22}|$. It is clear that the minima of $|S_{11}|$ and $|S_{22}|$ with the frequency occur at almost the same resonant frequencies of the single-element antenna (See Fig. 5). This indicates that the mutual coupling between the two elements of

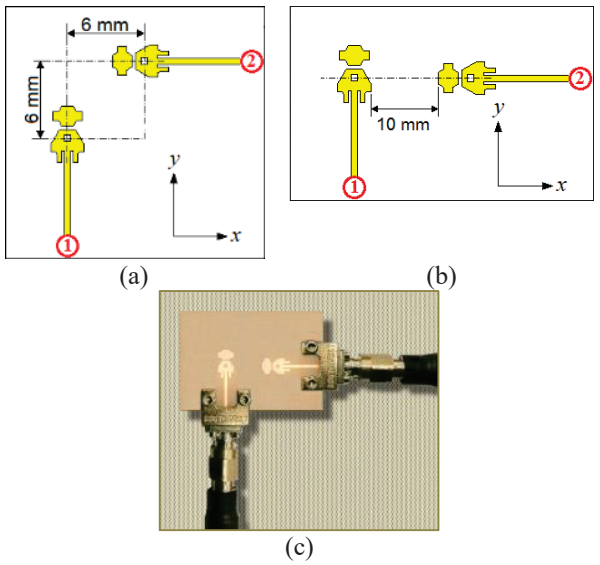

Fig. 19. (a). Cross-polarized two-port MIMO antenna system constructed as two orthogonally oriented elements of the quad-band patch. (a) Antenna model for simulation. (b) Fabricated prototype connected to end launchers and coaxial cables for measurements.

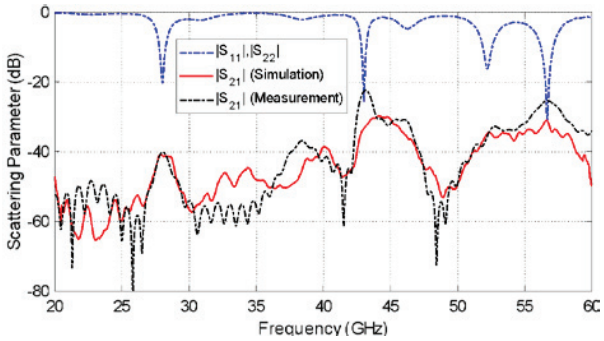

Fig. 19. (b). Frequency dependence of the self and mutual scattering parameters of the cross-polarized two-port MIMO antenna system presented in Fig. 15 (a).

the cross-polarized MIMO antenna is very weak. Also, the magnitude of the mutual scattering coefficient S_{21} is very low over the entire frequency range (20 - 60 GHz) as shown in Fig. 19. (a). The simulation results for the dependence of $|S_{21}|$ on the frequency over the range (20 - 60 GHz) are compared to those obtained by experimental measurements and showing good agreement, which emphasizes the low mutual coupling.

B.3. Envelope correlation coefficient and diversity gain of the cross-polarized two-port MIMO antenna

The dependencies of the ECC and the DG of the cross-polarized two-port MIMO antenna over the frequency range (20–60 GHz) are shown in Fig. 19. (b). Due to the orthogonal polarizations produced by the two antennas in addition to the separation between them, the ECC and, hence, the DG of the cross-polarized two-port MIMO antenna is better than those presented in Fig. 10 for the co-polarized two-port MIMO antennas of the two configurations described in Figs. 7 and 8.

B.4. Radiation patterns of cross-polarized two-port MIMO antenna system

The radiation patterns of the total radiated field at the frequencies 28, 43, 52, and 57 GHz are presented in Figs. 20, 21, 22, and 23, respectively in the orthogonal planes $\phi = 0^{\circ}$ and $\phi = 90^{\circ}$ when the cross-polarized two-port MIMO antenna is excited at each port individually. From the radiation patterns in the two orthogonal planes, it can be shown that the cross-polarized two-port MIMO antenna has omnidirectional radiation in the azimuth plane. This makes the antenna a promising candidate for mobile handset applications intended for the forthcoming generation of mobile communications.

For quantitative demonstration of the polarization diversity that can be provided by the cross-polarized two-port MIMO antenna proposed in the present work, the radiation patterns for the x-oriented and y-oriented components of the far electric field E_x and E_y, respectively, at

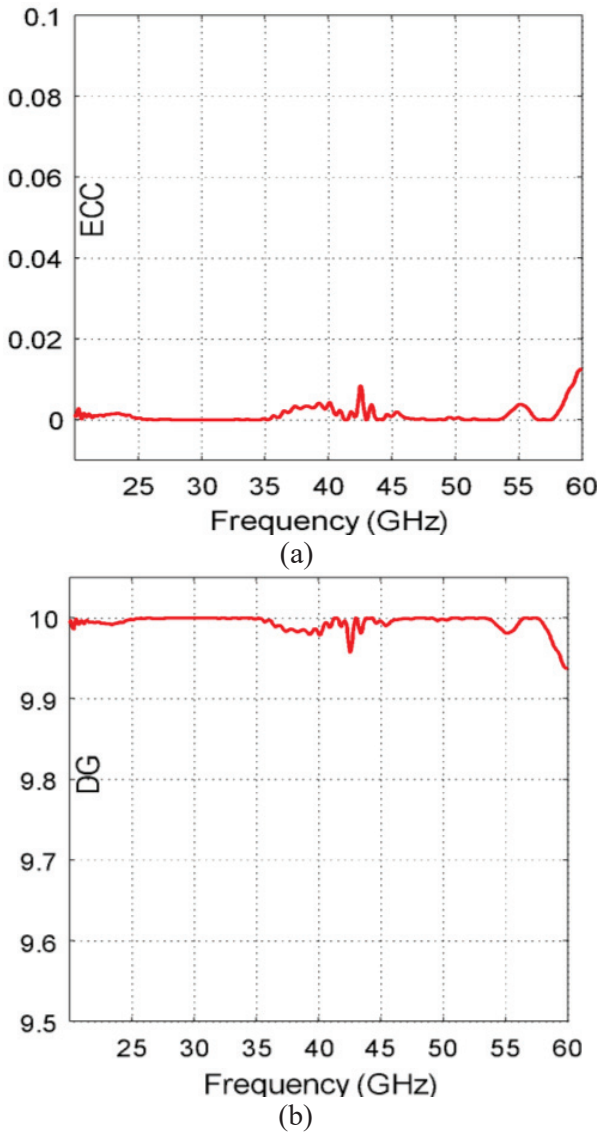

Fig. 20. Frequency dependence of the ECC and DG of the cross-polarized two-port MIMO antenna system presented in Fig. 19. (a).

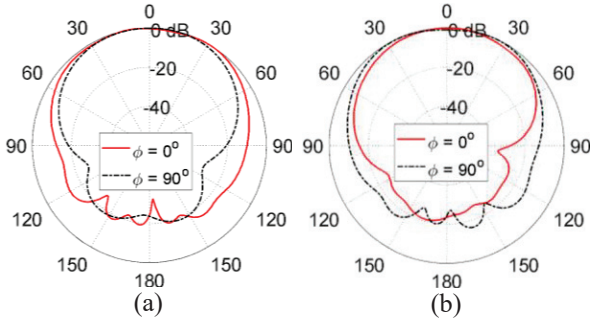

Fig. 21. Radiation patterns in the elevation planes for the cross-polarized two-port MIMO antenna system at 28GHz when excited at (a) port and (b) port 2.

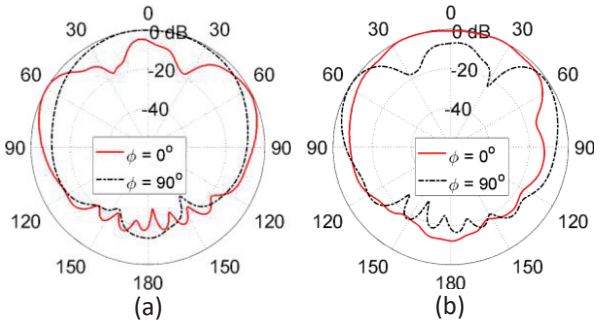

Fig. 22. Radiation patterns in the elevation planes for the cross-polarized two-port MIMO antenna system at 43 GHz when excited at (a) port 1 and (b) port 2.

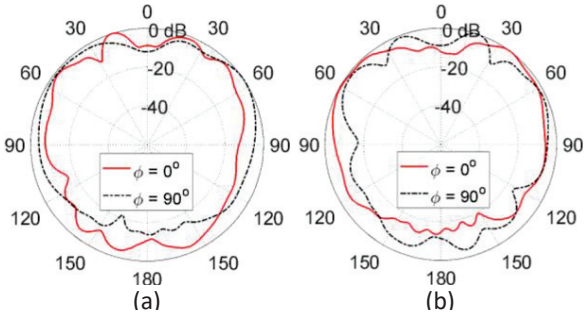

Fig. 23. Radiation patterns in the elevation planes for the cross-polarized two-port MIMO antenna system at 52 GHz when excited at (a) port and (b) port 2.

28 GHz are plotted as shown in Fig. 24 when the MIMO antenna is excited at each port alone. It is shown that the electric field in the far zone is dominated by vertical (y-oriented) component when MIMO antenna is excited at port 1 and is dominated by horizontal (x-oriented) component when the MIMO antenna is excited at port 2. Thus, the proposed cross-polarized two-port MIMO antenna provides the polarization diversity required for enhancing the communication system performance.

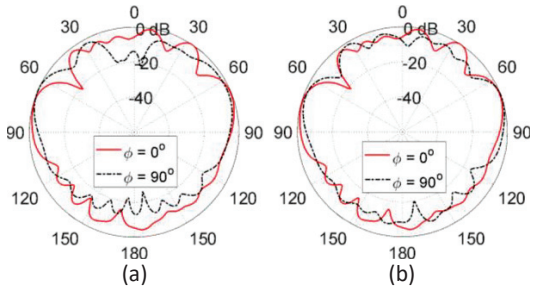

Fig. 24. Radiation patterns in the elevation planes for the cross-polarized two-port MIMO antenna system at 57 GHz when excited at (a) port 1 and (b) port 2.

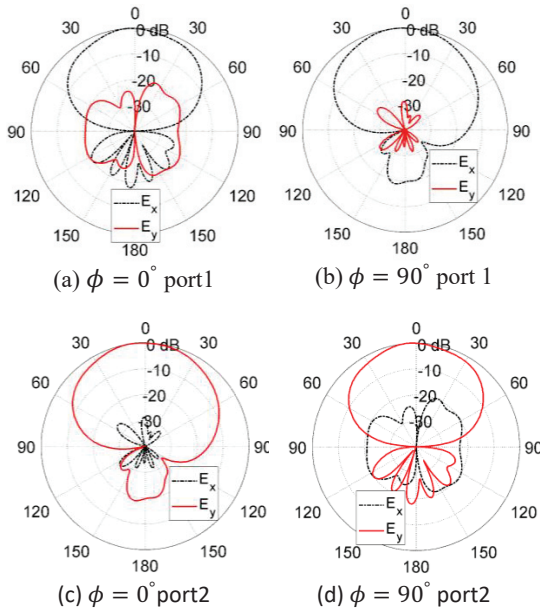

Fig. 25. The radiation patterns of the horizontally polarized (*x*-oriented) and vertically polarized (*y*-oriented) electric field radiated from the cross-polarized two-port MIMO antenna system at 28 GHz when the MIMO antenna is excited at each port alone.

IV. SUMMARY OF THE PROPOSED MIMO ANTENNA PERFORMANCE

A. Performance of the single-element antenna

A summary of some important performance measures of the proposed single-element antenna used to construct the proposed MIMO antenna systems at the four operational frequencies, is listed in Table 3.

B. Performance of the MIMO antennas

A comparative performance among some millimetric-wave MIMO antennas designed for mobile handsets that are available in some recent literature and the MIMO antennas proposed in the present work can be achieved by demonstrating the most important performance as listed in Table 2.

Table 2: Achieved frequency bands (obtained experimentally) by the proposed quad-band patch antenna and the corresponding gain and radiation efficiency

Center Frequency (GHz)	Start Frequency (GHz)	End Frequency (GHz)	Bandwidth (GHz)	Gain (dBi)	Radiation Efficiency
28	27.70	28.30	0.60	7.30	86.5%
45	44.50	46.50	2.00	7.03	87.5%
51	50.20	52.00	1.80	7.20	89.2%
56	55.70	57.00	1.30	8.03	90.0%

Table 3: Comparison among some millimetric-wave MIMO antennas available in some recent literature and the MIMO antennas proposed in the present work

Work:		[A01]	[A02]	[A03]	[A04]	[A05]	Present
Number of ports		7	4	2	2	4	4
Polarization	Co-polarized	√	√	√	√	√	√
	Cross-polarized	×	√	×	√	×	√
Minimum port isolation (*dB*)		−22	−23	−27	−23	−45	−20
Dimensions (mm^2)		60 × 25	44 × 44	55 × 110	75 × 40	47 × 33	20 × 20
Maximum ECC		0.01	0.0001	NA	0.0001	0.001	0.01
Minimum DG		9.955	9.9999	NA	9.9999	9.995	9.95
Operational frequencies (GHz)	Band 1	37.5	28	28	28	38	28
	Band 2	×	37.5	38	39	×	43
	Band 3	×	×	×	×	×	52
	Band 4	×	×	×	×	×	57
Bandwidth (GHz) at each frequency	Band 1	1.11	1.2	1.1	3.5	3.2	0.60
	Band 2	×	2.0	1.0	4.0	×	0.60
	Band 3	×	×	×	×	×	1.80
	Band 4	×	×	×	×	×	1.50
Gain (dBi) at each frequency	Band 1	7.7	8.0	7.0	5.0	6.5	7.30
	Band 2	×	13.6	8.0	5.7	×	7.03
	Band 3	×	×	×	×	×	7.20
	Band 4	×	×	×	×	×	8.03
Antenna efficiency at each frequency	Band 1	NA	97%	91.2%	99.5%	80%	86.5%
	Band 2	×	98%	89.6%	98.6%	×	87.5%
	Band 3	×	×	×	×	×	89.2%
	Band 4	×	×	×	×	×	90.0%

V. CONCLUSION

Novel designs for compact-size quad-band two-port MIMO antenna systems are introduced for the forthcoming generations of handsets for mobile communications over four frequency bands centered at 28, 43, 52, and 57 GHz. It is shown that the proposed MIMO antennas are well designed to produce appropriate radiation patterns and good impedance matching in the four frequency bands of operation. Some of the proposed two-port MIMO antennas provide spatial diversity while the other type is cross-polarized and provides polarization diversity. The performance of both the quad-band patch antenna and the MIMO antenna systems are assessed including the return loss at each antenna port and the coupling coefficients between the different ports. It is shown that the simulation results agree with the

experimental measurements and both show good performance of all the proposed types of MIMO antennas. The bandwidths achieved at approximately 28, 43, 52, and 57 GHz are 0.6, 0.6, 1.8, and 1.5 GHz, respectively. Also, the radiation efficiencies calculated at the four operational frequencies are 86.5%, 87.5%, 89.2%, and 90.0%, respectively. It is shown that the ECC and the DG are perfect over the four operational frequency bands for all the proposed types of two-port MIMO antenna systems.

REFERENCES

[1] R. Bhatti, J. Choi, and S. Park, "Quad-band MIMO antenna array for portable wireless communications terminals," *IEEE Antennas and Wireless Propagation Letters*, vol 8, pp. 129-132, 2009.

[2] H. S. Wong, S. Kibria, M. T. Islam, J. S. Mandeep, and N. Misran, "Quad band handset antenna for LTE MIMO and WLAN application," *International Journal of Antennas and Propagation*, 2014.

[3] M. Mishra and R. S. Kshetrimayum, "Compact Quad-band MIMO Antenna Array with Low Mutual Coupling for Mobile Terminal," In *IEEE Region 10 Symposium (TENSYMP)*, pp. 665-670, June 2019.

[4] C. Rajagopal, N. Noorullakhan, S. B. Suseela, and R. Sankararajan, "Compact modified circular patch quad-band MIMO antenna with high isolation and low correlation," *International Journal of Microwave and Wireless Technologies*, vol. 9, no. 3, pp. 581-590, 2017.

[5] C. Şeker, T. Ozturk, and M. Güneşer, "A single band antenna design for future millimeter wave wireless communication at 38 *GHz*," *European Journal of Engineering and Formal Sciences*, vol. 2, no. 2, pp. 35-39, 2018.

[6] E. M. Eldesouki, K. F. A. Hussein, and A. M. El-Nadi, "Circularly polarized arrays of cavity backed slot antennas for X-band satellite communications," *Progress in Electromagnetics Research*, vol. 9, pp. 179-198, 2008.

[7] K. F. A. Hussein, "Conical linear spiral antenna for tracking, telemetry and command of low earth orbit satellites" *Progress in Electromagnetics Research*, vol. 29, pp. 97-107, 2012.

[8] O. A. Elkady, S. A. Abolkassem, A. H. Elsayed, W. A. Hussein, and K. F. A. Hussein, "Microwave absorbing efficiency of Al matrix composite reinforced with nano-Ni/SiC particles," *Results in Physics*, vol. 12, pp. 687-700, 2019.

[9] H. Marzouk, M. I. Ahmed, and A. H. Shaalan, "Novel dual-band 28/38 GHz MIMO antennas for 5G mobile applications," *Progress in Electromagnetics Research C*, vol. 93, pp. 103-117, 2019.

[10] M. J. Riaz, A. Sultan, M. Zahid, A. Javed, Y. Amin, and J. Loo, "MIMO antennas for future 5G communications," In *2020 IEEE 23rd International Multitopic Conference (INMIC)*, pp. 1-4. IEEE, 2020.

[11] B. Aghoutane, S. Das, M. EL Ghzaoui, B. T. P. Madhav, and H. El Faylali, "A novel dual band high gain 4-port millimeter wave MIMO antenna array for 28/37 GHz 5G applications," *AEU-International Journal of Electronics and Communications*, p. 154071, 2021.

[12] S. Katragadda, and P. V. Y. Jayasree, "MIMO antenna miniaturization standards for future 5G," *International Journal of Intelligent Unmanned Systems*, vol. 10, no. 1, pp. 159-167, 2022.

[13] W. Ali, S. Das, H. Medkour, and S. Lakrit, "Planar dual-band 27/39 GHz millimeter-wave MIMO antenna for 5G applications," *Microsystem Technologies*, vol. 27, no. 1 pp. 283-292, 2021.

[14] D. A. Sehrai, M. Asif, N. Shoaib, M. Ibrar, S. Jan, M. Alibakhshikenari, A. Lalbakhsh, and E. Limiti, "Compact quad-element high-isolation wideband MIMO antenna for mm-wave applications," *Electronics*, vol. 10, no. 11, 2021.

[15] M. A. El-Hassan, A. E. Farahat, and K. F. A. Hussein, "Compact-size quad-band patch and MIMO antenna system for 5G mobile handsets," *Progress in Electromagnetics Research C*, vol. 112, 2021.

[16] M. A. El-Hassan, A. E. Farahat, and K. F. A. Hussein, "Quad-band MIMO antenna system for 5G mobile handsets," *Applied Computational Electromagnetics Society (ACES) Journal*, vol. 36, no. 11, 2021.

[17] A. E. Farahat and K. F. A. Hussein, "Dual-band (28/38 GHz) MIMO antenna system for 5G mobile communications with efficient DoA estimation algorithm in noisy channels," *Applied Computational Electromagnetics Society (ACES) Journal*, vol. 36, no. 3, pp. 282-294, 2021.

[18] A. E. Farahat and K. F. A. Hussein, "28/38 GHz dual-band Yagi-Uda antenna with corrugated radiator and enhanced reflectors for 5G MIMO antenna systems," *Progress in Electromagnetics Research C*, vol. 101, pp. 159-172, 2020.

[19] A. E. Farahat and K. F. A. Hussein, "Dual-band (28/38 GHz) yagi–uda antenna with corrugated radiator and triangular reflectors for 5G mobile phones," *Applied Computational Electromagnetics Society (ACES) Journal*, vol. 36, no. 10, pp. 1325-1334, 2021.

Asmaa E. Farahat received her B.Sc. and M.Sc. at the Department of Biomedical Engineering, Faculty of Engineering, Cairo University, in 2002 and 2006, respectively. She received her Ph.D. in 2012 from Ain Shams University. She is currently an Associate Professor at the Department of Microwave Engineering of the Electronics Research Institute. She has approximately 16 years of scientific research experience. She has published more than 30 papers in international, regional, and local scientific journals and conferences. She has worked as secondary investigator for 3research projects. Her research interests include antennas, electromagnetic wave propagation, risk assessment of human exposure to microwave radiation, remote sensing systems, and radar systems.

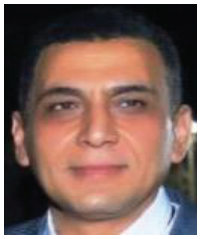

Khalid F. A. Hussein received his B.Sc., M.Sc., and Ph.D. degrees from the Department of Electronics and Electrical Communications, Faculty of Engineering, Cairo University in 1990, 1995 and 2001, respectively. He is currently as a professor at the Department of Microwave Engineering at the Electronics Research Institute. He has more than 30 years of scientific research experience. He has supervised more than 70 doctoral and master theses. He has published more than 110 papers in international, regional, and local scientific journals and conferences. He has served as Head of Microwave Engineering Department at the Electronics Research Institute for 4years. He has been a member of the Egyptian Space Program (currently the Egyptian Space Agency) for more than 8 years. He designed and implemented several satellite antennas between prototypes and finished products. His research interests include antennas, electromagnetic wave propagation, risk assessment of human exposure to microwave radiation, optical communications, photonics, quantum computing, radar systems, particularly ground penetrating radar (GPR), synthetic aperture radar (SAR), and remote sensing systems.

A Compact High Gain Wideband Metamaterial Antenna for Sub-6 GHz Applications

Ahmed A. Abbas and Balasem S. Samet

Department of Electrical Engineering
Faculty of Engineering, University of Anbar, Anbar, Iraq
Ahmed.abbas@uoanbar.edu.iq, balasem.sumait@uoanbar.edu.iq

***Abstract* –** This paper presents a design of high gain wideband antenna with metasurface for sub-6 GHz applications. The antennas at sub-6 GHz have a narrow bandwidth and low gain with a narrower axial ratio (AR). Hence, antennas combined with metamaterials are proposed to overcome these issues. The proposed metasurface antenna is designed with the implementation of W-shape transmission lines within the vias. The proposed antenna with metasurface is simulated using CST software and then fabricated on the FR4 substrate with ($\varepsilon_r = 4.4$ and $h = 1.6$ mm). The antenna performance achieved a wide bandwidth of 85% and operates at 2 GHz to 5 GHz. A compact size of 45% is achieved with a high gain of 7.12 dB. The proposed antenna is suitable to be used in future sub-6 GHz applications.

***Index Terms* –** antenna, compact size, sub-6 GHz wideband.

I. INTRODUCTION

Antenna systems in sub-6 GHz have been demanded to produce a high gain and wideband performance with compact size for cellular and wireless applications. It has been required for such antennas to provide compact size, directive beams, high radiation efficiency, and larger bandwidth [1–3]. Therefore, various types of antennas based on planar and non-planar technology have been introduced [4, 5]. However, such designed antennas have a narrow bandwidth and low gain with a narrow axial ratio [6]. In addition at sub-6 GHz, the antenna size using microstrip technology and waveguide-based structures are quite inflexible and big. Additionally, the antenna transmitter and receiver should be aligned to avoid losses by polarization mismatch. This generally occurred with linearly polarized antenna (LPA). Hence, the antenna with a circularly-polarized antenna (CPA) is proposed due to alignment avoidance.

Basically, a CP antenna requires two electric field components locaated orthogonally to each other with the same amplitude [6]. As a result, a narrow bandwidth is expected. In addition, the axial ratio of the CP antenna determines the polarization purity of the antenna [7]. Research has presented to enhance the axial ratio as well as the bandwidth in [8–13]. The method of inserting radiating elements within the integrated antenna is used in [9]. This method enhanced the impedance bandwidth by up to 15%. Another method is proposed in [10] with multiple feedlines inserted to radiate the element using of an external circuit to provide different phase shifts at each feed. Using this method provides a wideband of 30%. However, the size of the antenna is quite big and the performance of the antenna is limited by the phase shifter response. Cross antennas with dipoles are presented for wideband and axial ratio enhancement in [11]. In addition, another popular way to improve the bandwidth of microstrip antennas is proposed in [12, 13], by applying a stacked patch. However, all these designs still have limited bandwidth and AR enhancement of up to 30% in addition to the size and complexity issues.

Therefore, this paper presents a compact high gain wideband antenna using a vias structure and W-shape with square ring resonator (SRR) metasurface at sub-6 GHz. The proposed antenna is designed to achieve a wideband, axial ratio, and high gain. The antenna is designed to achieve an impedance bandwidth and an axial ratio of more than 1 GHz. The gain value aims to be higher than 5 dB. The proposed antenna is printed on a low-cost FR-4 substrate with $\varepsilon_r = 4.4$ and $h = 1.6$ mm. The measured results agreed well with simulated results and the antenna can be used in future sub-6 GHz applications.

II. DESIGN OF ANTENNA WITH METASURFACE

A. Design of W-shape antenna with vias structure

The vias-based structure with two air-filled vias rows is implemented in the substrate parallel to the W-patch. Vias operating principle includes making an artificial path within the substrate for guiding the wave. This could be accomplished by making holes or vias within the substrate. This leads to vias acting as a wall

Submitted On: May 15, 2022
Accepted On: October 2, 2022

https://doi.org/10.13052/2022.ACES.J.370807

replacement for the waveguide sidewalls. The rational selection of the vias in this work is to decrease the structure loading effect in the dielectric substrate. This helps in suppressing the structure standing waves and propagating the waves in the free space. The vias diameter (V_{via}) and the distance between each vias (p) are calculated using the following [13]:

$$D_{via} < \frac{\lambda_g}{5} \quad (1)$$

$$p \leq 2D_{via}. \quad (2)$$

To calculate the width of vias (W_{wsiw}) between any two parallel vias, the following formula is applied [13].

$$W_{eff} = W_{siw} - 1.08\frac{D_{via}^2}{p} + 0.1\frac{D_{via}^2}{W_{siw}}. \quad (3)$$

To achieve a wideband property, a self-similarity antenna is implemented with W-shape. The self-similarity or W-shape antennas have a constant electric patch over the frequency bandwidth. Whereas, the constant electric patch has been implemented in the dimension of the wavelength. Hence, the antenna is implemented with three transmission lines with a W-shape between the width of the vias as shown in Fig. 1. Each line is combined with two parallel vias to enable a bandwidth expanding more than 60%.

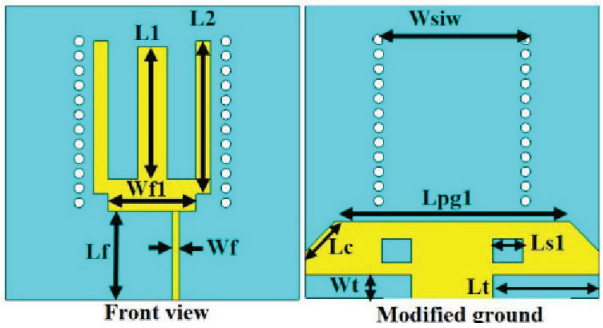

Fig. 1. The proposed W-shape vias antenna.

A parametric study in terms of the reflection coefficient (S_{11}) is performed on the proposed antenna with and without vias besides T-shape modified ground with respect to the diameter of vias as in Fig. 2 (a). Figure 2 shows the reflection coefficient responses with different values of vias diameter. It has been found that the optimal case for a wideband reflection coefficient is when the length of slot, width of slot, and vias diameter values are 17 mm, 3 mm, and 4 mm respectively. Hence, the antenna dimensions (in mm) are $L_1 = 23.5, L_2 = 22.5, L_f = 15, W_f = 1.25, _{f1\,t\,t}pg1_{s1}W_{f1} = 15, L_t = 14, W_t = 3, L_{pg1} = 40, L_{s1} = 5$

B. Metasurface design and integration with antenna

Metasurface is characterized by its resonant frequency (f). The resonant frequency is calculated with the

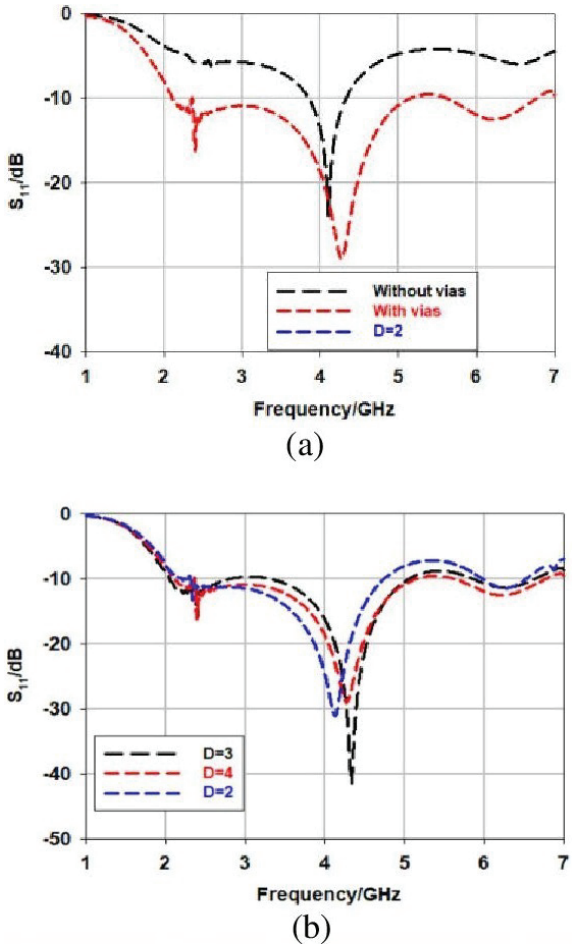

Fig. 2. (a) Reflection coefficient with and without vias, (b) Reflection coefficient at several vias dimeter values.

considerations of the capacitance (C) and inductance (L) properties of the transmission line. By altering the values of capacitance and inductance, the frequency is shifted to the higher or lower frequency or toward desired frequency. The resonant frequency can be found by [14]:

$$f = \frac{1}{2\pi\sqrt{LC}}. \quad (4)$$

Therefore, the elements' conductivity are filtered using a lattice etched on a dielectric substrate. This forms a full metasurface consisting of multiple unit cells. This also allows the metasurface to pass or reject certain signal at specific frequency. Therefore, a metasurface is implemented using square split ring resonator (SSRR) to increase the gain of the antenna. Similarly, the metasurface is fabricated by low-cost FR4 substrate with same height and permittivity as antenna. The unit cell is designed with four SSRR cells as shown in Fig. 3. The frequency of the four SSRR is found by [14]:

$$f_0 = \frac{1}{2\pi\sqrt{L\left[\left(2l - \frac{g}{2}\right)C + \frac{\varepsilon_0 wh}{2g}\right]}}. \quad (5)$$

Where, the length of unit cell is (L), the width of the cell is (WW), the gap between each cell is (S), the cut in each SSR is (g), and the width of last resonator is (SS). The capacitance and the inductance can be obtained as [14]:

$$C = \frac{\sqrt{\varepsilon_e}}{c_0 z_0} \tag{6}$$

$$L = 0.00508l\left(2.303\frac{4l}{w} - \theta\right) \tag{7}$$

$$l = \frac{\lambda}{N} N = 4,\ 10,\ 20,\ \ldots.,\ N\text{-}1. \tag{8}$$

Hence, the values of the unit cell is as follows: $L =$ 7 mm, $ww = 0.5$ mm, $S = 0.4$ mm, $g = 0.5$ mm, and SS = 1 mm.

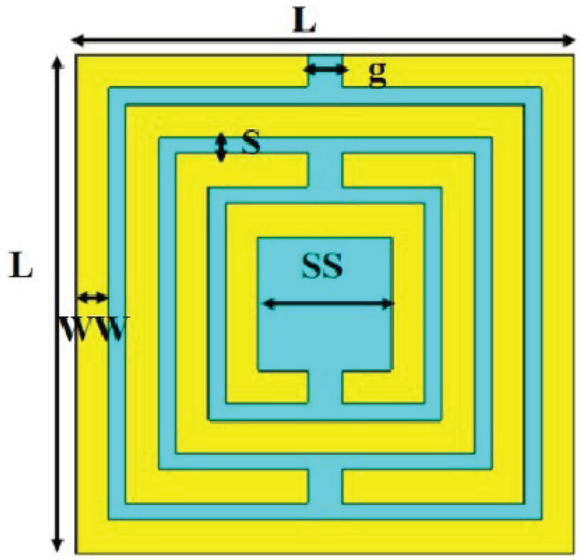

Fig. 3. SSRR unit cell design.

Figure 4 shows the performance of the SSRR unit cell in terms of S-parameters, permittivity (ε), and permeability (μ). The reflection coefficient (S_{11}) is shifted below 3.5 GHz as one SSRR is added to the shape as shown in Fig. 4 (a). The transmission coefficient is lagged the reflection coefficient in lower frequency when it compares with higher frequency more than 3.5 GHz as shown in Fig. 1 (b). The method used to extract the metamaterial properties is based on detecting the discontinuity points. This method is simple and works effectively by extracting the discontinuity points from the real part of the refractive index. The permittivity is negative from the range of 3 GHz to 4 GHz as the permeability is positive at sub-6 GHz. Hence, the proposed unit cell behaves as an epsilon-negative metamaterial (ENG) as seen in Fig. 4 (c) and Fig. 4 (d) respectively.

As a result, the SSRR unit cell is integrated to form a 5 × 5 metasurface structure as seen in Fig. 5. The proposed metasurface is symmetric, which gives the same

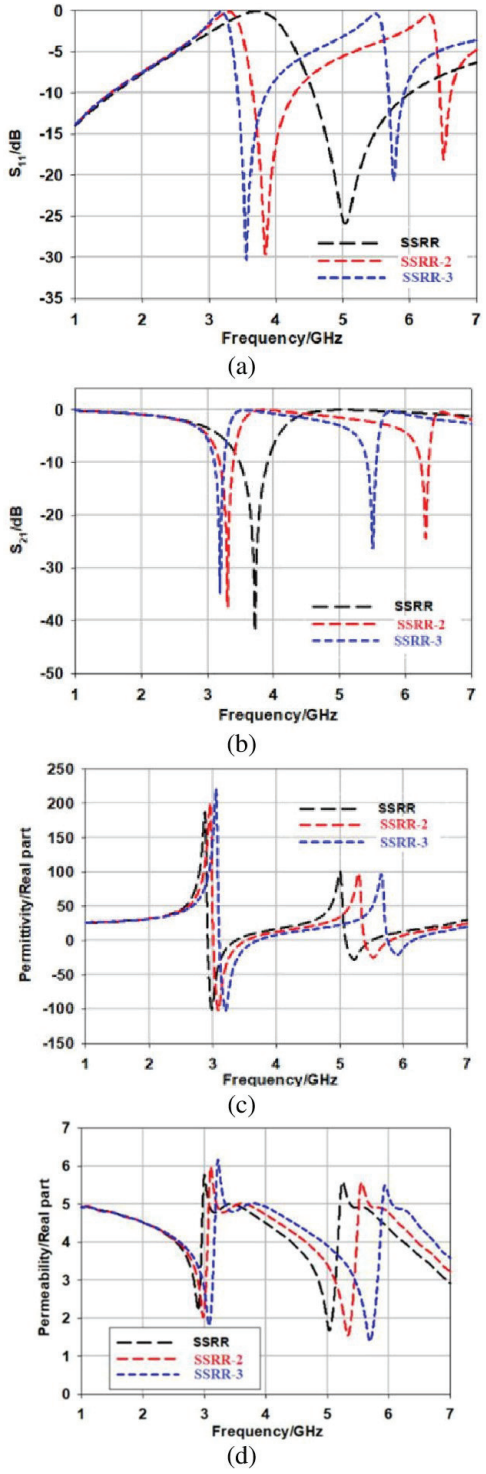

Fig. 4. The performance of the SSRR unit cell. (a) Reflection coefficient. (b) Transmission. (c) Permittivity. (d) Permeability.

cross-polarization and co-polarization under the normal x-polarized EM wave. The co-polarization at a range of 4.2 GHz to 4.45 GHz is less than −10 dB. At a frequency

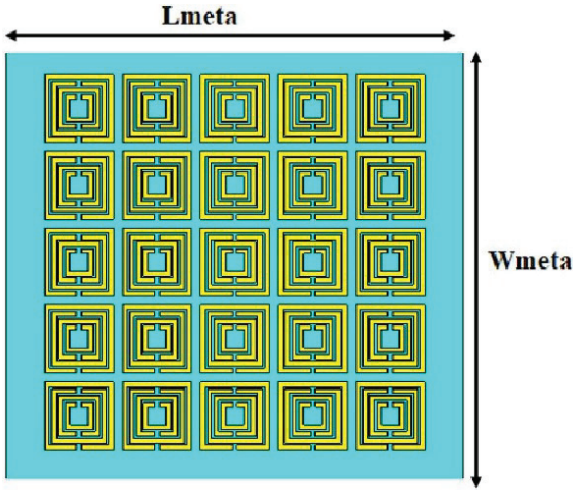

Fig. 5. The proposed 5 × 5 metasurface configuration.

range above 6 GHz, the co-polarization remains less than −10 dB as seen in Fig. 6 (a). The cross-polarization value is within 1− dB in the range of mid-band (at 3.5 GHz).

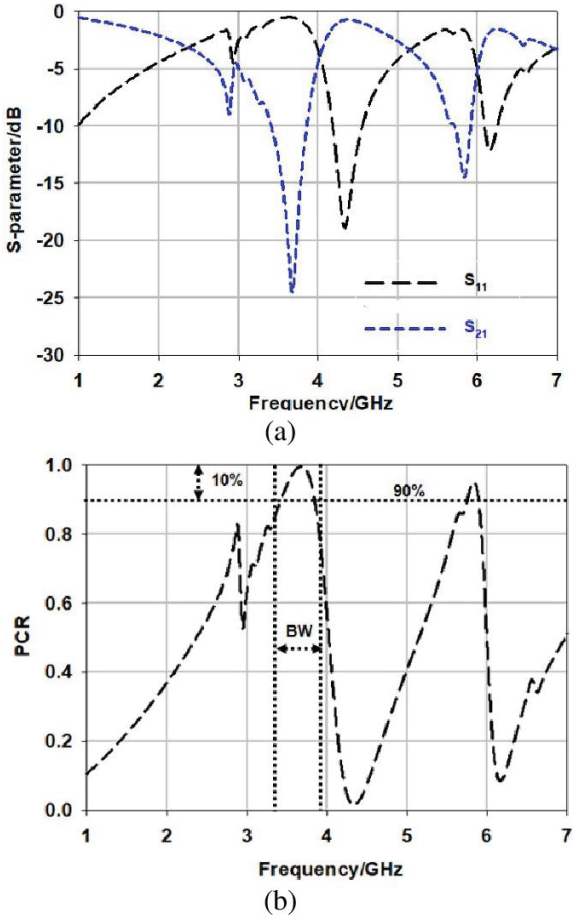

Fig. 6. Simulated response of 5 × 5 metasurface (a) reflection and transmission coefficients. (b) PCR.

At 3.5 GHz and 5.8 GHz, the PCR achieved a value higher than 90 % as seen in Fig. 6 (b). Therefore, the metasurface validates the increasing of current surface toward increases the gain. The proposed 5 × 5 metasurface is placed above a proposed antenna to validate the high gain property as presented in Fig. 7. The proposed structure consists of antenna layer at bottom and metasurface layer with unit cells are faced the antenna from above with a separation distance (air) between the layers (*d*). Figure 8 presents the comparison of simulated results in terms of the reflection coefficient, gain, axial ratio, and radiation pattern of the antenna with respect to metasurface at d = 15 mm. At 3.5 GHz, it has been found that the reflection coefficient is −23.5 dB with fractional bandwidth of 3 GHz for both antenna and metasurface antenna as in Fig. 8 (a). The gain is increased to 7.33 dBi when the SSRR metasurface is applied compared to the gain of antenna of 2.33 dBi as in Fig. 8 (b). Both axial ratios in the two cases sill same over the bandwidth with less than 3 dB as in Fig. 8 (c). Circularly polarized radiation pattern of 2.3 dB can be seen without metasurface applied compared to directive radiation pattern of 8 dB when metasurface is applied as shown in Fig. 8 (d). As a result, the simulated performance of the antenna with metasurface showed a great impedance bandwidth, high gain, and wide axial ratio.

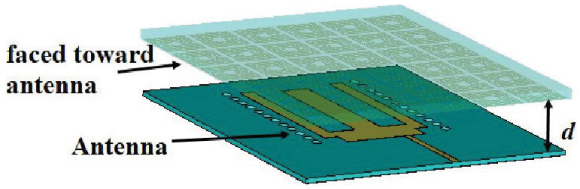

Fig. 7. The proposed metasurface placed above the antenna.

III. RESULTS AND DISCUSSION

Figure 9 shows the printed antenna with metasurface with total dimensions of 50 mm × 50 mm that highlighted the compact size of the whole system. The measured results in terms of S-parameters are performed using Keysight (Agilent Technologies) N9925A vector network analyser (VNA). The performance of printed antenna with metasurface in terms of reflection coefficient, radiation pattern, gain, and AR are compared with simulated results in Fig. 10.

The measured performance of the reflection coefficient is plotted in Fig. 10 (a). The measured (S_{11}) is −23.58 dB compared to the simulated one of −30.2 dB at 4 GHz. The measured fractional bandwidth is 2.99 GHz with a loss of 100 MHz of simulated bandwidth (3 GHz). The measured radiation pattern agreed well with the simulated one with an error tilt of 3 degrees

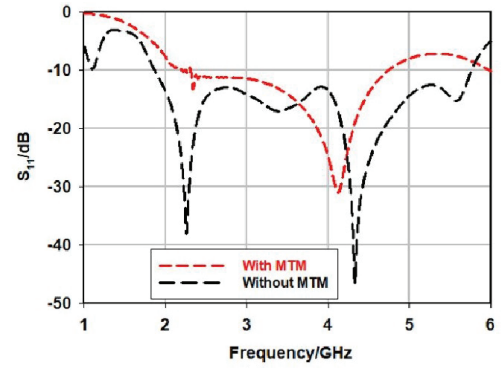

(a)

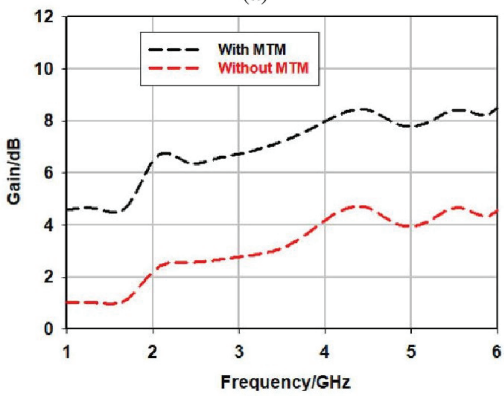

(b)

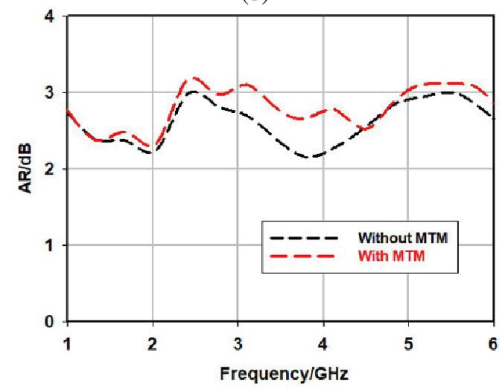

(c)

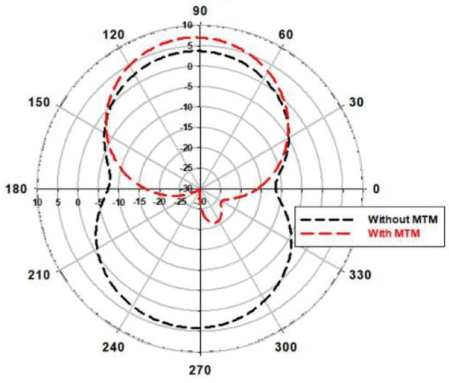

(d)

Fig. 8. Comparison of proposed antenna with and without Metasurface. (a) Return loss. (b) Gain. (c) Axial ratio. (d) Radiation pattern.

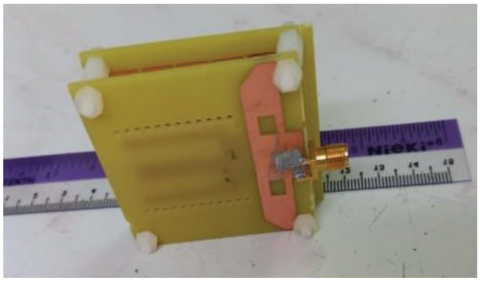

Fig. 9. The printed metasurface with antenna.

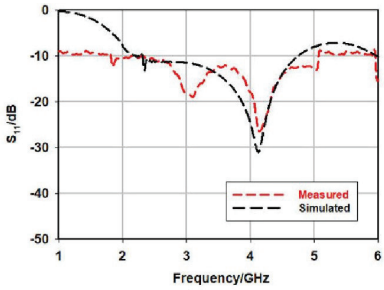

(a)

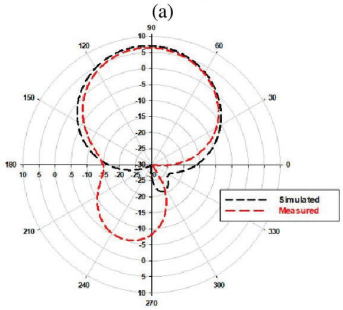

(b)

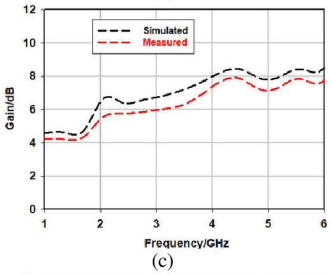

(c)

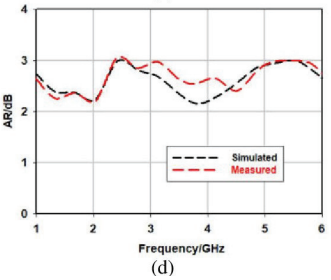

(d)

Fig. 10. The measured performance of the printed fractal antenna. (a) Reflection coefficient. (b) Radiation pattern. (c) Gain. (d) AR.

as seen in Fig. 10 (b). Figure 10 (c) shows the measured gain response compared to the simulated one. The measured gain is 7.2 dBi with 0.8 dBi loss compared to the simulated 8 dBi gain. This is due to the interference coming from the unwanted sources from the radiation pattern chamber. The AR performance is compared in Fig. 10. Over the operating frequencies, the AR value is above 82%. For example, at 4 GHz the measured and simulated AR has a small gap of 0.5 dB difference. Table 1 summarizes the antenna with metasurface performance and compares it with other related works. Overall, the printed antenna with metasurface exploited a great performance in terms of bandwidth, AR, and gain.

Table 1: Comparison between measured and simulated antenna with metasurface at 4 GHz with related existing works

Parameters/Coupler		Simulated		Measured
Return loss (S_{11}) (dB)		−30.2		−23.58
Bandwidth (GHz)		3		2.90
Gain (dBi)		8		7.2
AR (dB)		2.2		2.5
Comparison with related works				
Ref	Gain	BW (GHz)	Size %	AR (BW)
[9]	2.56	2.19 GH −	50%	3.39 GHz −
	dBi	3.7 GHz		3.55 GHz
[10]	3.2	2.43 GHz −	65%	2.43 GHz −
	dBi	2.47 GHz		2.47 GHz
[11]	2.5	12.2 GHz −	−	12.2 GHz −
	dBi	12.7 GHz		12.7 GHz
[12]	1.89	1.57 GHz −	20%	1.57 GHz −
	dBi	1.62 GHz		1.62 GHz
This	7.12	2 GHz −	45.2%	2.5 GHz −
work	dBi	5 GHz		5 GHz

IV. CONCLUSION

A designed compact high gain wideband with a metasurface antenna is presented in this paper at the sub-6 GHz band. The antenna is designed based on a W-shaped transmission line within the structure. The performance of the proposed metasurface antenna agreed well with the simulated results. Excellent S-parameters, bandwidth, gain, and AR performance at 4 GHz are achieved for the designed antenna. The antenna operates in the frequency band of 2 GHz to 5 GHz with a high fractional bandwidth of 85%. The antenna achieved a good profile of compact size by 45%. The proposed antenna is suitable to be used later in sub-6 GHz applications.

REFERENCES

[1] Y. He, S. Lv, L. Zhao, G.-L. Huang, X. Chen, and W. Lin, "A compact dual-band and dual-polarized millimeter-wave beam scanning antenna array for 5G mobile terminals," *IEEE Access*, vol. 9, pp. 109042-109052, 2021.

[2] I. Syrytsin, S. Zhang, G. F. Pedersen, and A. S. Morris, "Compact quad-mode planar phased array with wideband for 5G mobile terminals," *IEEE Transactions on Antennas and Propagation*, vol. 66, no. 9, pp. 4648-4657, 2018.

[3] N. O. Parchin, J. Zhang, R. A. Abd-Alhameed, G. F. Pedersen, and S. Zhang, "A planar dual-polarized phased array with broad bandwidth and quasi-end fire radiation for 5G mobile handsets," *IEEE Transactions on Antennas and Propagation*, vol. 69, no. 10, pp. 6410-6419, 2021.

[4] Y. Kumar and S. Singh, "Microstrip fed multiband hybrid fractal antenna for wireless applications," *Applied Computational Electromagnetics Society (ACES) Journal*, vol. 31, no. 3, pp. 327-332, 2016.

[5] M. I. Sabran, S. K. A. Rahim, P. J. Soh, C. Y. Leow, and G. A. E. Vandenbosch, "A simple electromagnetically fed circularly-polarized circular microstrip antenna," *Applied Computational Electromagnetics Society (ACES) Journal*, vol. 30, no. 11, pp. 1180-1187, 2015.

[6] M. Majidzadeh, J. Nourinia, and C. Ghobadi, "Compact CPW-Fed antenna with circular polarization characteristics in WLAN frequency band," *Applied Computational Electromagnetics Society (ACES) Journal*, vol. 28, no. 10, 2013.

[7] Y. Liu, X. Liang, X. Zhang, J. Li, J. Geng, R. Jin, and L. Zhang, "A K-band broadband circularly polarized slot antenna based on L-shaped waveguide cavity," *IEEE Antennas and Wireless Propagation Letters*, vol. 20, no. 9, pp. 1606-1610, 2021.

[8] Z. Zhou, Z. Wei, Z. Tang, and Y. Yin, "Design and analysis of a wideband multiple-microstrip dipole antenna with high isolation," *IEEE Antennas and Wireless Propagation Letters*, vol. 18, no. 4, pp. 722-726, 2019.

[9] X. Shuai and S. Xiao, "A novel dual-band circularly polarized slot antenna with fractal slot geometry," *Microwave and Optical Technology Letters,* vol. 59, no. 2, pp. 451-456, 2017.

[10] S. Maity, K. R. Barman, and S. Bhattacharjee, "Silicon-based technology: Circularly polarized microstrip patch antenna at ISM band with miniature structure using fractal geometry for biomedical application," *Microwave and Optical Technology Letters*, vol. 60, no. 1, pp. 93-101, 2018.

[11] K. S. Kola, A. Chatterjee, and D. G. Patanvariya, "Design of a wideband right-handed circularly polarized array of miniaturized mushroom-shaped antennas for direct broadcast satellite application," *Microwave and Optical Technology Letters*, vol. 62, no. 11, pp. 3542-3555, 2020.

[12] E. Wang, M. Liu, D. Lin, and J. Wang, "A compact circular polarized patch fractal antenna for global navigation satellite systems," *Microwave and Optical Technology Letters*, vol. 64, no. 3, pp. 520-524, 2022.

[13] Z. Zhang, Y. Fan, and Y. Zhang, "Multilayer half-mode substrate integrated waveguide wideband coupler with high selectivity," *Applied Computational Electromagnetics Society (ACES) Journal*, vol. 34, no. 9, pp. 1418-1425, 2019.

[14] H. A. Atallah, A. B. Abdel-rahman, K. Yoshitomi, and R. K. Pokharel, "Mutual coupling reduction in MIMO patch antenna array using complementary split ring resonators defected ground structure," *Applied Computational Electromagnetics Society (ACES) Journal*, vol. 31, no. 7, pp. 737-743, 2016.

Ahmed A. Abbas has been the head of the Electrical Engineering Department, College of Engineering, and the University of Anbar since 2018. He received a B.Sc. degree in Electrical Engineering from the University of Technology in 1994, an MS.c. in Communication Engineering from the University of Technology in 2005 and his Ph.D. in Communication Engineering from Ankara Yıldırım Beyazıt University in 2017. Dr. Ahmed is a researcher in the field of communications, particularlyin optical wave propagation through random media.

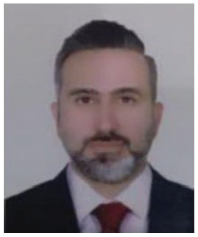

Balasem Salem Samet is a lecturer at the Electrical Engineering Department, College of Engineering, University of Anbar. He received a B.Sc. degree in Electrical Engineering from the University of Technology in 2000, received an MS.c. in Communication Engineering (University of Technology) in 2005, and received Ph.D. in Communication Engineering in 2013. Dr. Balasem is a researcher in wireless communication and smart antennas.

A Wideband Base Station Antenna Loaded with Bow-Tie-Like Parasitic Elements

Junwei Qi[1], Jiakang Pan[1], Yingsong Li[2,*], and Guan-Long Huang[3]

[1]College of Information and Communication Engineering
Harbin Engineering University, Harbin 150001, China

[2]Key Laboratory of Intelligent Computing and Signal Processing Ministry of Education
Anhui University, Hefei, China

[3]School of AI - Guangdong & Taiwan, Foshan University
Foshan, Guangdong 528225, China
*liyingsong@ieee.org

***Abstract* –** A $\pm 45^\circ$ dual-polarization wideband antenna for 5G base station application is proposed using cross dipoles, bow-tie-like parasitic elements and baluns. The antenna is modeled, simulated, and optimized for an optimal size of 115 mm $\times$ 115 mm $\times$ 27.8 mm. A -10dB bandwidth is obtained to cover 2.24GHz-3.75GHz, which has a fractional bandwidth of 50.4%. In the design, bent Γ-shaped microstrip lines are to achieve higher isolation that is better than 25dB. The proposed antenna is fabricated and measured to get a result that it has a wide bandwidth, good directional radiation patterns, and a high peak gain of 8.1 ± 1.1dBi, making it suitable for 5G base station applications.

***Index Terms* –** 5G application, $\pm 45^\circ$ dual-polarized antenna, cross dipole antenna, wideband antenna.

I. INTRODUCTION

With the continuous improvement of communication technology, the requirements of BS antenna are also significantly elevated. Especially, in the 5G era, for the sake of achieving a higher data transmission rate, the operation bandwidth of the BS antenna must be improved [1]–[2]. For enhancing the operating bandwidth of the BS antenna, pattern distortion, cross-polarization deterioration, and decreasing the front-to-back ratio (FBR) are always found in the previous designs. Therefore, the wideband base station antenna research is a hot topic for 5G applications [3]. For 5G applications, a dual-polarized antenna is widely used in BS antennas, which can provide diversity gain and reduce the impact of the multipath effect on the system [4]. Till now, dual-polarized antennas can be divided into $\pm 45^\circ$ polarization or horizontal and vertical polarization on the base of polarization direction. In addition, the dual-polarized antenna can also be divided into cross dipole type [5]–[6], microstrip type [7], and slot type [8]. Among the three types of dual-polarized antennas, the cross dipole has been studied widely because of its high port isolation and directional radiation characteristics [9]-[11].

In the past decades, many dual-polarized BS antennas have been proposed [12]-[14]. A miniaturized cross dipole antenna is proposed in [15]. The antenna is installed in a dielectric resonant cavity to get an FBR of 22dB in the operating frequency band, with a bandwidth of 3.2GHz-3.7GHz. In [16], a broadband cross dipole antenna is proposed to get a -15dB impedance bandwidth range from 1.7GHz to 2.7GHz, and the fractional bandwidth reaches 48%. But the isolation of the dual-polarized port of the antenna is only 22dB. A folded dipole antenna with a metal reflector is proposed in the literature [17]. The antenna increases the resonance points and greatly improves the antenna impedance bandwidth by bending the dipole and adding via, which might deteriorate the radiating. In [18], a broadband and high isolation dual-polarized antenna is presented. Compared with the traditional dual-polarized antenna, the antenna employs a resonance ring and a square plate to expand bandwidth and improve directionality. However, its height is increased.

In this work, a wideband dual-polarized antenna consisting of a pair of T-shaped dipoles, bow-tie-like parasitic elements, microstrip baluns, and a box-like reflector is proposed, analyzed, fabricated, and measured. The cross dipoles are used as the main radiator, and the bow-tie-like parasitic elements are surrounded the cross dipoles to expand the bandwidth of the proposed antenna. The orthogonal microstrip baluns not only feed the upper radiator patches through coupling but also support the entire structure of the antenna, making the

Submitted On: April 18, 2022
Accepted On: September 24, 2022

https://doi.org/10.13052/2022.ACES.J.370808

antenna easier to assemble and more stable. Also, Γ-shaped microstrip lines are used to enhance the isolation of the antenna. In the operating frequency band, the gain is 8.1±1.1dBi, and the −3dB beam width is 63°±5°. In addition, due to the existence of a box-like metal reflector, the FBR of the antenna is higher than 17dB. Thus, the wideband BS antenna is suitable for 5G BS application.

II. ANTENNA DESIGN AND ANALYSIS

A. Antenna design

Figure 1 shows the configuration of the proposed dual-polarized antenna that is composed of cross dipoles, bow-tie-like parasitic elements, baluns, and a box-like metal reflector. A pair of balun is placed orthogonally to feed the radiation structure and support the antenna. All the baluns, dipoles, and parasitic elements are created on FR4 with relative permittivity = 4.4 and loss tangent =0.02, whose thickness is 0.8 mm thick as the FR4. The box-like reflector is welded by a 115 mm×115 mm copper base plate and four 115 mm× 16 mm copper coamings. The thickness of all copper plates is 0.8 mm. The box-like metal reflector enables the cross dipole antenna to radiate directionally in the +Z axis direction.

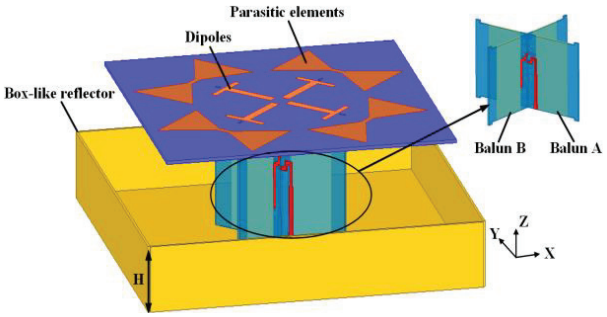

Fig. 1. Configuration of proposed antenna.

The detailed configuration of the radiation structure is shown in Fig. 2 (a). Four T-shaped patches form pairs of cross dipoles, which are surrounded by bow-tie-like parasitic elements. In Fig. 2 (b), two circular holes are drilled to connect with the 50-Ω coaxial line. The inner conductor of the 50-Ω coaxial line will be connected with a Γ-shaped microstrip line through a circular hole, and the outer conductor will be connected with the box-like reflector. Four rectangular slots are used to fix the antenna.

Figures 3 (a) and (b) present the feeding baluns for implementing the dual polarization. The Γ-shaped microstrip lines are printed on one side of FR4, while two thin rectangular copper sheets are printed on the other side of the FR4. Two complementary slots are etched in the middle of the balun sheets to provide a convenient

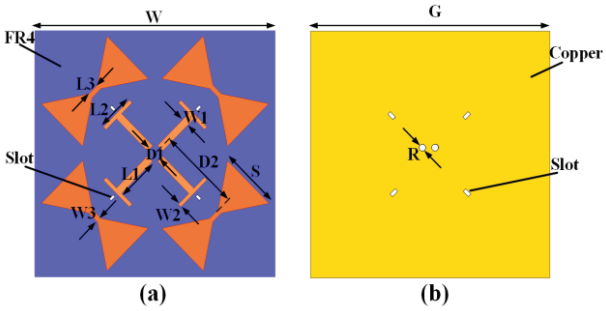

Fig. 2. (a) Configuration of the radiation structure. (b) Configuration of the reflector base plate.

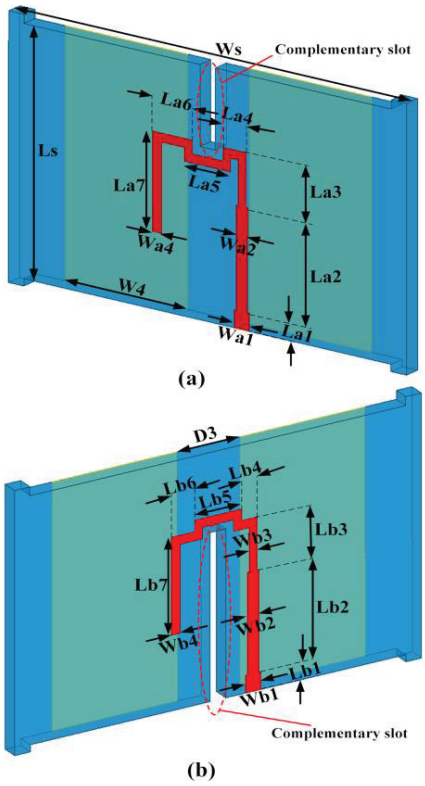

Fig. 3. Configuration of the baluns, (a) balun A and (b) balun B.

installation for the constructed antenna. In addition, four corners of the FR4 of baluns have bumps which are connected with the rectangular slots on the FR4 of radiating layer and a box-like metal reflector to give stable support for the constructed antenna.

The antenna is created in the HFSS, and it is optimized to achieve a good performance. The details of the geometric dimensions of the proposed antenna are shown in Table 1. The overall size of the antenna is 115 mm×115 mm× 27.8 mm.

Table 1: Optimized parameters for the geometric parameters of the antenna

Parameters	H	W	G	R	S	W1	W2
Value(mm)	16	100	115	1.84	24	3	1.5
Parameters	W3	W4	L1	L2	L3	D1	D2
Value(mm)	2	16	18	15	5	6	34
Parameters	D3	WS	LS	Wa1	Wa2	Wa3	Wa4
Value(mm)	8	52	26	1.5	0.8	0.5	0.7
Parameters	Wb1	Wb2	Wb3	Wb4	La1	La2	La3
Value(mm)	1.5	1	0.5	0.7	2	11.5	5.5
Parameters	La4	La5	La6	La7	Lb1	Lb2	Lb3
Value(mm)	2	5	3.7	11	2	11.5	5.5
Parameters	Lb4	Lb5	Lb6	Lb7			
Value(mm)	2	5	3.7	11			

B. Antenna analysis

To better illustrate the implementation principle of the wideband BS antenna, the radiation structure design procedure of the antenna is presented in Fig. 4. ANTA_1 only consists of four T-shaped patches to form a pair of cross dipoles to achieve ±45° polarization. Then, rectangle parasitic elements are used to form ANTA_2. At last, the rectangle parasitic elements are modeled to be bow-tie-like parasitic elements for the proposed antenna with a name of ANTA_3.

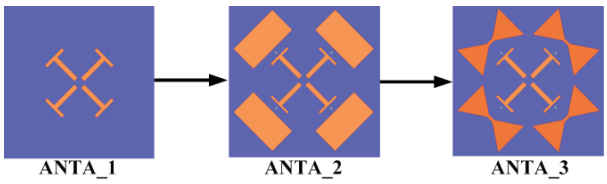

Fig. 4. Evolution of the antenna radiation structure.

Then, the principle of the antenna is discussed based on the current distribution in Fig. 5 and Fig. 6. We can see that ANTA_1 has a resonance point at approximately 3.5GHz owing to the current distributions on the T-shaped dipoles. When we use the rectangle parasitic elements for ANTA_2, the current path are expanded to the parasitic elements, and hence the bandwidth of the antenna is increased. In the same method, bow-tie-like parasitic elements are adopted in ANTA_3 to enhance the bandwidth of the proposed antenna.

On the basis of ANTA_2, ANTA_3 modifies the parasitic element to bow-tie-like shape. The S-parameter for the antenna at different design procedures are shown in Fig. 7. It is found that the ANTA_1 has only one resonant mode, and with a bandwidth of approximately 400MHz. For the ANTA_2, it has a new resonant mode to expand the bandwidth to around 600MHz. Finally, ANTA_3 employs bow-tie-like parasitic elements to further expand the bandwidth via providing another new resonant mode at lower frequency. As a result, a wider −10dB impedance bandwidth for the ANTA_3 is achieved, which operates from 2.24Ghz to 3.75GHz with a bandwidth of 1.51GHz.

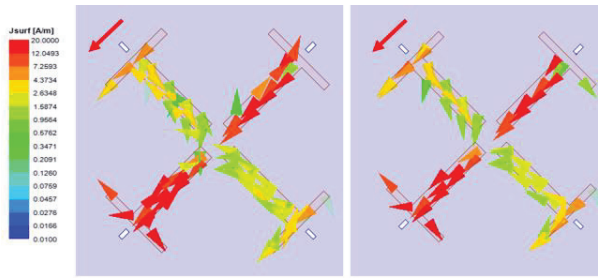

Fig. 5. Surface current distribution, (a) 3.2GHz, ANTA_1, (b) 3.5GHz, ANTA_1.

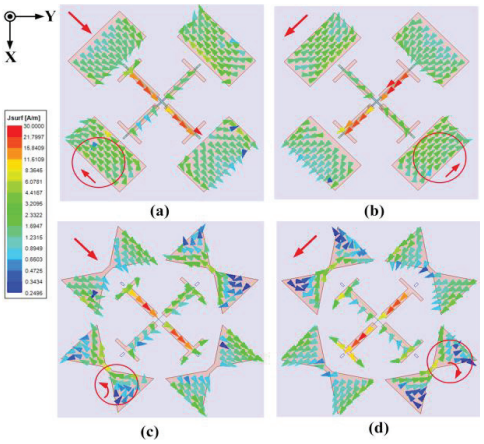

Fig. 6. Surface current distribution in 3.5GHz. (a) The ANTA_2 with only port 1 excitation. (b) The ANTA_2 with only port 2 excitation. (c) The proposed antenna with only port 1 excitation. (d) The proposed antenna with only port 2 excitation.

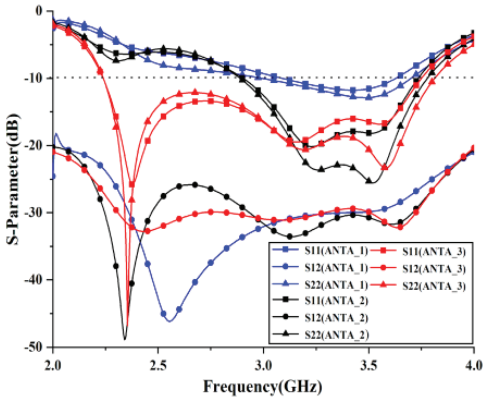

Fig. 7. Simulated S-parameters of ANTA_1, ANTA_2, and ANTA_3.

Although the introduction of parasitic elements is beneficial to expand the operating bandwidth of the BS antenna, it will affect the radiation performance. In Figs. 6 (a) and (b), ANTA_2 with rectangular parasitic elements maintains the current distribution in the same direction as the T-shaped dipoles, while the other two parasitic elements have coupling currents in the opposite direction with respect to the current of dipoles. There is no doubt that reverse coupling current will affect the radiation performance of the antenna and reduce the pattern stability. As for proposed antenna, it uses bow-tie-like parasitic elements to give stable current distribution presented in Figs. 6 (c) and (d).

III. RESULT AND DISCUSSION

A. Antenna numerical simulation

For the sake of obtaining larger antenna bandwidth, it is necessary to analyze quantitatively the antenna parameters. Since the balun is the key element to realizing impedance matching, the balun parameters are mainly analyzed quantitatively.

L1 is a parameter that determines the length of the T-shaped dipole. The S-parameters of the antenna with different L1 are shown in Fig. 8. When L1 increases, the lowest frequency moves to the lower frequency, getting a larger bandwidth, and vice visa. The distance between T-shaped dipole and bow-tie parasitic element also affects the impedance matching of the antenna, which is demonstrated in Fig. 9 with varying D2. When D2 increases, the impedance bandwidth will be expanded slightly. The effect for different LS is presented and shown in Fig. 10, where we can see that the antenna has the best bandwidth for LS = 26 mm.

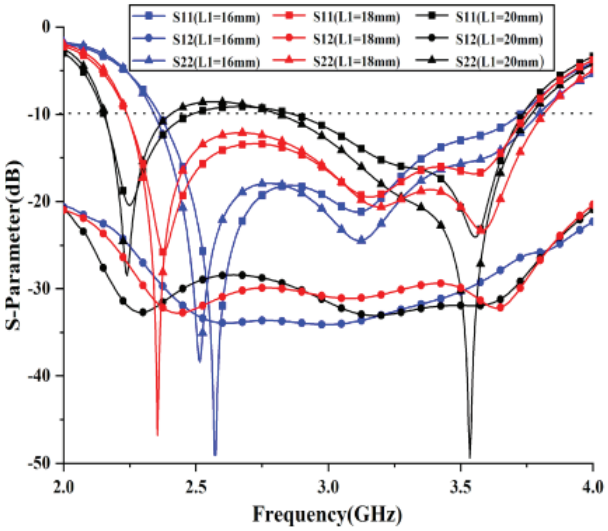

Fig. 8. Simulated S-parameters of the proposed antenna with different L1.

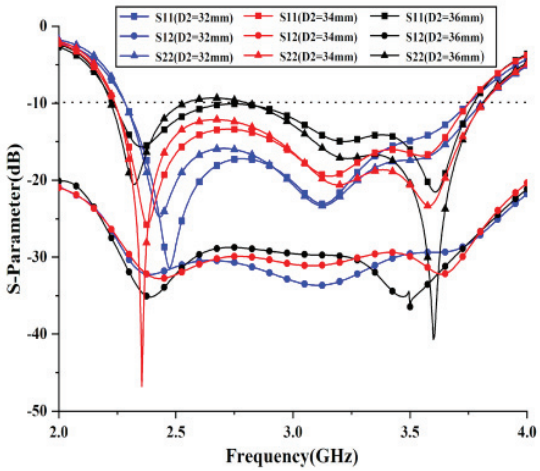

Fig. 9. Simulated S-parameters of the proposed antenna with different D2.

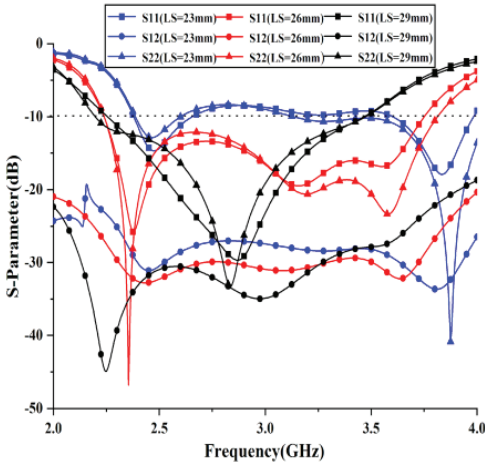

Fig. 10. Simulated S-parameters of the proposed antenna with different LS.

B. Performance for the fabricated antenna

To verify the simulation results of the antenna, a prototype of the proposed antenna is manufactured and tested. Figure 11 shows and sets up the prototype antenna. The S-parameters of the prototype antenna are tested using the vector network analyzer-Agilent N5244A and compared with the simulation results in Fig. 13. The −10dB impedance bandwidth of simulation and measurement has a little difference that is caused by fabrications. In addition, within the operating bandwidth, the simulated isolation and measured isolation between the two ports is better than 25dB.

Figure 13 shows the simulated and measured peak gain and the radiation efficiency of the proposed antenna. In the operating frequency band, the simulated peak gain range is 8.1±1.1dBi and the 3dB beam-width of the antenna is 63°±5°. The measured peak gain is slightly

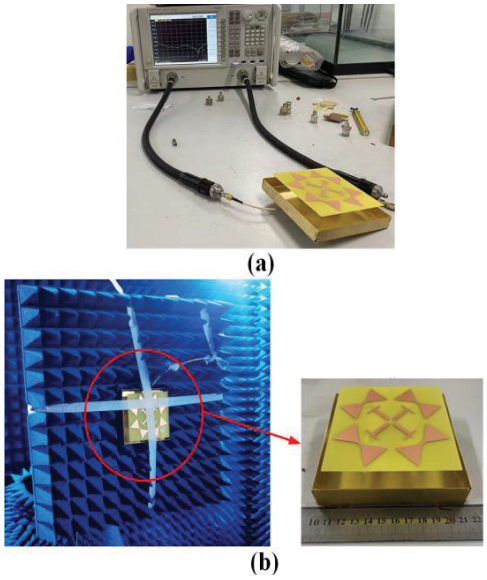

Fig. 11. Photograph of prototype antenna. (a) Antenna on test for S-parameters. (b) Antenna radiating performance on test.

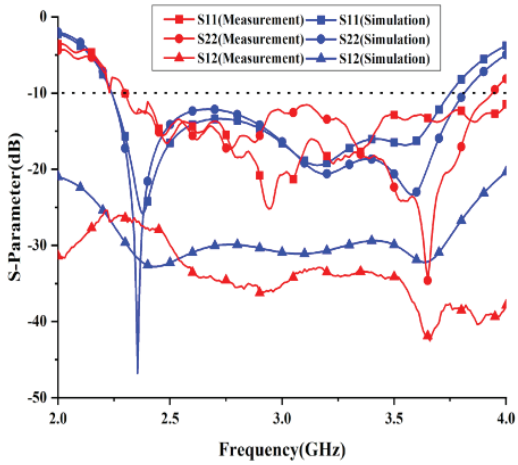

Fig. 12. Simulated and measured S-parameters of the base station antenna.

lower than the simulation result, which is caused by the insertion loss caused by the fabrication of the prototype antenna. On the other hand, it can be seen in Fig. 13 that the radiation efficiency of the antenna in the operating bandwidth is higher than 90%. In Fig. 14, only the radiation patterns of port 1 at 2.4GHz, 3.0GHz, and 3.6GHz are given, since the antenna is symmetry between port 1 and port 2. It can be seen that the radiation patterns of the antenna have a high coincidence between the simulated result and the measured result. In addition, the cross-polarization discrimination (XPD) of the designed BS antenna is over 30 dB in the boresight direction. The achieved front-to-back-ratio (FBR) is better than 17dB,

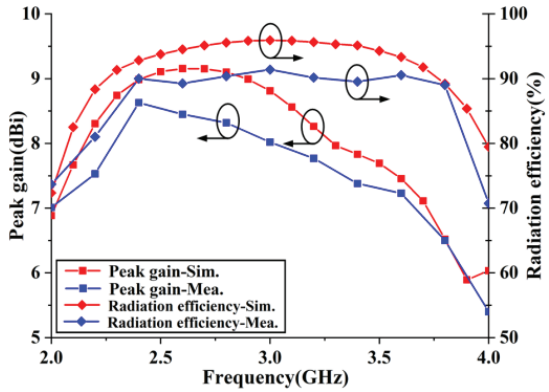

Fig. 13. The peak gain and radiation efficiency of the BS antenna.

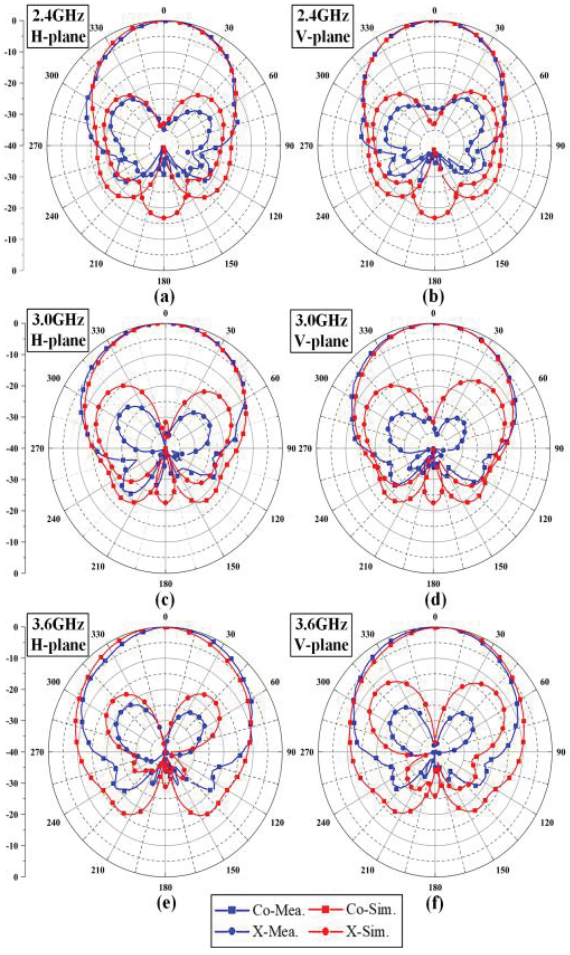

Fig. 14. Simulated and measured radiation patterns at 2.4 GHz, 3.0 GHz and 3.6 GHz.

meaning that the back radiation of the proposed antenna is suppressed well. Table 2 shows the performance comparison between the proposed antenna and the existing dual-polarized antenna (λ is the wavelength correspond-

Table 2: Comparison of the proposed antenna with existing dual-polarized antennas

Ref.	Operation band (GHz)	XPD (dB)	Isolation (dB)	Gain (dBi)	FBR (dB)	Profile height
[15]	3.25-3.75 (11.4%)	>25	>30	∼7	18	0.21λ
[16]	1.6-2.9 (48%)	>25	>22	8.2	∼20	0.24λ
[17]	1.15-4.07 (107%)	>20	NS	>8.2	11.5	0.38λ
[18]	1.71-2.69 (44.5%)	>25	>22	∼8	18	∼0.39λ
[19]	1.68-2.75 (48%)	>20	>37	8.9±0.7	15.5	0.18λ
[20]	3.28-3.71, 4.8-5.18 (12.3,7.6)	>20	>37	8.7±1.8	∼13	0.13λ
This work	2.24-3.75 (50.4%)	>30	>25	8.1±1.1	>17	∼0.28λ

ing to the central frequency). It is to say that the proposed antenna is a wideband BS antenna with high gain, high isolation and low cross-polarization. In the future, the antenna can be used for MIMO radar and sparse arrays applications [21-22].

IV. CONCLUSION

A wideband ±45° dual-polarized cross dipole antenna is proposed in this paper and its impedance bandwidth is extended by parasitic elements and baluns. The proposed antenna adopts bow-tie parasitic elements, which improves the operating bandwidth of the antenna and solves the problem of parasitic elements affecting the radiation performance. The reflector improves the peak gain of the antenna and increases the stability of the antenna radiation pattern. The antenna has an impedance bandwidth of 50.4%, which can be operated at 2.24 GHz-3.75 GHz. Furthermore, the proposed antenna has a port isolation of more than 25dB and a high cross polar discrimination of better than 30 dB in the operating bandwidth. Furthermore, the antenna has a high gain, good directional radiation patterns, and front-to-back-ratio, making it promising for 5G base station applications.

REFERENCES

[1] F. Jia, S. Liao, and Q. Xue, "A dual-band dual-polarized antenna array arrangement and its application for base station antennas," in *IEEE Antennas and Wireless Propagation Letters*, vol. 19, no. 6, pp. 972-976, Jun. 2020.

[2] Y. Zhu, Y. Chen, and S. Yang, "Decoupling and low-profile design of dual-band dual-polarized base station antennas using frequency-selective surface," in *IEEE Transactions on Antennas and Propagation*, vol. 67, no. 8, pp. 5272-5281, Aug. 2019.

[3] Z. Li, J. Han, Y. Mu, X. Gao, and L. Li, "Dual-band dual-polarized base station antenna with a notch band for 2/3/4/5G communication systems," in *IEEE Antennas and Wireless Propagation Letters*, vol. 19, no. 12, pp. 2462-2466, Dec. 2020.

[4] B. Lindmark and M. Nilsson, "On the available diversity gain from different dual-polarized antennas," in *IEEE Journal on Selected Areas in Communications*, vol. 19, no. 2, pp. 287-294, Feb. 2001.

[5] Y. Cheng and Y. Dong, "Dual-broadband dual-polarized shared-aperture magnetoelectric dipole antenna for 5G applications," in *IEEE Transactions on Antennas and Propagation*, vol. 69, no. 11, pp. 7918-7923, Nov. 2021.

[6] Y. Li and Q.-X. Chu, "Coplanar dual-band base station antenna array using concept of cavity-backed antennas," in *IEEE Transactions on Antennas and Propagation*, vol. 69, no. 11, pp. 7343-7354, Nov. 2021.

[7] Y. He, Y. Li, W. Sun, and Z. Zhang, "Dual-polarized, high-gain, and low-profile magnetic current Array antenna," in I*EEE Transactions on Antennas and Propagation*, vol. 67, no. 2, pp. 1312-1317, Feb. 2019.

[8] J. Lu, Z. Kuai, X. Zhu, and N. Zhang, "A high-isolation dual-polarization microstrip patch antenna with quasi-cross-shaped coupling slot," in *IEEE Transactions on Antennas and Propagation*, vol. 59, no. 7, pp. 2713-2717, Jul. 2011.

[9] C. Ding and K.-M. Luk, "Low-profile magneto-electric dipole antenna," in *IEEE Antennas and Wireless Propagation Letters*, vol. 15, pp. 1642-1644, 2016.

[10] Q. Zhang and Y. Gao, "A compact broadband dual-polarized antenna array for base stations," in *IEEE Antennas and Wireless Propagation Letters*, vol. 17, no. 6, pp. 1073-1076, Jun. 2018.

[11] Alieldin, Y. Huang, S. J. Boyes, M. Stanley, S. D. Joseph, and B. Al-Juboori, "A dual-broadband dual-polarized fylfot-shaped antenna for mobile base stations using mimo over-lapped antenna sub-arrays," in *IEEE Access*, vol. 6, pp. 50260-50271, 2018.

[12] Y. Cui, R. Li, and P. Wang, "A novel broadband planar antenna for 2G/3G/LTE base stations," in *IEEE Transactions on Antennas and Propagation*, vol. 61, no. 5, pp. 2767-2774, May 2013.

[13] Y. Gou, S. Yang, J. Li, and Z. Nie, "A compact dual-polarized printed dipole antenna with

high isolation for wideband base station applications," in *IEEE Transactions on Antennas and Propagation*, vol. 62, no. 8, pp. 4392-4395, Aug. 2014.

[14] J. Lee, K. Lee, and P. Song, "The design of a dual-polarized small base station antenna with high isolation having a metallic cube," in *IEEE Transactions on Antennas and Propagation*, vol. 63, no. 2, pp. 791-795, Feb. 2015.

[15] Z.-Y. Zhang and K.-L. Wu, "A wideband dual-polarized dielectric magnetoelectric dipole antenna," in *IEEE Transactions on Antennas and Propagation*, vol. 66, no. 10, pp. 5590-5595, Oct. 2018.

[16] H. Huang, Y. Liu, and S. Gong, "A broadband dual-polarized base station antenna with sturdy construction," in *IEEE Antennas and Wireless Propagation Letters*, vol. 16, pp. 665-668, 2017.

[17] Z. Wang, J. Wu, Y. Yin, and X. Liu, "A broadband dual-element folded dipole antenna with a reflector," in *IEEE Antennas and Wireless Propagation Letters*, vol. 13, pp. 750-753, 2014.

[18] Y. Liu, H. Yi, F.-W. Wang, and S.-X. Gong, "A novel miniaturized broadband dual-polarized dipole antenna for base station," in *IEEE Antennas and Wireless Propagation Letters*, vol. 12, pp. 1335-1338, 2013.

[19] Z. Zhou, Z. Wei, Z. Tang, and Y. Yin, "Design and analysis of a wideband multiple-microstrip dipole antenna with high isolation," in *IEEE Antennas and Wireless Propagation Letters*, vol. 18, no. 4, pp. 722-726, April 2019.

[20] Y. Li, Z. Zhao, Z. Tang, and Y. Yin, "Differentially Fed, dual-band dual-polarized filtering antenna with high selectivity for 5G sub-6 GHz base station applications," in *IEEE Transactions on Antennas and Propagation*, vol. 68, no. 4, pp. 3231-3236, Apr. 2020.

[21] W. Shi and Y. Li, "Improved uniform linear array fitting scheme with increased lower bound on uniform degrees of freedom for DOA estimation," *IEEE Transactions on Instrumentation and Measurement*, vol. 71, 2022.

[22] W. Shi, X. Liu, and Y. Li, "ULA fitting for MIMO radar," *IEEE Communications Letters*, vol. 26, no. 9, pp. 2190-2194, 2022.

Junwei Qi received a B.S. degree in electrical information science in 2003, and M.S. and Ph.D. degrees in Communication And Information Systems from Harbin Engineering University (HEU), China, in 2008 and 2012, respectively. He is currently an Associate Professor with the Department of Information and Communication Engineering, Harbin Engineering University. His research interests include microwave antennas, wireless communication, and machine learning.

Jiakang Pan was born in Guangdong, China. He received a B.S. degree in Communication Engineering from the Changsha University of Science and Technology, Hunan, China, in 2020. He is currently pursuing an M.S. degree in Information And Communication Engineering at the Harbin Engineering University, China. His current research interest is base station antenna applications.

Yingsong Li received a B.S. degree in Electrical And Information Engineering, and an M.S. degree in Electromagnetic Field and Microwave Technology from Harbin Engineering University, 2006 and 2011, respectively. He received his Ph.D degree from both Kochi University of Technology (KUT), Japan and Harbin Engineering University (HEU), China in 2014. He is currently a Full Professor with the School of Electronic and Information Engineering of Anhui University from March 2022. He was a Full Professor in Habirn Engineering University from 2014 to 2022 and a Visiting Scholar of University of California, Davis from March 2016 to March 2017, a Visiting Professor of University of York, UK in 2018, and a Visiting Professor of Far Eastern Federal University (FEFU) and KUT. Now, he holds the Visiting Professor position of School of Information of KUT from 2018.

He is a Postdoc of Key Laboratory of Microwave Remote Sensing, Chinese Academy of Sciences from 2016 to 2021. Now, he is a Fellow of Applied computational Electromagnetics Society (ACES Fellow), and also a senior member of Chinese Institute of Electronics (CIE) and IEEE. He has authored and coauthored about 300 journal and conference papers in various areas of Electrical And Information Engineering. His current research interests include signal processing, adaptive filters, metasurface designs and microwave antennas. Li serves as an Area Editor of AEÜ-International Journal of Electronics and Communications from 2017 to 2020, and is an Associate Editor of IEEE Access, Applied Computational Electromagnetics Society Journal (ACES Journal), and Alexandria Engineering Journal and Electromagnetic Science. He is the TPC Co-Chair of the 2019 IEEE International Workshop on Electromagnetics (iWEM 2019-2020), 2019 IEEE 2nd International Conference on Electronic Information and Communication Technology (ICEICT 2019), 2019 International Applied Computational Electromagnetics Society (ACES) Symposium-China, 2019 Cross Strait Quad-regional Radio Science and Wireless Technology Conference (2019 CSQRWC), and TPC Chair of ICEICT 2021-2022. He is also a General Co-Chair of ICEICT 2020 and a General Chair of IEEE 9th International Conference on Computer Science and Network Technology (ICCSNT 2021) and ICCSNT 2022 as well as a TCP member for many international and domestic conference. He also serves as a Session Chair or Organizer for many international and domestic conferences, including the WCNC, APS, ACES-China ect. He acts as a Reviewer of numerous IEEE, IET, Elsevier and other international journals and conferences.

Guan-Long Huang received a B.E. degree in Electronic Information Engineering at Harbin Institute of Technology, Harbin, China, and his Ph.D. degree in Electrical And Computer Engineering at the National University of Singapore, Singapore. He is now a Full Professor with Foshan University, Foshan, Guangdong, China. He is also a joint-researcher with the Peng Cheng Laboratory, Shenzhen, Guangdong, China.Prior to joining the university, he worked at Shenzhen University as an Associate Professor, Nokia Solutions and Networks System Technology as a Senior Antenna Specialist, and the Temasek Laboratories at National University of Singapore as a Research Scientist from 2011 to 2020. He was a TPC member and special session organizer of several international conferences. He has authored or co-authored more than 150 papers in journals and conferences. He was the recipient of the Raj Mittra Travel Grant (2021), the Best Reviewer Award of IEEE AWPL (2019) and IEEE TAP (2020, 2021), all from IEEE Antenna and Propagation Society, and the recipient of the Young Scientist Award in 2021 from Applied Computational Electromagnetics Society, the Fok Ying-Tong Education Foundation Award in 2020 from the Ministry of Education of the People's Republic of China, and the Foundation for Distinguished Young Talents in Higher Education of Guangdong Province, China in 2017. His research interests include design and implementation of high-performance antenna arrays, base-station, and mobile RF front-end devices/antennas, millimeter-wave antenna, antenna measurement techniques, and 3-D printing technology in microwave applications.

Design and Analysis of Dual Narrow Band MIMO (DNB-MIMO) Antenna for IoT Applications

Saminathan Thiruvenkadam and Eswaran Parthasarathy

Department of Electronics and Communication Engineering
SRM Institute of Science and Technology, Chennai, Tamilnadu 603203, India
saminatt@srmist.edu.in, eswaranp@srmist.edu.in

***Abstract* –** A compact DNB-MIMO antenna design and analysis for IoT application was proposed. The antenna radiator consists of 2 L-shaaped quarter-wavelengths and inverted 7-shaped radiators with a microstrip feed line, and partial ground plane with a size of 32 × 15 mm^2. This antenna achieves a higher quality factor (Q > 10) and narrow band impedance matching at the central frequencies of 1.8 GHz and 2.4 GHz bands with approximately 8.2% and 6.2% bandwidth respectively. The suitability of the designed antenna for IoT applications is verified through the hosting device model. The proposed 4-port MIMO antenna has an overall size of 60 × 60 × 1.6 mm^3, and it is printed on an FR4 substrate. The diversity add comma such as ECC, DG, TARC, MEG, and CCL, are calculated and there values are < 0.19, 9.85 dB, < -25 dB, < -6 dB, < 0.19 bits/Hz/s, respectively, within the limits. The proposed antenna is integrated with the Zigbee module (lowercase) to analyze the performance for IoT applications at 2.4 GHz.

***Index Terms* –** DNB, DNB-MIMO, EEC, IoT, TARC, Zigbee module.

I. INTRODUCTION

The Internet of Things (IoT) is a global network of billions of physical objects that gather and send data without requiring human-to-human or human-to-computer communication. IoT implementation is found in many fields, such as smart homes, medical healthcare facilities, transportation, smart buildings, manufacturing, smart agriculture, and automation, which allows for quick decision-making based on real-time data analysis [1]. As reported in a Cisco study, between 2003 and 2020, the number of physical devices connected to the Internet increased significantly, ranging from 500 million to 50 billion [2]. Because the IoT device specifies a low data transmission rate, bandwidth needs are reduced, resulting in ultra-narrow band (UNB) modulations. Considering the above constraint, the antennas for IoT applications should be smaller and have reduced bandwidth (approximately 1MHz is also supportable for many applications), which is main challenge when designing antennas [3, 4]. It has been found that the IoT applications based on various multiband antennas [5–6], and multiband MIMO antenna designs have been investigated [7–17]. A complementary S-shape meander line has been integrated with a slotted rectangular box and capacitive load for WLAN application, showing a gain 1.347 dBi and a radiation efficiency of 79% [5]. Triangular-shaped slotted monopole antenna, E-shape monopole antenna, and two slotted patches connected to the main rectangular patch are used to achieve GSM/Bluetooth/WLAN bands [18–19]. Planar spiral loops with 4-turns for near field communication (NFC) and meander line radiator for ultra-high frequency (UHF) bands are used for IoT-based RFID reader applications [20]. Coplanar wave guide (CPW)-fed multiband patch antennas with two crossed C-shaped slots integrated into the patch and two E-shaped slots integrated into the grounded, CPW-fed slot with asymmetric T-shaped radiators are used for WLAN/WiMAX applications [21–23]. Multibranch strips a and asymmetric CPW feed with split-ring resonator are used for LTE/WWAN/WiMAX/WLAN bands [6, 24]. In [5–6], multiband antennas where implemented for GSM/Bluetooth/LTE/WLAN/WiMAX applications. However, most of the reported multiband designs have a relatively large antenna size, less gain and lower efficiency which is not suitable for IoT applications.

Furthermore, the rapid development of a multiband MIMO antenna that utilizes multiple antennas for both the transmitter and receiver will improve channel capacity, reliable radio links, and high data rates of the wireless communication system. In [7], a circularly polarized 4-port path antenna implemented without decoupling structure is used in WLAN applications. In [8], a 4-port two identical planar inverted F-antenna implemented without decoupling network was used for WLAN/LTE/4G applications. In [9], a dual mode four elements MIMO antenna design with slits placed at the four edges of the substrate were implemented with a

Submitted On: July 18, 2022
Accepted On: September 20, 2022
https://doi.org/10.13052/2022.ACES.J.370809

decoupling network for WLAN applications. In [10], a 4-port shorted patch antenna was integrated with a square-ring structure for mobile device applications. A 4-port dual-band antenna consisting of two symmetrical twisting inverted-F antenna [11]. Tunable, triangular- and C-shaped MIMO antennas with a meander line-shaped are used for LTE/ISM-2.4 GHz/5G/WiMAX bands [12–14]. For a rectangular patch antenna connected to a complementary split-ring resonator (CSRR) in the ground plane, the antenna ports are created by inserting T–shaped structure, and modified U-shaped resonator were used to reduce mutual coupling between the ports [15–17]. The literature review on multiband MIMO antennas show that the most essential frequency bands, such as LTE/GSM/WLAN/4G/WiMAXA applications, are covered. However, the most widely reported multiband MIMO designs have a relatively large antenna size, and mutual coupling between the ports are used several techniques, such as parasitic elements, metamaterials, electromagnetic band gap structure (EBG) [8, 9, 15–17].

In this article, a simple, compact, and DNB-MIMO antenna for IoT applications is presented. The designed antenna front side two radiators and backside two radiators are placed in the FR4 substrate without decoupling structure. The antenna element has a Quarter wavelength of L-shaped, and inverted 7-shaped stubs are loaded with microstrip line to achieves the dual narrow band (DNB). The designed antenna has a size of 60 × 60 × 1.6 mm^3.

II. DESIGN CONFIGURATION AND ANALYSIS OF DNB ANTENNA

In this section, we have discussed the unit element design, equivalent circuit model, surface current distribution at operating bands, hosting effect, and MIMO antenna design.

A. Design of unit element

The dimension of the proposed DNB antenna is depicted in Fig. 1. The front of the substrate is composed of an L-shaped and inverted 7-shaped radiators integrated with 50-ω feed line. The back side of the substrate optimized partial ground plane. The unit element is designed on a FR4 substrate with a thickness of 1.6 mm, $\varepsilon_r = 4.4$, tan $\delta = 0.02$ and a conductor (copper) thickness = 0.035 mm. The overall size of the proposed unit element is 32 × 15 mm^2, and the optimized dimensions are listed in Table 1. Figures 2 (a)-(b) describes the development stages of the DNB antenna. The DNB antenna is accomplished due to L-shaped and inverted 7-shaped radiators, and it can be determined by following Equation (1). The f_{o1} and f_{o2} are operating frequency due to L-shaped and inverted 7-shaped radiator respectively.

$$f_{oi} = \frac{C}{4L_{si}\sqrt{\varepsilon_{eff}}} \quad ; \; i = 1, 2, \tag{1}$$

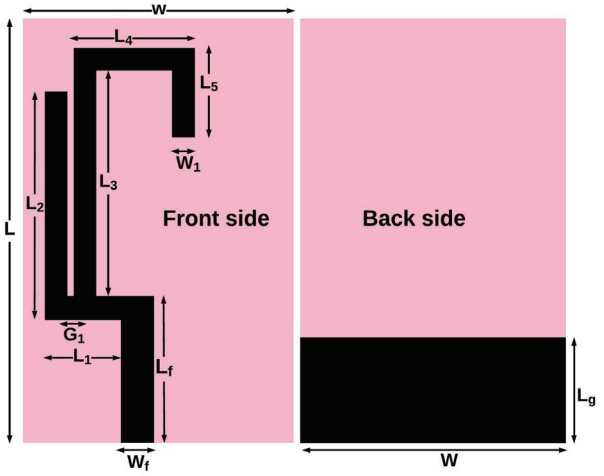

Fig. 1. Proposed DNB unit element.

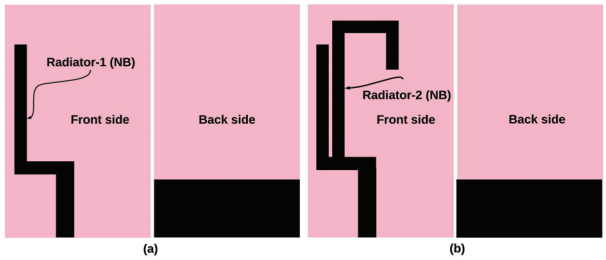

Fig. 2. Development stages of DNB antenna (a) Antenna-1, (b) Antenna-2.

where

$$\varepsilon_{eff} = \frac{\varepsilon_{r+1}}{2},$$

where 'C' is speed of light, ε_{eff} is effective dielectric constant, ε_r is dielectric constant of substrate, and L_{si} is total length of stub radiator which is responsible for operating mode.

1. Antenna-1

A quarter wavelength of L-shaped radiator-1 and an optimized partial ground plane of $L_g \times W$ is designed with a 3 mm wide microstrip feed line as shown in the Fig. 2 (a).

Table 1: Dimension of proposed unit element

Parameters	Values (mm)	Parameters	Values (mm)
L	32	L_4	9.5
L_f	11	L_5	6
L_1	5.5	W	15
L_2	19	W_f	3
L_3	20	W_1	1.5
L_g	8	G_1	0.5

$$L_{s1} = L_1 + L_2 + W_1 = \frac{\lambda_g}{4} \approx 30\,mm, \qquad (2)$$

where L_1, L_2 are length of L_{s1}, W_1 is the width of L_{s1} and λ_g is guided wavelength. The length of the L-shaped stub (L_{s1}) is calculated using length and width of the L_{s1} as mentioned in Equation (2) and it is 30 mm approximately. The antenna-1 operating frequency f_{o1} is theoretically calculated at 2.4 GHz and while the simulated operating frequency is 2.5 GHz as illustrated in Fig. 3, which is very close to theoretical value.

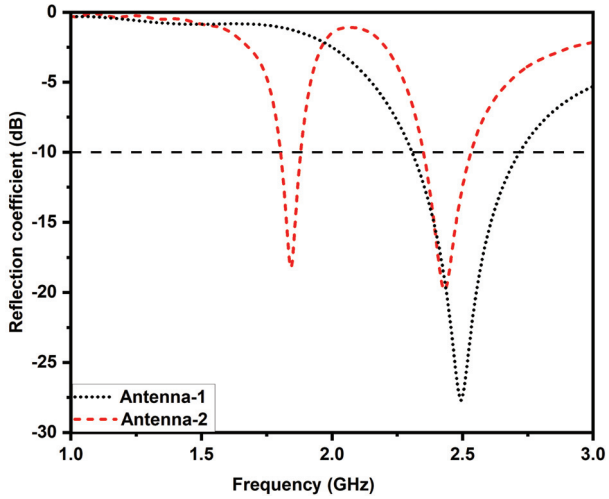

Fig. 3. Reflection coefficient (S_{11}) of designed unit element.

2. Antenna- 2:

A quarter wavelength of the inverted 7-shaped radiator-2 connected with antenna-1. Antenna-2 consists of L-shaped, inverted 7-shaped radiator connected with a feed line and an optimized partial ground plane, as shown in Fig. 2 (b).

$$L_{s2} = L_3 + L_4 + L_5 + W_1 = \frac{\lambda_g}{4} \approx 40\,mm, \qquad (3)$$

where L_{s2} is the length of the inverted 7-shaped radiator-2. L_3, L_4 and L5 are the length of L_{s2}, and W_1 is the width of L_{s2}. The length of the inverted 7-shaped stub (L_{s2}) is calculated using the length and width of the L_{s2} as mentioned in Equation (3) and it is 40 mm approximately. The radiator-2 operating frequency f_{o2} is theoretically calculated at 1.8 GHz and while the simulated operating frequency is 1.85 GHz as depicted in Fig. 3, which is very close to the theoretical value. It was found that antenna-2 operates dual-mode at 1.85 GHz and 2.45 GHz due to the inverted 7-shaped and L-shaped radiators. The reflection coefficient of the proposed antenna-2 is $<$ -10 dB at the operating bands. Further, the proposed unit element covers the GSM (1.75-1.9 GHz) and WLAN (2.34-2.55 GHz) bands.

B. Equivalent circuit of designed element

The antenna's physical mechanism is investigated using the equivalent circuit. The equivalent circuit is calculated by using proposed the antenna impedance characteristic as shown in Fig. 4. It can be seen that the impedance curve at resonance frequency real part is around 50 ω and imaginary part nearly equivalent to 0 ω. Further, the impedance curve at resonance frequency goes from high (positive) to low (negative), so a parallel RLC resonant circuit is drawn [25, 26] . The dual-band antenna consist of 7-shaped and L-shaped stub, hence the two parallel RLC circuits used to generate a dual-band through lumped equivalent circuit model are depicted in Fig. 5. The S-Parameters of the lumped equivalent circuit model is illustrated in Fig. 6. It can be observed that S-Parameters of EM model and equivalent circuit model provide identical performance.

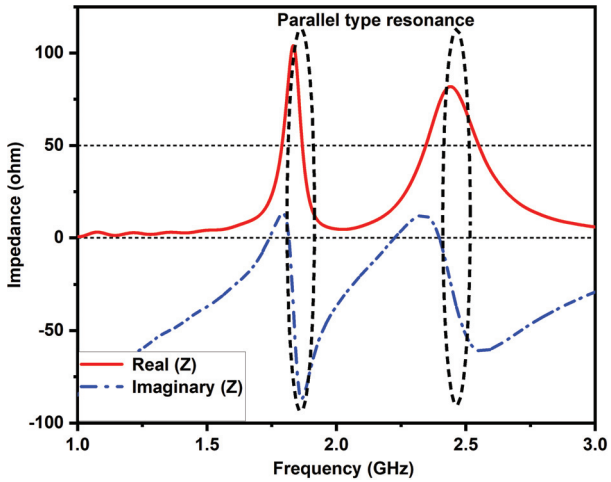

Fig. 4. Impedance characteristic of designed antenna.

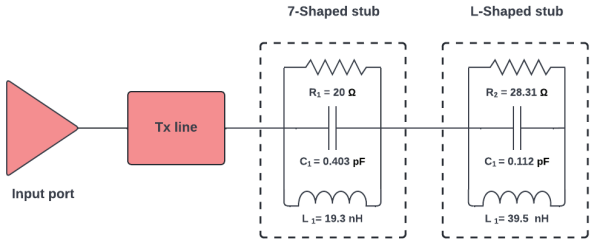

Fig. 5. Equivalent circuit model of designed antenna.

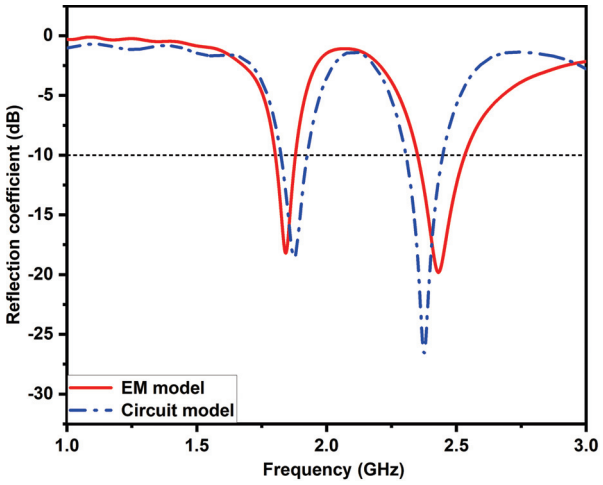

Fig. 6. Comparison of the reflection coefficient of the circuit model and the EM model.

C. Surface current distribution of DNB antenna

The surface current distribution of the proposed unit element has been investigated and illustrated in the Fig. 7. Figure 7 (a) represent the current distribution at 1.85 GHz, and the maximum current density available in radiator-2. A current density value of approximately 0.3926 A/mm is observed in radiator-2. Figure 7 (b) represent the current distribution at 2.45 GHz, and the maximum current density available in radiator-1. A current density value of approximately 0.5436 A/mm is observed in radiator-1. Hence, the surface current distribution shows that the fundamental resonance of two radiators is seen to be independent of the change in radiator length and mutual coupling between two radiators is adjusted.

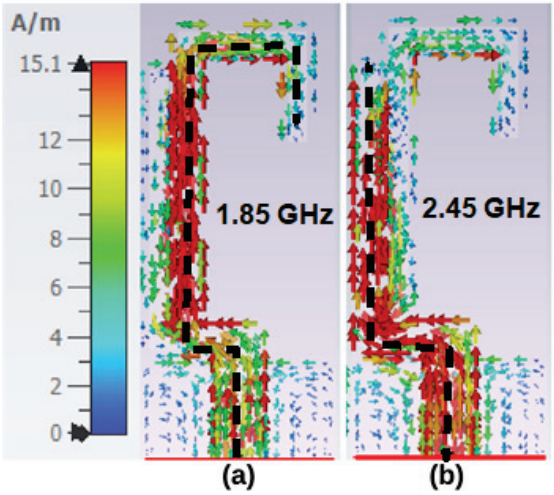

Fig. 7. Surface current distribution of the proposed unit element.

D. Hosting effect

The performance of the designed antenna is verified considering it as a host device in IoT applications. The antenna is mounted below a copper sheet size of 32 × 15 mm^2 at a distance h of 10 to 30 mm to investigate the hosting effect [27–29]. The proposed antenna reflection coefficients are investigated after being mounted in the host device, as shown in Fig. 8. It is found that the antenna can operate in dual-band whenever substrate-sized ground plane is mounted in the far near-field region. Thus, the copper sheet has less impact on the antenna performance, indicating that it will work reliably in IoT devices.

E. Design of 4-port MIMO antenna

The designed unit element is used in a MIMO system that utilizes multiple ports as transmitters and receivers to enhance the channel capacity for IoT applications. The designed has a size of 60 × 60 × 1.6 mm^3, as shown in the Fig. 9. The designed antenna was printed identically on double-sided FR4 substrate

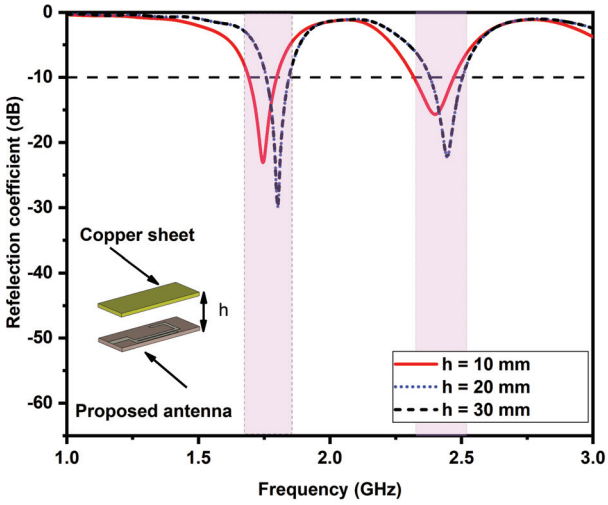

Fig. 8. Reflection coefficient of the dual band antenna with a copper plate at the distance 'h'.

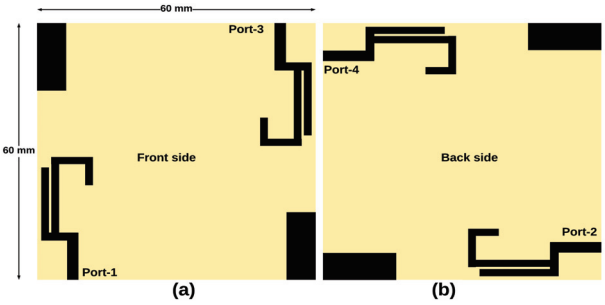

Fig. 9. Schematic diagram of designed MIMO antenna.

and each side contains two elements with an optimized partial ground plane that are connected to two other elements printed on the other side. MIMO elements are placed in an orthogonal arrangement on both sides to reduce mutual coupling between ports. The simulated reflection coefficients of the MIMO antenna are depicted in Fig. 10. It is perceived that the designed antenna achieves narrow bandwidth at center frequency of 1.8 GHz and 2.4 GHz with reflection coefficient of $<$ -10 dB.

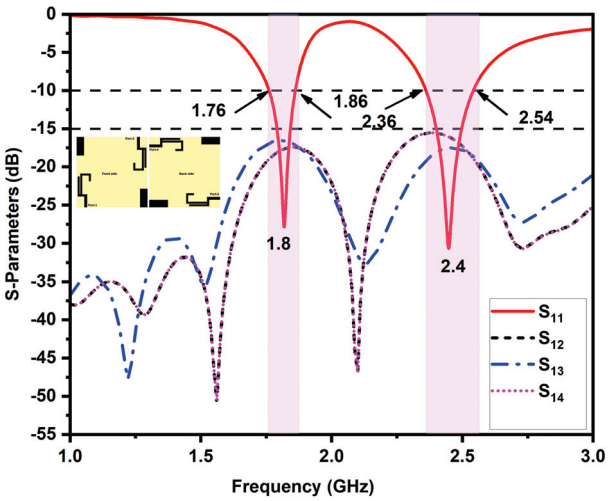

Fig. 10. S-parameters of designed antenna at Port 1 (Simulated).

The designed MIMO antenna uses double-sided placement techniques such as radiators and ground planes on both sides because it has less mutual coupling between the ports (S_{12}, S_{13}, S_{14}) as shown in the Fig. 10. It has been observed that the mutual coupling between the two ports is $<$ -15 dB over the entire operating band. In addition, the surface current distribution results of the proposed antenna used to validate the mutual coupling between the ports is depicted in Fig. 11. In this 4-port MIMO antenna design, when every port is excited and remain ports are connected to 50-ω matched the loaded, a negligible amount of current flows to other ports. Hence, the need for a decoupling structure was eliminated.

III. RESULTS AND DISCUSSIONS OF PROPOSED 4-PORT MIMO ANTENNA

The designed MIMO antenna fabricated on FR4 substrate is depicted in Fig. 12. The simulation results are experimentally verified for the antenna reflection coefficients, farfield radiation pattern, gain, and efficiency measured using the N9926A vector network analyzer and anechoic chamber.

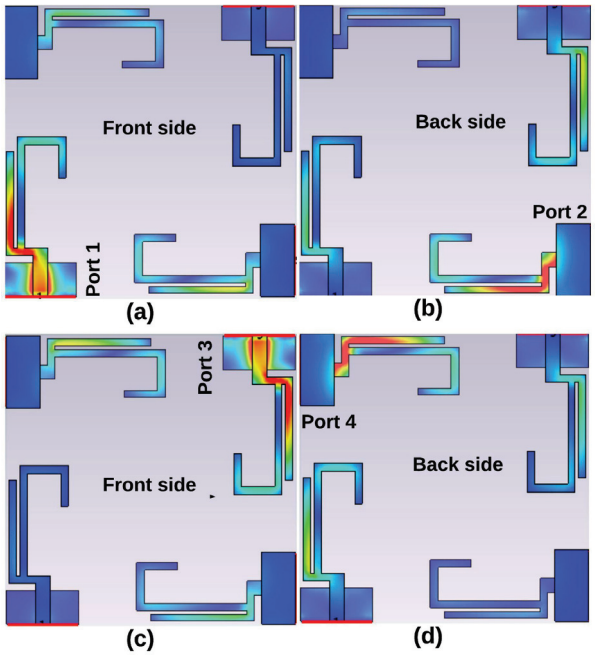

Fig. 11. Surface current distribution of designed 4-port MIMO antenna at 2.4 GHz with excitation applied at (a) Port 1, (b) Port 2, (c) Port 3, and (d) Port 4.

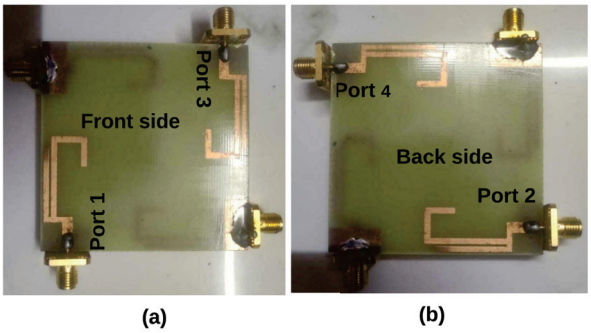

Fig. 12. Prototype of designed antenna.

A. Reflection coefficients

The proposed antenna simulated and measured reflection coefficients are illustrated in Fig. 13. The antenna is resonating dual-band center frequencies of 1.8 and 2.4 GHz and covers two different narrow bandwidth of 130 MHz (1.7–1.83 GHz) and 190 MHz (2.33–2.52 GHz) at $<$ -10 dB, which covers GSM and WLAN bands. The mutual coupling between port 1 to port 2, port 1 to port 3, and port 1 to port 4 are $<$ -20 dB at the operating bands, which shows the simulated and measured results are in good agreement.

B. Radiation pattern

The antenna radiation pattern, gain, and efficiency are measured using an anechoic chamber at port 1 and

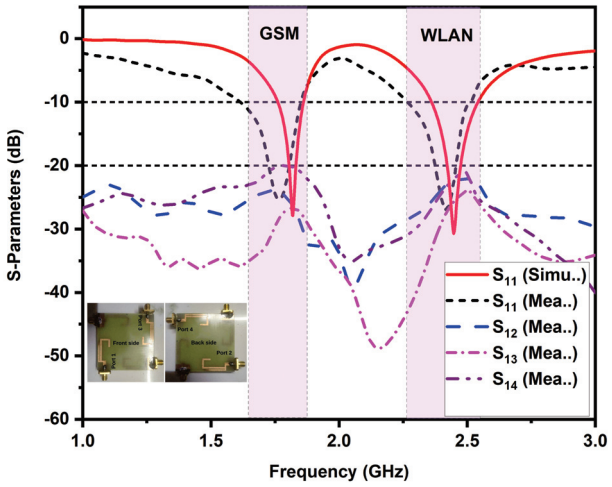

Fig. 13. S-parameters of designed antenna at Port 1 (Simulated and Measured).

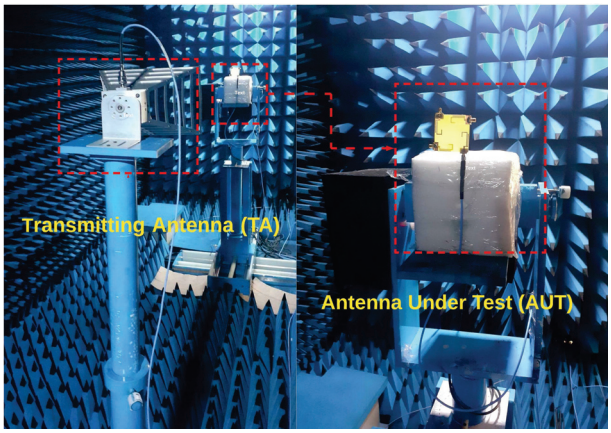

Fig. 14. Radiation pattern measurements of designed antenna in anechoic chamber.

the measurement environment is shown in Fig. 14. The coplanar and cross polarization of electric and magnetic field distribution of the designed antenna excited in port 1 is depicted in Figs. 15 (a)-(b) for 1.8 GHz and 2.4 GHz respectively.The designed antenna exhibits an omnidirectional radiation pattern in a simulation study as well as in experimental measurement. It shows good agreement among the measured values.

C. Gain and efficiency

The measured gain and total efficiency of the proposed 4-port MIMO antenna at port 1 from the far-field distance $\left[> \frac{2D^2}{\lambda}\right]$ is depicted in Fig. 16. It is perceived that the peak gain of 3.2 dBi and 4 dBi is attained in 1.8 GHz and 2.4 GHz respectively. The total efficiency measured at 1.8 GHz is 85% and at 2.4 GHz is 93.57%. Hence, the designed antenna achieves an overall peak

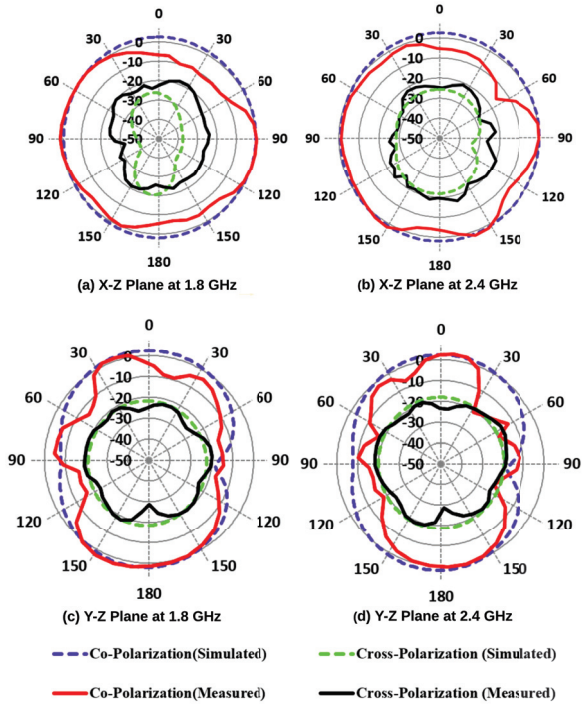

Fig. 15. Radiation patterns of designed antenna (a) X-Z plane at 1.8 GHz, (b) X-Z Plane at 2.4 GHz, (c) Y-Z plane at 1.8 GHz, (d) Y-Z Plane at 2.4 GHz.

gain $>$ 3 dbi and total efficiency $>$ 78% in the operating bands and is illustrated in Fig. 16.

D. MIMO parametric analysis of proposed antenna

The essential diversity metrics of the proposed MIMO antenna are discussed in this section using calculated and measured values of reflection coefficient, mutual coupling and radiation pattern.

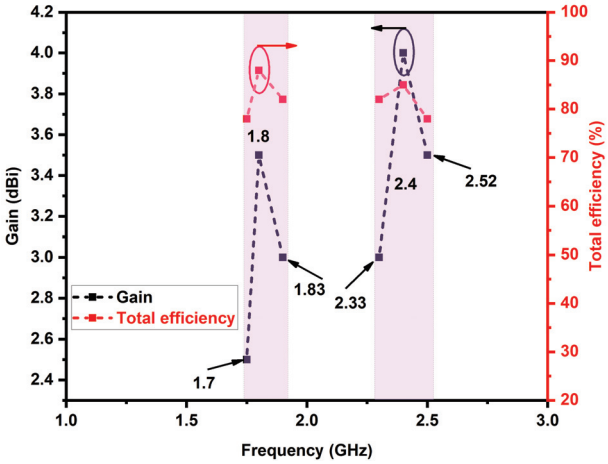

Fig. 16. Gain and total efficiency of the designed 4-port MIMO antenna is measured at Port 1.

1. ECC

Envelope correlation coefficient (ECC) is an essential metric for the MIMO antenna. It determines the correlation between the antenna radiating elements. The ECC can be computed using far-field patterns as given in Equation (4), where S_a and S_b are the electric fields radiated, and θ, φ, and dΩ are the elevation, azimuthal, and beam area, respectively. The real-time best value of ECC should be < 0.5 in all operating bands [30, 31].

$$ECC = \frac{\left|\iint[\vec{S}_a(\theta,\phi).\vec{S}_b(\theta,\phi)]\,d\Omega\right|^2}{\iint\left|[\vec{S}_a(\theta,\phi)]\right|^2 d\Omega \iint\left|\vec{S}_b(\theta,\phi)]\right|^2 d\Omega} \quad (4)$$

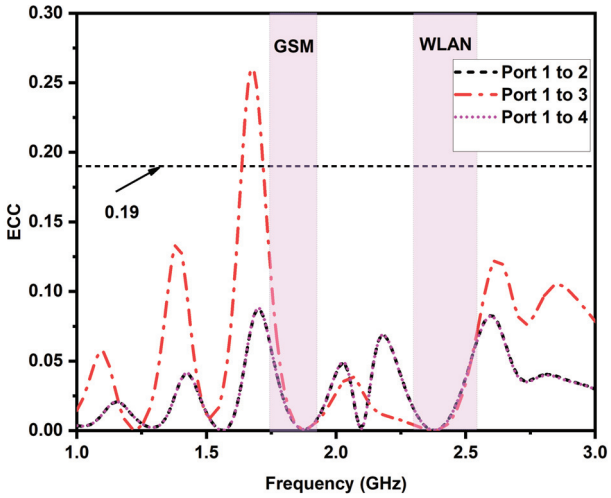

Fig. 17. ECC of designed antenna (Measured).

2. DG

The diversity gain (DG) is calculated by using farfield ECC value as given in Equation (5) [32]:

$$DG = 10\sqrt{1 - ECC^2} \quad (5)$$

3. TARC

The total active reflection coefficient (TARC) is a mathematical expression that relates to the total incident power with the total radiated power of a MIMO antenna. TARC is calculated between two-port MIMO antennas by using Equation (6). The most suitable value of TARC is expected to be < 0 to have good diverse performance for MIMO system [33].

$$\text{TARC} = \sqrt{\frac{\left(S_{11} + S_{12}e^{j\theta}\right)^2 + \left(S_{21} + S_{22}e^{j\theta}\right)^2}{2}}, \quad (6)$$

Where, θ is lies from 0 to 360°

4. CCL

The channel capacity loss (CCL) is a significant metric in MIMO performance since it grows linearly with the number of antenna elements employed under a given assumption, without affecting the transmitted power or bandwidth. MIMO channel systems suffer from capacity loss as a result of the elements' correlation. The CCL parameter is determined by the Equation (7).

$$CCL = -\log_2 det\left[\psi^R\right], \quad (7)$$

where ψ^R is correlation of the receiving antenna. The allowable limit for CCL is typically < 0.4 bps/Hz [34]. The designed MIMO antenna measured CCL is plotted in Fig. 20 and the value of CCL is < 0.19 bits/Hz/s at the resonating bands.

5. MEG

In multi-path fading situations, the mean effective gain (MEG) is defined as the ratio of the received mean power of the diversity antenna to the received mean

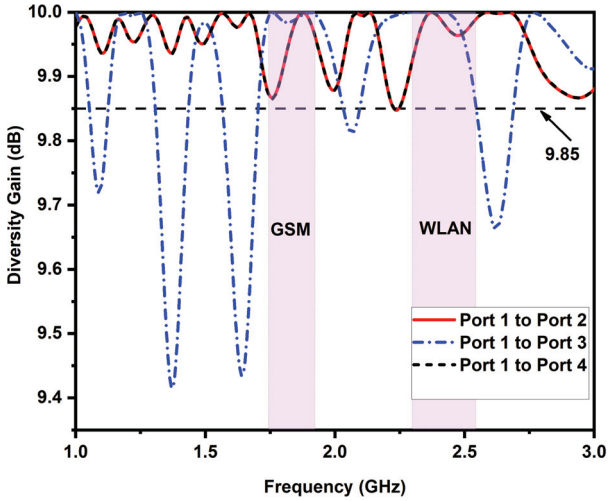

Fig. 18. DG of designed antenna (Measured).

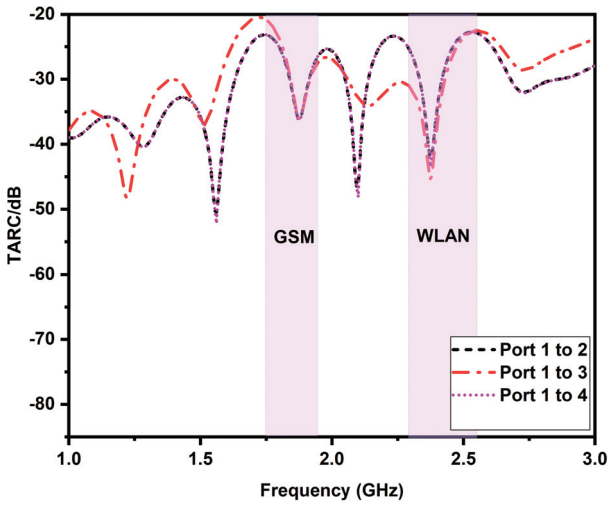

Fig. 19. TARC of designed antenna (Measured).

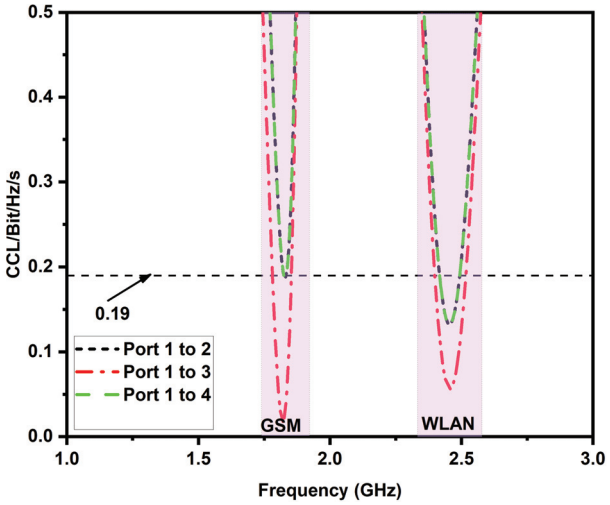

Fig. 20. CLL of designed antenna (Measured).

power of the isotropic antenna and as given in Equation (8) is used to determine S-parameters of individual ports.

$$MEG_i = 0.5\left(1 - \sum_{j=1}^{N} |S_{ij}|^2\right), \quad (8)$$

where N is number ports and i is the active port.

The computed MEG-1, MEG-2, MEG-3, MEG-4 values are given in Table 2, which is lies standard range of -3 $\leq$ MEG(dB) $<$ -12 [35, 36]. Further, the ratio of MEG1/MEG2 and MEG3/MEG4 are closed to one, which complies with the multi-path fading standard.

6. Performance comparison

The designed antenna parameters are compared with previously reported works of MIMO antenna and it is given in Table 3.

- The designed antenna structure is compact when compared to previously reported works [7, 8, 10–12, 14, 15].
- The mutual coupling of the designed antenna are better than those of [8–15] without a decoupling structure.
- This work also concentrated on the ECC and TARC of the MIMO design. The proposed antenna has a lower ECC than [7–9, 11, 12] because of the low mutual coupling characteristics. TARC was not reported in [7–13], and a lower TARC value is exhibited when compared with [14, 15] .
- The proposed MIMO antenna has been validated for real-time IoT applications.

7. Implementation of designed MIMO antenna for smart home application

Real-time implementation is carried out for IoT-based home automation applications in which the sensor modules are embedded with designed antenna operating at 2.4 GHz. The experimental setup depicted in Fig. 21 (a) consists of IoT 2040 gateway, three Zigbee modules (CC2538 kit) embedded with a designed 4-port MIMO antenna integrated with temperature, light, humidity sensors respectively.

Table 2: Measured MEG of designed antenna

Frequency (GHz)	MEG-1	MEG-2	MEG-3	MEG-4	MEG-1/MEG-2	MEG-3/MEG-4
1.8	-8.44	-8.53	-8.42	-8.51	0.989	0.989
2.4	-6.76	-6.93	-6.86	-6.84	1.002	1.002

Table 3: Comparison between proposed work and existing work

Ref.No	Size (mm^2)	M	N	BW (GHz)	MC (dB)	ECC	TARC	App
[15]	96 × 96	FR4	2	2.4-2.485	<-25	<0.4	-	WLAN
[16]	50 × 100	FR4	2	2.0-3.6	<-17	<0.3	-	IoT
[17]	46 × 20	FR4	4	2.4-2.5, 4.9-5.7	<-12	<0.3	-	WLAN
[18]	66 × 66	FR4	4	2.4-2.484, 5.7-5.8	<-12	<0.1	-	WLAN
[19]	52 × 77	FR4	2	2.4-2.48, 5.15 -5.82	<-15	<0.3	-	WLAN
[20]	80 × 54	FR4	2	1.06-1.24, 1.52-2.13, 2.19-2.63	<-14	<0.5	-	Radio/LTE/ISM
[21]	60 × 20	FR4	2	2.4-2.48, 3.4-3.6, 5.3-5.9	<-20	<0.08	-	WLAN/WiMAX
[22]	150 × 75	FR4	4	3.4-3.6	<-17.5	<0.09	<-8.6	5G
[23]	106 × 95	FR4	4	2.29-2.49,2.85-3.04, 5.61-5.80	<-17	<0.01	<-20	WLAN
PS	60 × 60	FR4	4	1.7-1.83,2.33-2.52	<-21	<0.19	<-21	IoT

M-Material, N-refers to number of radiators, BW-Bandwidth, MC-Mutual Coupling, App-Application

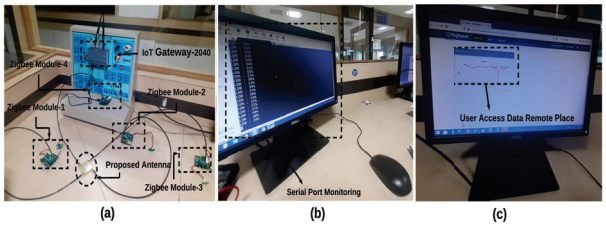

Fig. 21. Experimental setup of IoT based smart home application by using proposed antenna.

In this 4-port MIMO antenna, Port 1, Port 2, and Port 3 are connected sensor modules and Port 4 is connected to the coordinating sensor module.The Winx serial port monitor is used to display the status of the sensor data acting as a host computing device and it is shown in Fig. 21 (b). This sensor data can be used remotely using a cloud platform (ThinkSpeak) and is shown in Fig. 21 (c). The smart home application is implemented in a closed room environment. Each sensor module trasmits sensor data at a rate of 64 kbps through IoT 2040 gateway to the host computing device, which is connected to the IoT cloud . This data can be accessed from any device remotely.

IV. CONCLUSION

A multi-stub-based 4-port dual narrow band MIMO antenna is designed and fabricated and the characteristics are analyzed experimentally for IoT applications. The designed antenna exhibits dual narrow bandwidth of 1.8 GHz (1.7–1.83 GHz) and 2.4 GHz (2.33-2.52 GHz) which covers the GSM/WLAN frequency band. In the operating bands, the antenna's important metrics, such as reflection coefficient of $<$ -10 dB, mutual coupling of $<$ -21 dB between the ports, peak gain of $>$ 3 dbi, nearly omnidirectional radiation pattern, and total efficiency of $>$ 78%, are obtained experimentally. The hosting effect of proposed antenna is examined. The diversity metrics, such as ECC, DG, TARC, CCL, and MEG, are experimentally analyzed and found to be within the limits. The designed MIMO antenna performance compared with previous work shows better results. We have also demonstrated the implementation of the designed antenna in a real-time application. This proposed antenna can also be used to integrate sensor modules in a larger IoT network.

REFERENCES

[1] A. Al-Fuqaha, M. Guizani, M. Mohammadi, M. Aledhari, and M. Ayyash, "Internet of things: A survey on enabling technologies, protocols, and applications," *IEEE Communications Surveys & Tutorials*, vol. 17, no. 4, pp. 2347-2376, 2015.

[2] D. Evans, "The internet of things: How the next evolution of the internet is changing everything," *CISCO white paper*, vol. 1, no. 2011, pp. 1-11, 2011.

[3] S. Zhang, "Spectrum aanlyses of UNB modulation formats," in *2013 3rd International Conference on Consumer Electronics, Communications and Networks*, pp. 594-597, 2013.

[4] A. De, B. Roy, and A. K. Bhattacharjee, "Miniaturized dual band consumer transceiver antenna for 5G-enabled IoT-based home applications," *International Journal of Communication Systems*, p. e4840, Jul. 2021.

[5] M. S. Islam, M. T. Islam, M. A. Ullah, G. K. Beng, N. Amin, and N. Misran, "A modified meander line microstrip patch antenna with enhanced bandwidth for 2.4 GHz ISM-band Internet of Things (IoT) applications," *IEEE Access*, vol. 7, pp. 127850-127861, Sep. 2019.

[6] K. K. Naik, "Asymmetric CPW-fed SRR patch antenna for WLAN/WiMAX applications," *AEU-International Journal of Electronics and Communications*, vol. 93, pp. 103-108, Sep. 2018.

[7] E. Zhang, A. Michel, M. R. Pino, P. Nepa, and J. Qiu, "A dual circularly polarized patch antenna with high isolation for MIMO WLAN applications," *IEEE Access*, vol. 8, pp. 117833-117840, Jun. 2020.

[8] H. T. Chattha, "Compact high isolation wideband 4G and 5G multi-input multi-output antenna system for handheld and internet of things applications," *International Journal of RF and Microwave Computer-Aided Engineering*, vol. 29, no. 6, p. e21710, Jun. 2019.

[9] S. Soltani, P. Lotfi, and R. D. Murch, "A dual-band multiport MIMO slot antenna for WLAN applications," *IEEE Antennas and Wireless Propagation Letters*, vol. 16, pp. 529-532, Jul. 2016.

[10] K.-L. Wong, C.-J. Chen, and W.-Y. Li, "Integrated four low-profile shorted patch dual-band WLAN MIMO antennas for mobile device applications," *IEEE Transactions on Antennas and Propagation*, vol. 69, no. 6, pp. 3566-3571, Nov. 2020.

[11] J. Deng, J. Li, L. Zhao, and L. Guo, "A dual-band inverted-F MIMO antenna with enhanced isolation for WLAN applications," *IEEE Antennas and Wireless Propagation Letters*, vol. 16, pp. 2270-2273, Jun. 2017.

[12] B. BharathiDevi and J. Kumar, "Small frequency range discrete bandwidth tunable multiband MIMO antenna for radio/LTE/ISM-2.4 GHz band applications," *AEU-International Journal of Electron-*

ics and Communications, vol. 144, p. 154060, Feb. 2022.

[13] S. Pandit, A. Mohan, and P. Ray, "Compact frequency-reconfigurable MIMO antenna for microwave sensing applications in WLAN and WiMAX frequency bands," *IEEE sensors letters*, vol. 2, no. 2, pp. 1-4, Apr. 2018.

[14] A. T. Z. Moses, N. Moses, and D. K. Janapala, "An electrically small 4-port self-decoupled MIMO antenna pairs operating in n78 5G NR band for smartphone applications," *AEU-International Journal of Electronics and Communications*, p. 154082, Feb. 2021.

[15] M. Aminu-Baba, M. K. A. Rahim, F. Zubir, A. Y. Iliyasu, K. I. Jahun, M. F. M. Yusoff, M. M. Gajibo, A. A. Pramudita, and I. K. C. Lin, "A compact triband miniaturized MIMO antenna for WLAN applications," *AEU-International Journal of Electronics and Communications*, vol. 136, p. 153767, Jul. 2021.

[16] H. Yon, M. A. Aris, N. H. A. Rahman, N. M. Nasir, and H. Jumaat, "A Design of Decoupling Structure MIMO Antenna for Mutual Coupling Reduction in 5G Application," in *2019 International Symposium on Antennas and Propagation (ISAP)*, pp. 1-3, 2019.

[17] A. Iqbal, A. Altaf, M. Abdullah, M. Alibakhshikenari, E. Limiti, and S. Kim, "Modified U-shaped resonator as decoupling structure in MIMO antenna," *Electronics*, vol. 9, no. 8, p. 1321, Aug. 2020.

[18] M. Dehmas, A. Azrar, F. Mouhouche, K. Djafri, and M. Challal, "Compact dual band slotted triangular monopole antenna for RFID applications," *Microwave and Optical Technology Letters*, vol. 60, no. 2, pp. 432-436, Feb. 2018.

[19] S. Katoch, H. Jotwani, S. Pani, and A. Rajawat, "A compact dual band antenna for IOT applications," in *2015 International Conference on Green Computing and Internet of Things (ICGCIoT)*, pp. 1594-1597, 2015.

[20] A. Romputtal and C. Phongcharoenpanich, "IoT-linked integrated NFC and dual band UHF/2.45 GHz RFID reader antenna scheme," *IEEE Access*, vol. 7, pp. 177832-177843, Dec. 2019.

[21] A. M. Saadh and R. Poonkuzhali, "A compact CPW fed multiband antenna for WLAN/INSAT/WPAN applications," *AEU-International Journal of Electronics and Communications*, vol. 109, pp. 128-135, Sep. 2019.

[22] Chandan, "Truncated ground plane multiband monopole antenna for WLAN and WiMAX applications," *IETE Journal of Research*, pp. 1-6, Jan. 2020.

[23] K.-L. Wong, H.-J. Chang, C.-Y. Wang, and S.-Y. Wang, "Very-low-profile grounded coplanar waveguide-fed dual-band WLAN slot antenna for on-body antenna application," *IEEE Antennas and Wireless Propagation Letters*, vol. 19, no. 1, pp. 213-217, Dec. 2019.

[24] Ming-An Chung, "A miniaturized triple band monopole antenna with a coupled branch strip for bandwidth enhancement for IoT applications," *Microwave and Optical Technology Letters*, vol. 60, no. 9, pp. 2336-2342, Sep. 2018.

[25] S. Luo, D. Wang, Y. Chen, E. Li, and C. Jiang, "A compact dual-port UWB-MIMO antenna with quadruple band-notched characteristics," *AEU-International Journal of Electronics and Communications*, vol. 136, p. 153770, Jul. 2021.

[26] L. S. Yahya, L. S. Yahya, and K. H. Sayidmarie, "Dual-band folded monopole MIMO antennas with enhanced isolation," *Applied Computational Electromagnetics Society (ACES) Journal*, pp. 1569-1578, Dec. 2021.

[27] U. Bashir, K. R. Jha, G. Mishra, G. Singh, and S. K. Sharma, "Octahedron-shaped linearly polarized antenna for multistandard services including RFID and IoT," *IEEE Transactions on Antennas and Propagation*, vol. 65, no. 7, pp. 3364-3373, May 2017.

[28] N. K. Maurya and R. Bhattacharya, "Design of compact dual-polarized multiband MIMO antenna using near-field for IoT," *AEU-International Journal of Electronics and Communications*, vol. 117, p. 153091, Apr. 2020.

[29] S. Thiruvenkadam, E. Parthasarathy, S. K. Palaniswamy, S. Kumar, and L. Wang, "Design and performance analysis of a compact planar MIMO antenna for IoT applications," *Sensors*, vol. 21, no. 23, p. 7909, Nov. 2021.

[30] M. S. Sharawi, "Printed multi-band MIMO antenna systems and their performance metrics [wireless corner]," *IEEE Antennas and Propagation Magazine*, vol. 55, no. 5, pp. 218-232, 2013.

[31] P. Prabhu and S. Malarvizhi, "Compact dual-band hybrid-fractal MIMO system for UMTS and LTE mobile applications," *Applied Computational Electromagnetics Society (ACES) Journal*, pp. 135-140, Jan. 2019.

[32] Z.-J. Tang, J. Zhan, B. Zhong, L. Cheng, and G. Zuo, "Design of a coplanar UWB-MIMO ground antenna based on the theory of characteristic modes," *Progress in Electromagnetics Research C*, vol. 117, pp. 221-237, 2021.

[33] J. Kulkarni, A. Desai, and Chow-Yen-Desmond Sim, "Two port CPW-fed MIMO antenna with wide bandwidth and high isolation for future wire-

less applications," *International Journal of RF and Microwave Computer-Aided Engineering*, p. e22700, Aug. 2021.

[34] K. Srivastava, S. Kumar, B. K. Kanaujia, S. Dwari, H. C. Choi, and K. W. Kim, "Compact eight-port MIMO/diversity antenna with band rejection characteristics," *International Journal of RF and Microwave Computer-Aided Engineering*, vol. 30, no. 5, p. e22170, May 2020.

[35] A. A. Khan, M. H. Jamaluddin, J. Nasir, R. Khan, S. Aqeel, and J. Saleem, "Design of a dual-Band MIMO dielectric resonator antenna with pattern diversity for WiMAX and WLAN applications," *Progress in Electromagnetics Research M*, vol. 50, pp. 65-73, 2016.

[36] D. H. Sadek, H. A. Shawkey, and A. A. Zekry, "Multiband triple L-arms patch antenna with diamond slot ground for 5G applications," *Applied Computational Electromagnetics Society (ACES) Journal*, pp. 302-307, Mar. 2021.

T. Saminathan received his B.E. degree in Electronics and Communication Engineering from King College of Engg, Tamil Nadu, India (affiliated to Anna University, Chennai) in 2008 and M.Tech degree in Embedded System and Technology from SRM University, Tamil Nadu, India, in 2012. Presently, he is working as an assistant professor in SRMIST and pursuing a Ph.D. degree in the Department of Electronics and Communication Engineering at SRMIST, Chennai, India. His research interests include monopole antenna design, multi-band antennas, and MIMO antenna design.

P. Eswaran received his Bachelor degree in Electronics and Telecommunication Engineering from the Institute of Engineers (India) in 2000, Master's in Mechatronics in 2003 from Madras Institute of Technology (India), and Ph.D. in Electronics and Communication Engineering from SRM University in 2014. He currently works as Professor in Department of Electronics and Communication Engineering at SRMIST (Formerly known as SRM University). His areas of interest are MEMS, VLSI, Device Modeling, EV and PV systems, embedded systems and Industry 4.0. He has published over 30 reviewed international journal/conference papers, and two Indian patents. He has served as a reviewer for peer reviewed journals. He is also Fellow Member of IE (India), Life Member of IETE, and ISTE professional bodies.

Fractal Sectoral Monopole Antenna for UWB Band Applications

A. H. Majeed[1] and K. H. Sayidmarie[2]

[1]Department of Information and Communication Engineering
College of Information Engineering
Al-Nahrain University, Baghdad, Iraq
asmaahameed37@ yahoo.co.uk

[2]College of Electronic Engineering
Ninevah University, Mosul, Iraq
kh.sayidmarie@uoninevah.ed.iq

Abstract – This paper proposes a fractal monopole antenna based on a sectoral-shaped patch. To improve the gain of the proposed antenna over a larger bandwidth, the matching was enhanced by attaching two rectangular stubs to the feeding line. The antenna, which is built on an FR4 epoxy substrate with ε_r =4.3 and a loss tangent of 0.018 has a compact size of 28 mm×31 mm×1.6 mm. The antenna covers the UWB range and extends to about the 22 GHz frequency, as well as offers omnidirectional radiation patterns. The optimized configuration was fabricated and tested. The impedance bandwidth of the proposed antenna is about 155% with a reflection coefficient better than −10 dB and has a maximum gain of nearly 4 dBi with a relatively stable omnidirectional radiation pattern.

Index Terms – bandwidth extension, fractal antennas, monopole antennas, stubs, UWB.

I. INTRODUCTION

Since the FCC has designated the frequency band (3.1–10.6 GHz) for unlicensed commercial UWB communications in the United States [1], extensive research has gone into the development of UWB antennas. With the development of many communication systems, larger bandwidths are still needed. The microstrip printed antenna can provide such desired features if the problem of the narrow bandwidth is solved. Traditional geometrical shapes such as triangular, circular, and elliptical disc monopoles were used in many proposed designs of the UWB-printed antennas [2–5]. The aim was to use different shapes to obtain enough bandwidth that may be able to go above and beyond the UWB requirement. The dipole type of antenna has also been proposed and investigated aiming to provide UWB properties, where circular, square, triangular, and other shapes for the two arms have been employed [6, 7]. Most of the presented design methods were based on choosing a certain shape followed by some sort of trial and error procedures to obtain enhanced performance. Initial designs are then developed by customizing corners, slots, slits, or parasitic parts to obtain the desired features. One example was a circular disk monopole that was developed by cutting a small sector to form what was called a packman-shaped antenna [8]. Another example was the use of a circular patch with a sawtooth-like circumference for the extension of the bandwidth and size reduction [9]. A rectangular monopole antenna was developed by cutting rectangles and adding strips to improve the bandwidth [10]. The deployment of advanced simulation software packages like CST and HFSS has aided the above search for the desired antenna characteristics. The influence of many of the antenna parameters on the antenna characteristics is explored aiming to achieve an optimized design. However, there exist some more efficient approaches for designing UWB antennas such as the self-complementary geometries [11, 12].

A large impedance bandwidth can be achieved by exploiting the concept of fractal geometry to obtain a multiband performance covering a wider band [13, 14]. Fractal geometry is a type of geometry that uses rules to repeat and scale a specific shape. The repeated shapes produce a multi-resonance operation in which the resonance frequencies are inversely proportional to the sizes [15]. A tree-shaped monopole, created by arranging several squares or triangles, was proposed in [16] for the enhancement of the antenna bandwidth. The concept was further developed in [17] by proposing the flower fractal geometry, which is inspired by the geometry of flowers where the shape of the petal is scaled, rotated, and repeated a few times. The antenna achieved bandwidth exceeding the UWB range. The shape repetition results in a multi resonance that leads to a wide bandwidth as

Submitted On: June 12, 2021
Accepted On: June 20, 2022

https://doi.org/10.13052/2022.ACES.J.370810

compared to the single monopole antennas or the dipole antenna [11, 12]. In [14, 16] the scaling factor can be chosen by the designer to achieve the desired performance. Thus, giving more flexibility as compared to the conventional fractals where the scale factor is fixed as in Sierpinski fractals [13] and Koch fractals [18]. Therefore, the multi-resonance frequencies manifest themselves individually instead of forming a unified band.

This paper proposes a fractal monopole antenna based on a sectoral-shaped patch that is scaled down, rotated then repeated to form a fractal geometry. Two or three iterations can be employed to achieve the required bandwidth. To provide proper matching for higher frequencies, two stubs are attached to each side of the feeding line. Thus, the proposed fractal antenna covered the UWB range and further to the 22 GHz frequency. In section II, the proposed fractal is presented, while section III describes the antenna configuration. In section IV, the parametric investigations are used to improve the matching and expand the bandwidth. Section V explains how to improve matching in the upper half of the operating band. In section VI, the antenna's fabricated prototype is tested, and in section VII, the achieved antenna characteristics are compared to those of other antennas. The conclusions are listed in section VIII.

II. THE PROPOSED FRACTAL GEOMETRY

The proposed fractal employs the shape of a circular sector, which is iterated by scaling down and repetitions many times as required. The first iteration is represented by two adjacent sectors that are symmetrically placed with respect to the axis of symmetry, as shown in Fig 1. Each of the two sectors is defined by three points;

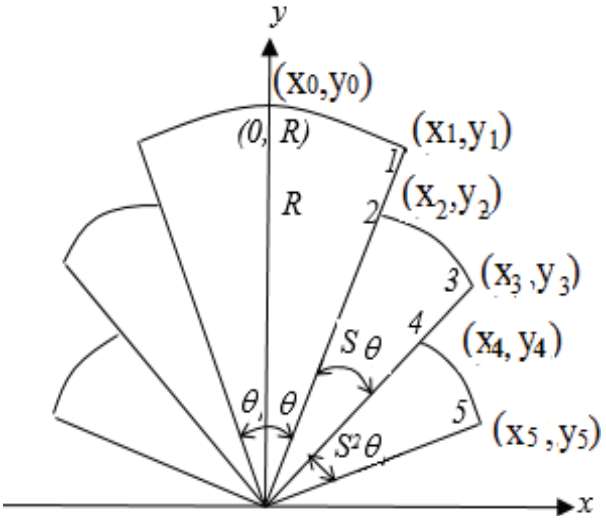

Fig. 1. Coordinates of the various corners of the circular sectors for generating the proposed fractal.

the center of the circle, which is placed at the origin, and two corners points (x_0, y_0), (x_1, y_1), which are given by:

$$x_0 = 0, \tag{1.a}$$

$$y_0 = R_0, \tag{1.b}$$

$$x_1 = R_0 \sin(\theta_0), \tag{2.a}$$

$$y_1 = R_0 \cos(\theta_0). \tag{2.b}$$

where R_0 is the radius of the sector and θ_0 is the subtended angle, which is measured from the axis of symmetry (Y-axis). The 1^{st} iteration comprises a scaling of the radius and the angle by a factor S, resulting in a new radius of $R_1 = SR_0$, and subtended angle of $\theta_1 = S\theta_0$. The generated sector is placed adjacent to either of the former ones, with their center at the origin. The corners of the new sector on the right side are given by:

$$x_2 = S\,R_0\,sin\,(\theta_0)\,, \tag{3.a}$$

$$y_2 = S\,R_0\,cos\,(\theta_0)\,, \tag{3.b}$$

$$x_3 = S\,R_0\,sin\,(\theta_0 + S\,\theta_0)\,, \tag{4.a}$$

$$y_3 = S\,R_0\,cos\,(\theta_0 + S\,\theta_0)\,. \tag{4.b}$$

Thus, at the nth iteration, the parameters of the sector can be described by:

$$R_n = R_0 S^n \qquad n = 1,2,3 \tag{5.a}$$

$$\theta_n = \theta_0(1 + \Sigma_{i=1}^{n} S^i) \qquad n = 1,2,3. \tag{5.b}$$

The fractal geometries for the first three iterations were plotted by a MATLAB program, and are shown in Fig. 2.

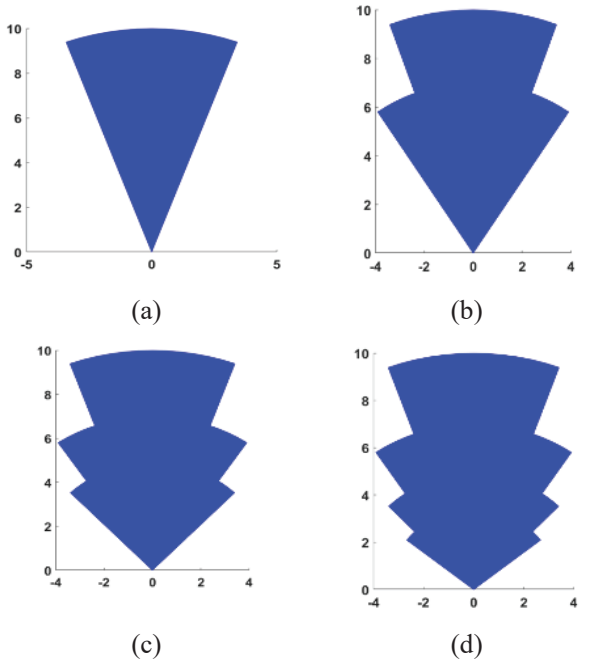

Fig. 2. The geometries of the proposed fractal for the iterations; 0, 1, 2, and 3, corresponding to one, two, three, and four sectors.

III. ANTENNA DESIGN

Figure 3 depicts the general configuration of the proposed fractal monopole UWB antenna. The design is based on the 2^{nd} iteration of the fractal geometry that is described in section II and shown in Fig. 2 (c). In this design, the scaling factor S is chosen to be smaller than unity, and the total angle θ_2 is less than 90^o so that the radiating patch (monopole) does not overlap the ground plane. The prototype antenna is built on a 28 × 31 mm^2

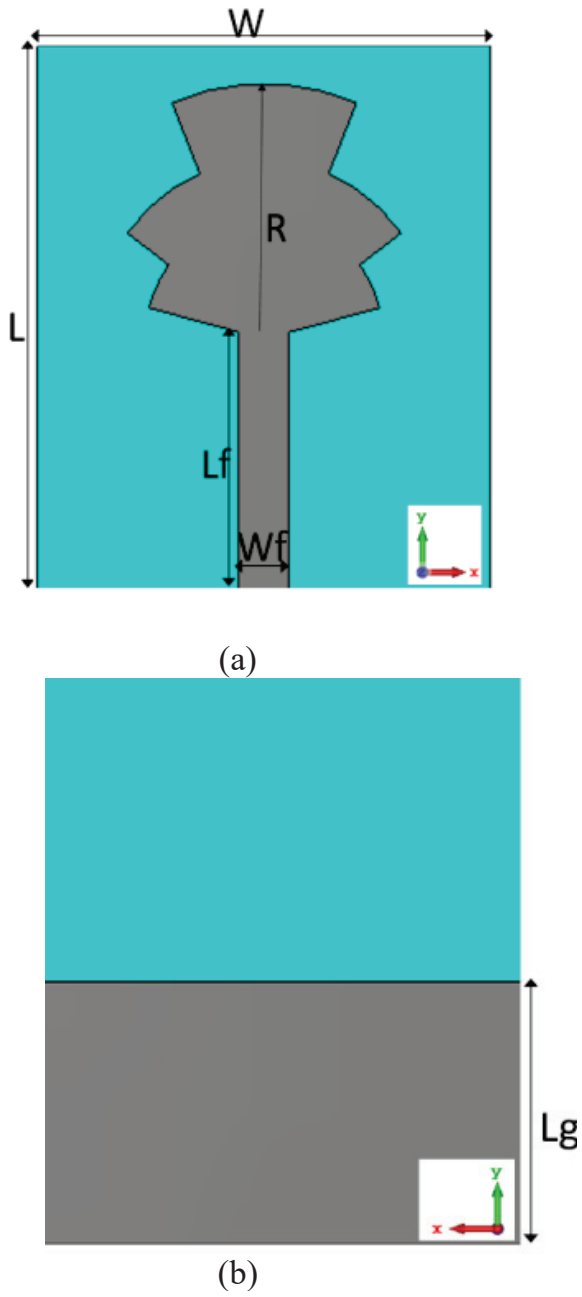

Fig. 3. The configuration of Antenna I; (a) Front view, (b) back view.

FR4 substrate with ε_r = 4.3, loss tangent of 0.018, and 1.6 mm thickness. A microstrip feeding line is used to excite the antenna assembly. The length and width of the microstrip lines were determined using the empirical formulas in [19], resulting in a length of 15.5 mm and 3.1 mm width to insure a 50 Ω line impedance.

The Computer Simulation Technology (CST) version 2018, which focuses on a finite integration technique (FIT), is used to study the effect of various parameters on the antenna characteristics, thus optimizing the structure of the proposed fractal monopole form antenna (Antenna-I). We need to describe the surfaces in the CST simulations using equations in terms of R, S, and θ_0 so that changing the shape in the parametric analysis is much simpler.

The conducting ground plane on the other side of the substrate has a length of *Lg*=15.2 mm, and thus it covers only a portion of the microstrip feed line. The same metallic material (copper) was used to model the fractal-shaped patch and the ground plane.

IV. SIMULATION AND PARAMETRIC ANALYSIS

The impact of various parameters on the response of the proposed Antenna-I is discussed in this section. The following parameters must be optimized:

- The radius R_0 of the sector,
- The angle l_0 (in radians),
- The scale factor S.

On the other hand, the other parameters of Antenna-I are kept constant. The antenna performance is initially characterized in terms of the reflection coefficient as shown in Figs. 4–6. The following paragraphs address the effects of the sector radius R_o, scale factor S, and angle θ_0 on the reflection coefficient response.

Figure 4 shows the variation of the reflection coefficient with frequency for various patch radii, R_0, with S= 0.64 and θ_0 = 0.78 radians. The radius R_0 has a moderate impact on the lower and upper frequencies, as well as on matching, as shown in Fig. 4. It was found that the best patch radius is R_0 =13.9 mm.

Figure 5 depicts the fluctuation of the reflection coefficient (S_{11}) with frequency for different values of the scale factor S with R_0 = 13.9 mm and θ_0 = 0.78 radians. The scale factor S has a small effect on the lower frequencies, but it has a significant impact on the reflection coefficient at the upper frequencies. With better matching at lower values of S, the upper limit of frequency decreased as S increased. The best scale factor was found to be S = 0.65, which results in a larger bandwidth.

Figure 6 displays the simulated reflection coefficient as a function of frequency for various values of the initial angle θ_0. The angle θ_0 has a minor impact on the lower

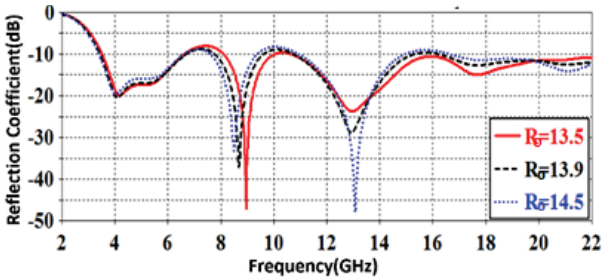

Fig. 4. Simulated Antenna-I reflection coefficient as a function of frequency for various patch radii R_o.

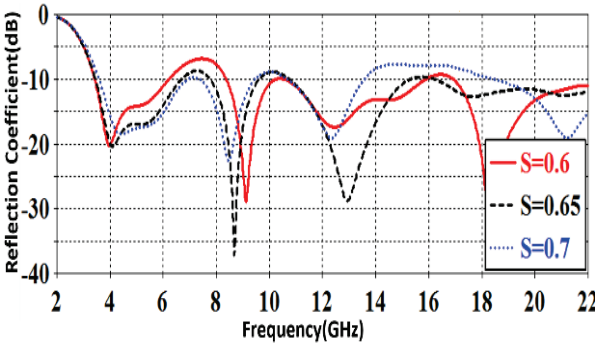

Fig. 5. Simulated Antenna-I reflection coefficient as a function of frequency for different scale factors *S*.

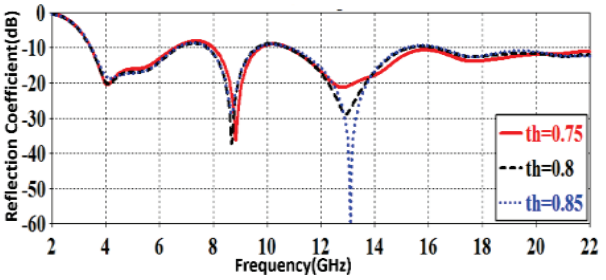

Fig. 6. Simulated Antenna-I reflection coefficient as a function of frequency for various angles θ_0.

and upper frequencies, but it improves matching as the angle θ increases. In terms of reflection coefficient and bandwidth, it was found that the case θ_0 = 0.8 radians provides a better response. The scale factor was set to 0.65 and radius R_0 was held at 13.9 mm.

Table 1 shows the optimized parameters for Antenna-I. Figure 7 (a) depicts the optimized Antenna-I simulated reflection coefficient as a function of frequency. This figure shows that Antenna-I has a reflection coefficient ≤ -10 dB at 4.09 GHz, 8.7 GHz, 12.9 GHz, 17.6 GHz and 20.9 GHz of -20.3 dB, -36.7 dB, -28.8 dB, -12.7 dB and -12.5 dB respectively. Figure 7 (b) displays the optimized antenna realized gain versus frequency. A maximum gain of 4.62 dBi

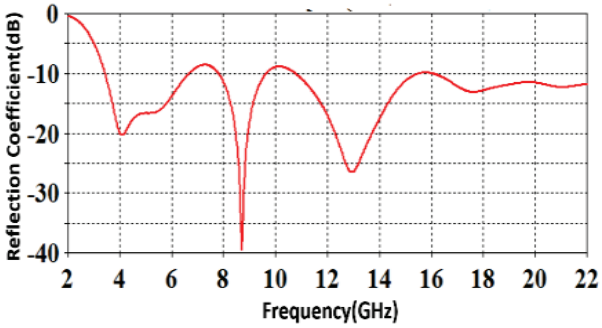

Fig. 7. (a). Simulated reflection coefficient for optimized Antenna-I.

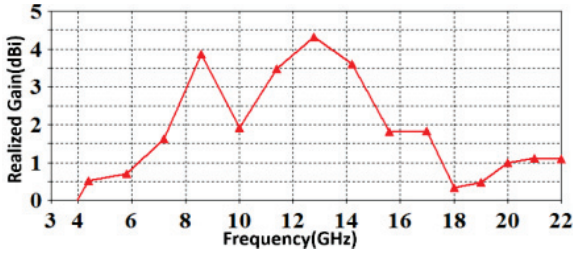

Fig. 7. (b). Simulated realized gain for optimized Antenna-I.

Table 1: Optimized parameters of the Antenna-I

Parameter	Value (mm)	Parameter	Value (mm)
W	28	*Lg*	15.2
L	31	*R*	13.9
t	1.6	*S*	0.65
Lf	15.5	θ	0.8 radian
Wf	3		

was achieved in the direction of theta =90^o across the band of interest. However, the gain drops at both sides of the operation band.

V. IMPROVED PERFORMANCE

A double-stub matching network was added on each side of the feed line of Antenna-I to produce the developed design Antenna-II, as shown in Fig. 8, aiming to achieve better performance in terms of matching, gain, and impedance bandwidth. The CST program is also used to evaluate and refine the Antenna-II structure to obtain better dimensions of the double-stub matching network, which resulted in improved performance for the Antenna-II.

Figure 9 demonstrates the variation of Antenna-II simulated reflection coefficient versus frequency for various left stub lengths (*x*). According to practical experience, the stub length should be close to 1/4 the effective

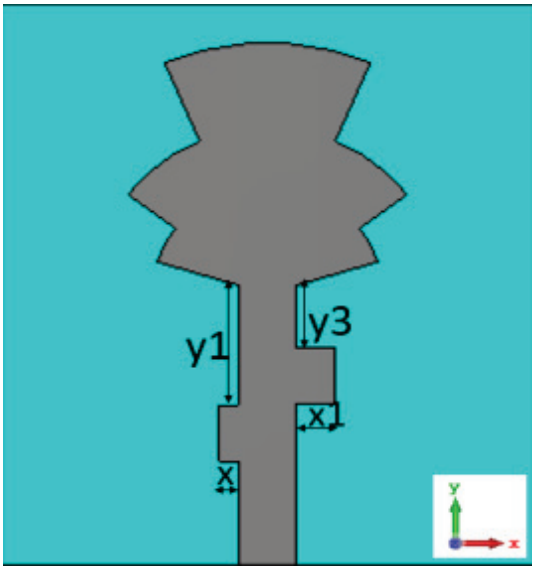

Fig. 8. The configuration of the proposed fractal patch monopole antenna (Antenna-II) with the added double-stub network.

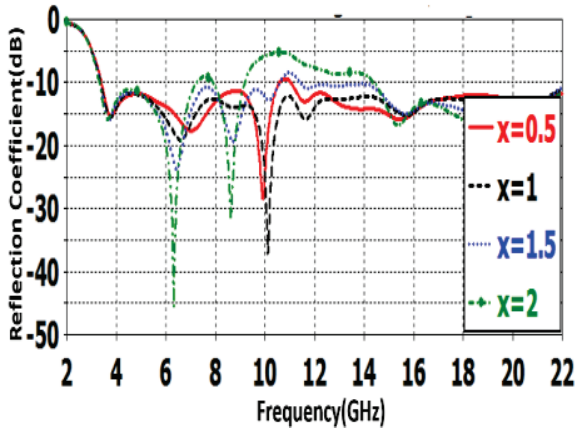

Fig. 9. Antenna-II simulated reflection coefficient versus frequency curves with various x.

wavelength [19], and the optimization of the stub length should begin from there.

The variation of the Antenna-II simulated reflection coefficient with frequency for various stub lengths of the right stub (x_1) is shown in Fig. 10. In terms of matching and impedance bandwidth, it is obvious from this figure that x_1=2.0 mm provides the best performance.

Figure 11 presents the variation of the Antenna-II simulated reflection coefficient versus frequency for various separations of the left stub from the feeding line upper end (y_1). It can be seen from this figure that increasing y_1 has no impact on the lower edge of the frequency band but it causes an improvement in the reflection coefficient with the increase in frequency.

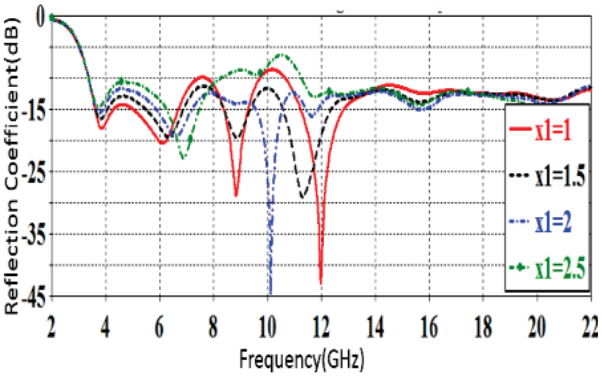

Fig. 10. Antenna-II simulated reflection coefficient versus frequency curves for various values of x_1.

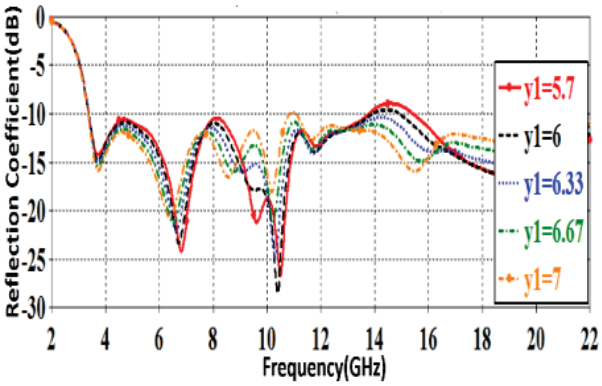

Fig. 11. Antenna-II simulated reflection coefficient versus frequency curves for various values of y_1.

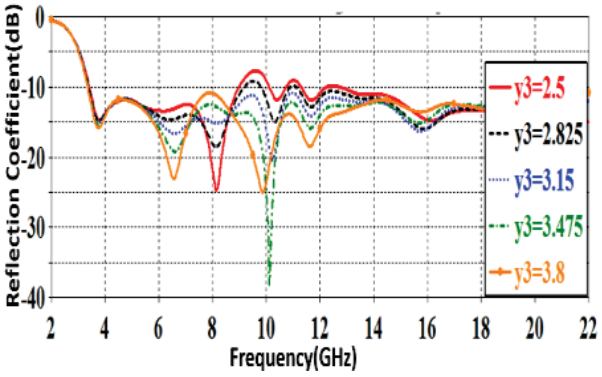

Fig. 12. Antenna-II simulated reflection coefficient versus frequency curves with various y_3.

The effect of different separations of the right stub (y_3) from the feeding line upper end of Antenna-II on the reflection coefficient is shown in Fig. 12. It is clear that increasing y_3 has no impact on the frequency band lower edge but it causes an improvement in the reflection coefficient for frequencies greater than 8.5 GHz.

VI. ANTENNA FABRICATION AND RESULTS

Table 2 lists the optimum parameters for the double stub matching network (x, x_1, y_1, and y_3) of Antenna-II, while the other parameters of Antenna-II are left unchanged as they are in Antenna-I. The low-cost antenna is small and simple to fabricate using traditional PCB techniques. The proposed Antenna-II was fabricated as shown in Fig. 13. The antenna was tested by a vector network analyzer (Rode and Schwarz ZVL13) operating up to 13.6 GHz. Figure 14 shows the measured reflection coefficient, compared to the simulation results, where the −10 dB band extends from 3.3 GHz to the upper frequency measurable by the VNA. As a higher frequency analyzer was not available to the authors, the fullly achieved bandwidth cannot be confirmed. It can be seen that the antenna bandwidth extends beyond the UWB, but the simulated results of 20 GHz were not confirmed. Three regions of very low reflection coefficient can be seen around the frequencies; 4.3 GHz, 6.5 GHz, and 10 GHz. These frequencies are proportional to the numbers 0.43: 0.65: 1. These figures are in proportion to S^2: S:1, i.e., to the fractal scale factor of 0.64 which was used in the design of the antenna (see Table 1). Therefore, the designer can control the multi-resonance frequencies by choosing a proper value for the scale factor.

Figure 15 shows a comparison between Antenna-I and Antenna-II simulated gain versus frequency. It is noted from the figure that the addition of the double stubs improves the gain for frequencies above 16 GHz. The gain response becomes with fewer fluctuations. However, the gain drops from its former values in the frequency range of 10.2 GHz to 15.8 GHz. The use of the two stubs has resulted in reducing the ripples in the gain response.

Figure 16 shows the simulated 3-dimensional far-field radiation patterns for Antenna-I and Antenna-II for various frequencies. The two antennas show almost uniform radiation in the horizontal plane, (the plane perpendicular to the antenna), but antenna-II shows better coverage at frequencies above 8.6 GHz. The radiation from Antenna-I exhibits splitting when the frequency is above 9 GHz, but the pattern of Antenna-II keeps its uniformity at frequencies higher than 9 GHz. Thus antenna-II shows better radiation pattern stability with frequency as compared to Antenna-I.

Table 2: Optimized parameters for x, x_1, y_1, and y_3 of the Antenna-II

Parameter	Value (mm)	Parameter	Value (mm)
x	1.25	x_1	2
y_1	6.7	y_3	3.47

Fig. 13. Photographs of the fabricated Antenna-II.

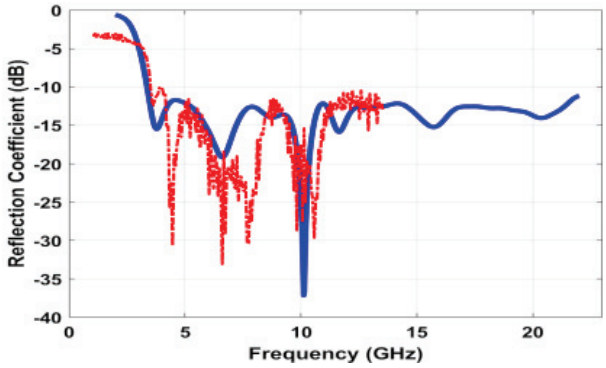

Fig. 14. Comparison between Antenna-II simulated (---) and measured (—-) reflection coefficient as a function of frequency.

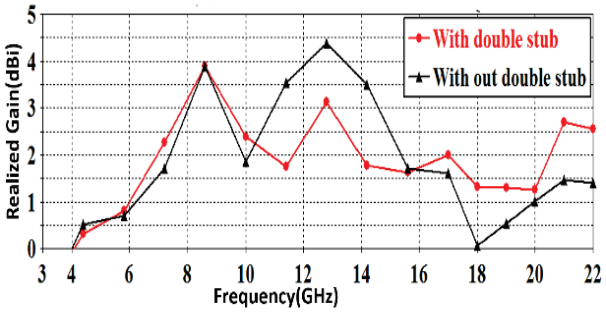

Fig. 15. Comparison of Antenna-I and Antenna-II simulated gain as a function of frequency.

Figure 17 shows a comparison between simulated and measured 1-D radiation patterns of Antenna-II for

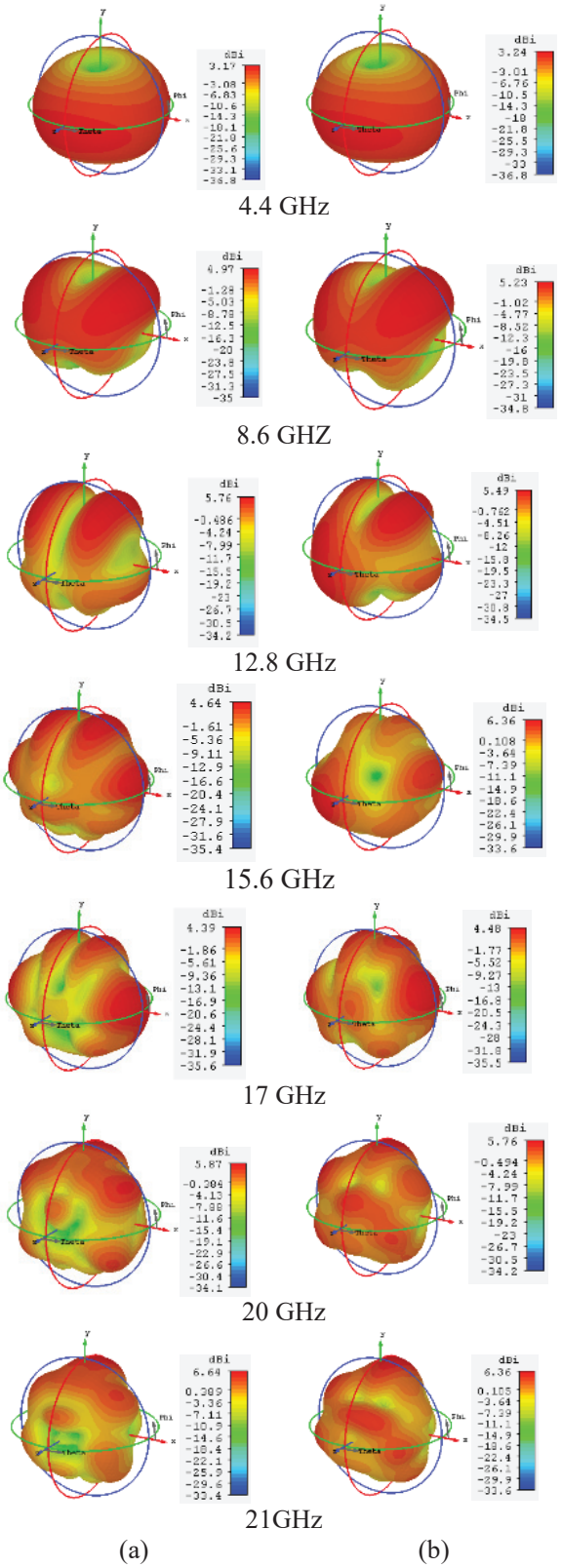

Fig. 16. comparison of 3-D far-field radiation patterns of (a) Antenna-I (without double stubs) and (b) Antenna-II (with stubs) for various frequencies.

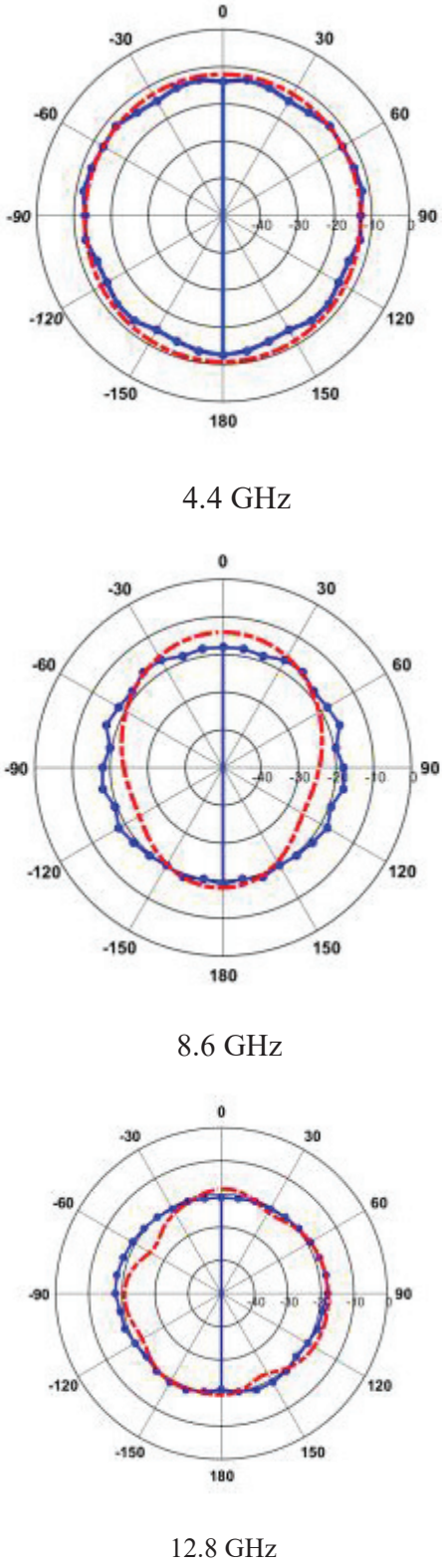

Fig. 17. Simulated and measured far-field radiation patterns of the proposed Antenna-II at XZ-plane; simulation (red), Measured (blue) at 4.4 GHz, 8.6 GHz, and 12.8 GHz.

three frequencies (4.4 GHz, 8.6 GHz, and 12.8 GHz). The patterns were calculated and measured in the plane perpendicular to the antenna. The patterns show the omnidirectional property of the monopole antenna.

VII. COMPARISON WITH PREVIOUS WORKS

Table 3 compares the parameters and characteristics of the optimized antenna reported in this paper to those of several UWB antennas disclosed in recent publications. The table shows that the proposed antenna-II achieved the 2^{nd} largest bandwidth after that in [11] but at 36% of the size of the antenna in [11]. As regards the size, the proposed antenna has a smaller size than those in [7–9, 11] and [18]. The proposed antenna has gain values that are comparable to other antennas. The proposed antenna offers a competitive performance of gain, bandwidth, and size.

Table 3: Comparison between recently published UWB antennas and the proposed antenna in this work

[Ref]	Dimensions [mm]	Frequency range [GHz]	BW [%]	Gain [dB]
[4]	17×7.6×1.0	4-10.0	85.7	N/A
[5]	25×30×1.6	3.6-14.7	121.6	4
[6]	40×10×0.8	2.8-10.9	118	2.4-6.2
[7]	36×36×1.27	3.1-11	121	N/A
[8]	25×38×1.6	2.9-13	127	3 − 9
[9]	40×32.4×1.5	3-11	114	0 − 5
[10]	16×20×1.6	4.8 – 13.7	96.22	2 − 4
[11]	52×46×1.6	1.8 up to 17.7	162	N/A
[15]	14×22 ×1.6	3.05-13.57	125	N/A
[18]	36.2×41×1.52	3.05-10.95	113	1.4-5.7
This work	28×31× 1.6	3.34 up to 22	155	0.5-4.0

VIII. CONCLUSION

A compact fractal patch monopole antenna with wide bandwidth and good omnidirectional radiation pattern covering a frequency range beyond the UWB is proposed. A sectoral patch was scaled down and added to the initial one to form the proposed sectoral-shaped fractal. In this way, a design rule has been presented and demonstrated. To improve the proposed antenna gain, two rectangular stubs were attached to the feeding line. The proposed antennas were designed, analyzed, and the optimized design was fabricated. The antenna was able to cover a frequency range of 3.34 GHz up to 22 GHz. The proposed antenna is ideal for UWB applications because of its small size and high impedance bandwidth.

REFERENCES

[1] First Report and Order (FCC 02-48), "New public safety applications and broadband internet access among uses envisioned by FCC authorization of ultra-wideband technology," *Action by the Commission*, vol. 14, Feb. 2002.

[2] J. Yeo, Y. Lee, and R. Mittra, "Wideband slot antennas for wireless communications," *IEE Proc. Microwaves Antennas and Propagation*, vol. 151, pp. 351-355, 2004.

[3] C. Ying, G. Li, and Y. Zhang, "An LTCC planar ultra-wideband antenna," *Microwave and Optical Technology Letters*, vol. 42, pp. 220-222, 2004.

[4] C. Lin, Y. Kan, L. Kuo, and H. Chuang, "A planar triangular monopole antenna for UWB communication," *IEEE Microwave and Wireless Components Letters*, vol. 15, no. 10, pp. 624-626, 2005.

[5] A. H. Majeed, K. H. Sayidmarie, F. M. A. Abdussalam, A. Alhaddad, and R. A. Abd-Alhameed, "A. microstrip-fed pentagon patch monopole antenna for ultra-wideband applications," *IEEE Conf. on Internet Technologies and Applications (ITA),* pp. 452-456, 2015.

[6] X. N. Low, Z. N. Chen, and T. S. P. See, "A UWB dipole antenna with enhanced impedance and gain performance," *IEEE Transactions on Antennas and Propagation*, vol. 57, no. 10, pp. 2959-2966, Oct. 2009.

[7] T. Karakolak and E. Topsakal, "A double-sided rounded bow-tie antenna (dsrba) for UWB communication," *IEEE Antennas and Wireless Propagation Letters*, vol. 5, 2006.

[8] S. Naser and N. Dib, "Printed UWB pacman-shaped antenna with two frequency rejection bands," *Applied Computational Electromagnetics Society (ACES) Journal*, vol. 32, no. 3, pp. 186-192, Mar. 2017.

[9] A. A. Omar, S. Naser, M. I. Hussein, N. I. Dib, and M. W. Rashad, "Super formula-based compact UWB CPW- fed-patch antenna with and without dual frequency notches," *Applied Computational Electromagnetics Society (ACES) Journal*, vol. 32, no. 11, pp. 97-986, Nov. 2017.

[10] M. N. Shakib, M. Moghavvemi, and W. N. L. Mahdi, "Design of a compact planar antenna for ultra-wideband operation," *Applied Computational Electromagnetics Society (ACES) Journal*, vol. 30, no. 2, pp. 222-229, Feb. 2015.

[11] K. H. Sayidmarie and Y. A. Fadhel, "Self- complementary circular disk antenna for UWB applications," *Progress in Electromagnetics Research*, vol. 24, pp. 111-122, 2011.

[12] K. H. Sayidmarie and Y. A. Fadhel, "A planar self-complementary bow-tie antenna for UWB applica-

tions," *Progress in Electromagnetics Research C*, vol. 35, pp. 253-267, 2013.
[13] J. Anguera, E. Martinez, C. Puente, C. Borja, and J. Soler, "Broad-band dual-frequency microstrip patch antenna with modified Sierpinski fractal geometry," *IEEE Transactions on Antennas and Propagation*, vol. 52, no. 1, pp. 66-73, Jan. 2004.
[14] K. H. Sayidmarie and M. E. Bialkowski, "Fractal unit cells of increased phasing range and low slopes for single-layer microstrip reflectarrays," *IET Microwaves, Antennas & Propagation*, vol. 5, no. 11, pp. 1371-1379, 2011.
[15] A. Ghazi, M. N. Azarmanesh, and M. Ojaroudi, "Multi-resonance square monopole antenna for ultra-wideband applications," *Progress in Electromagnetics Research C*, vol. 14, pp. 103-113, 2010.
[16] K. H. Sayidmarie and Y. A. Fadhel, "UWB fractal monopoles of rectangular and triangular shapes," *4th IEEE International Symposium on Microwave, Antenna, Propagation and EMC Technologies for Wireless Communications*, pp. 709-712, Nov. 2011.
[17] A. H. Majeed and K. H. Sayidmarie, "Flower shaped elliptical patch antenna for UWB applications," *International Journal of Microwave and Optical Technology*, vol. 15, no. 2, pp. 168-178, Mar. 2020.
[18] B. Guenad, A. Chaabane, D. Aissaoui, A. Bouacha, and T. A. Denidni, "Compact cauliflower-shaped antenna for ultra-wideband applications," *Applied Computational Electromagnetics Society (ACES) Journal*, vol. 37, no. 1, Jan. 2022.
[19] C. A. Balanis, *Handbook of Microstrip Antennas*, John Wiley and Sons, New York, 1982.
[20] M. Singh, A. Basu, and S. K. Koul, "Design of aperture coupled fed micro-strip patch antenna for wireless communication," *2006 Annual IEEE India Conference,* pp. 1-5, 2006.

Asmaa H. Majeed received B.Sc. Degree in Electronic and Communication from the Department of Electrical Engineering,the University of Technology, Baghdad, Iraq, then an M.Sc degree in Electronic and Communication from the Department of Electrical Engineering, Baghdad University, Baghdad, Iraq. She then received a Ph.D. in Electronic and Communication from the Department of Electrical Engineering/Basrah University, Basrah, Iraq. She has approximately 14 years of teaching experience. She is a member of the teaching staff at the Department of Information and Communication Engineering, College of Information Engineering, Al-Nahrain University, Iraq. She has published 17 papers in national and international journals/conferences. Her research interests include the analysis and design of printed antennas.

Khalil Sayidmarie received a B.Sc. degree with first-class honors in Electronic & Communication Engineering from Mosul University, Iraq, in 1976, and a Ph.D. in Antennas & Propagation from Sheffield University, U.K. in 1981. Then he joined the College of Engineering at Mosul University in 1983 and was promoted to full professor in 1992. He worked as the head of the electrical engineering department for 9 years. He was a co-founder of the College of Electronic Engineering at Mosul University. He has been a professor of communication engineering at that college. Sayidmarie served as a professor of communication engineering at the College of Engineering, University of Amman Al-Ahliyya, Jordan from Oct 2006 to Sept 2009. He is a professor of communication engineering at the College of Electronic Engineering, Ninevah University. He has supervised 45 MSc and Ph.D. theses and published more than 140 papers.